ETH
Eidgenössische Technische Hochschule Zürich
Swiss Federal Institute of Technology Zurich

IAC Institute for Atmospheric and Climate Science

Master Thesis

A Lagrangian Analysis of the Dynamical and Thermodynamic Drivers of Greenland Warm Events during 1979–2017

Department of Environmental Systems Science (D-USYS), ETH Zurich
Institute for Atmospheric and Climate Science (IAC)

Supervisors:

Dr. Lukas Papritz, IAC, ETH Zurich (main advisor)
Prof. Dr. Heini Wernli, IAC, ETH Zurich

Submitted by:

Mauro Hermann
13-916-481
Zurich, 5 April 2019

Abstract

The acceleration of mass loss from the Greenland Ice Sheet (GrIS) since the late 1990s was primarily driven by increased surface melt, partly concentrated in single extreme melt events. A textbook example was observed around 12 July 2012 (EV69), when almost the entire GrIS was melting, including Summit Station at 3216 m in the dry inland plateau. The melt event coincided with strong meridional air mass transport towards the GrIS followed by a Greenland blocking, which resembles the anomalous synoptic pattern that became increasingly frequent in the North Atlantic region in the last two decades.

Here, we investigate the atmospheric forcing of extraordinary melt periods by assessing the main dynamical and thermodynamic processes that cause so-called warm events. We present an ERA-Interim-based climatology of 77 Greenland warm events affecting the high accumulation area in 1979–2017. These events became longer and more frequent during the study period. With Lagrangian backward trajectories started from the lowermost $\sim$500 m above the GrIS, we identify transport from a climatologically warmer region as key process for Greenland warm events. With an about 15° latitude more southerly air mass origin and subsidence-induced adiabatic warming, this process is twice as important as diabatic heating to the final warm anomaly over North and East Greenland. In South and West Greenland, major contributions come from ascending air masses and in the Southwest, warm events are dominated by orographically induced latent heating as opposed to transport. 70–85% of all warm events go along with a Greenland blocking, which we suggest induces additional melt via modulations of the surface energy budget not captured by our Lagrangian methodology.

We further qualify the importance of the concurrent US Great Plains heatwave for EV69. In contrast to previous studies, we find that air masses arriving over the GrIS during EV69 mostly originated from the Canadian Arctic, Newfoundland and the subtropical North Atlantic, which were partly also anomalously warm.

Given the relevance of atmospheric blocking for Greenland warm events and their link to anomalously warm summers, it is crucial, as we argue, to better understand the modification of inter-annual climate variability by climate change in the North Atlantic region, to more accurately predict future GrIS mass loss. Also, more research on cloud radiative effects is needed to capture the GrIS-wide variability of surface energy budget anomalies during Greenland blocking.

Acknowledgements

I would like to express my great appreciation to my main supervisor Dr. Lukas Papritz from the Institute for Atmospheric and Climate Science (IAC) at ETH Zurich. He guided me through all of the thesis, brought in breaths of fresh air whenever I was stuck, while still allowing this study to be my own research.

Further, I wish to acknowledge the support from my second supervisor and IAC institute head Prof. Dr. Heini Wernli. Throughout my entire studies, I not only enjoyed several of the courses he taught, but also developed academically thanks to his great guidance, advice and encouragement during both my bachelor and master thesis, respectively.

Both my supervisors created an ambiance full of intellectual and social support, which is a great benefit for research taking place in their group. Thus, my special thanks is extended to all the other group members of the Atmospheric Dynamics group at IAC. They gave valuable input during milestone presentations and were very accommodating, no matter who I asked for advice. They further set up my working environment and the entire data set, which was the essential technical basis of my master thesis.

I wish to thank my fellow students with whom I shared the office, had inspiring discussions and built up a friendship that will go beyond our period of study. Finally, to my family, I am especially grateful for the emotional support in all of my academic and personal pursuits, which has so far been the foundation of my efforts.

Table of Contents

List of Figures

List of Tables

Chapter 1

Introduction

The Greenland Ice Sheet (GrIS) is the world's second largest ice body and holds water equivalent to 7 m of global sea level rise if it were to melt completely. Mass loss from the GrIS has been observed over approximately the past 120 years, mainly by surface melt and ice discharge across the grounding line: Aerial imagery and space-born altimetry observations indicate that total mass loss from the GrIS more than doubled from 1900–2003 to 2003–2010 to 186.4 ± 18.9 Gt/yr (Kjeldsen et al., 2015). Since then, the GrIS has been losing almost an additional 100 Gt/yr, summing up to 278 ± 35 Gt/yr (Tedesco et al., 2016a). The total mass balance (TMB) of the GrIS is typically split in two parts: ice discharge (D) and the surface mass balance (SMB). While D accounted for the majority (58%) of mass loss at the beginning of this century, its relative contribution to the TMB decreased to 32% in 2009–2012 (Enderlin et al., 2014). Not only the current magnitude, but also the speedup of mass loss from the GrIS, observed recently and predicted for the future, is primarily driven by negative SMB (Enderlin et al., 2014; Van den Broeke et al., 2016).

The GrIS Surface Mass Balance

In general, the SMB of the GrIS can be approximated as the difference between winter snow accumulation and melt water runoff during summer. Contributions from other mass gains (rainfall, frosting) and losses (evaporation, snow and ice sublimation, drifting snow sublimation) appear negligible relative to snowfall and runoff (Box et al., 2004; Lenaerts et al., 2012). Surface melt regulates SMB and almost entirely causes its current decrease, which in turn dominates the recent decrease in TMB (Box et al., 2004; Fettweis et al., 2012; Andersen et al., 2015; Van den Broeke et al., 2016). The

second contributor, snow accumulation, has decreased since the early 2000s as well, due to reduced cyclone but increased anticyclone frequency (Chen et al., 2016). So both contributors to the SMB have favored a stronger mass loss from the GrIS, with melt as a primary driver of SMB (and TMB).

The importance of SMB for TMB and its large inter-annual variability was illustrated clearly in 2012. SMB was $\sim$400 Gt/yr more negative than the 1958–2011 average, which is only one of many records broken in 2012 (Tedesco et al., 2013). Gravity-measuring GRACE satellites observed a record low TMB of -638 ± 45 Gt/yr in that hydrological year, which is more than twice the 2002–2015 average (Tedesco et al., 2016a). The summer season 2012 contained periods, covering in total 42 out of 92 summer days, which we define later and in more detail as "warm events" (Chap. 2). Two of the strongest warm events occurred in mid and late July 2012, when satellites measured melt over 98.6% and 79% of the GrIS surface area, respectively (Nghiem et al., 2012). During the first warm event, surface melt was even recorded at Summit Station, 3216 m above sea level. Prior to 2012, similar extreme melt extents were only observed once in 1889, according to Summit Station ice core data (Meese et al., 1994), and several times during the Medieval Climate Anomaly that ended more than 600 years ago (Neff et al., 2014).

Role of the Atmosphere

Mass loss from the GrIS and the consequent rise in global sea level is, via modulation of snowfall and surface air temperature, highly sensitive to the atmospheric forcing (Hanna et al., 2005; Chen et al., 2016). The oceanic forcing of ice melt during the mid-July 2012 warm event was weak (Hanna et al., 2014) and the linkage of high sea surface temperatures and the GrIS SMB is generally limited due to the kadiabatic wind blocking effect (Noël et al., 2014). The atmospheric forcing can to some extent be characterized by the North Atlantic Oscillation (NAO) index (Hurrell et al., 2013) or the Greenland Blocking Index (GBI) (Hanna et al., 2013). The two indices capture the variability of the atmospheric circulation in the North Atlantic region or near Greenland, respectively. They are anticorrelated (Hanna et al., 2016) and both based on geopotential height, but are also distinctive statistical patterns of atmospheric variability. The simplest version of the NAO index, the station-based NAO index, is the difference of normalized sea level pressure (SLP) between Lisbon, Portugal and Stykk-

isholmur/Reykjavik, Iceland - thus capturing a dipole structure of the Azores High and the Icelandic Low. The GBI, on the other hand, represents the monopole structure of 500 hPa geopotential height (Z500) and its standardized anomaly, respectively, averaged in the 60–80°N, 20–80°W region, hereafter GBI region.

When the two centers of action (Azores High and Icelandic Low) are reinforced, i.e., during positive phases of the NAO (and negative GBI: NAO+/GBI−), the North Atlantic storm track and zonal flow are strong. This typically goes along with colder temperatures in Greenland. By contrast, weakened centers of action during NAO−/GBI+ stand for weaker westerlies and storm track activity, and also blocking systems centered over the GrIS. NAO−/GBI+ is the relevant phase to Greenland warm events as the meandering jet stream allows for more southerly flow towards Greenland, and the formation of blocking anticyclones leading to subsidence, respectively, which both cause warming over Greenland. This was the case in the anomalously warm summer 2012 that went along with a JJA NAO of −1.60 (Hanna et al., 2014). While NAO− favors higher temperatures especially in South and West Greenland, colder conditions and below average ice loss are typically observed in Svalbard (Fettweis et al., 2013; Box et al., 2018). Summer 2012 was one out of a series of NAO− summers since the late 1990s with a doubled anticyclone frequency over Greenland compared to the past 50 years (Fettweis et al., 2013). A case of very extreme meridional transport, not taking place in summer, however, was observed in April 2011, when the polar jet stream reached down to North Africa and enabled Saharan dust transport to East Greenland (Francis et al., 2018).

To summarize, the large-scale flow can lead to high temperatures in Greenland by northward advection of warm air and subsidence-induced adiabatic warming in GrIS-centered blocking anticyclones. Demonstrated by the thermodynamic energy equation, diabatic heating is another source of warming (Holton and Hakim, 2012). It comes in the form of turbulent surface fluxes, latent heating/cooling in clouds and radiation. Turbulent surface fluxes are typically limited in summer, due to the small surface-atmosphere temperature gradient. Latent heating and cooling as well as radiation cause local air mass warming and are strongly dependent on moisture content and cloud cover. On top of these warming mechanisms, there is the overall warming trend under climate change. The Arctic warms much stronger than the globe on average; a

process known as Arctic amplification (e.g., Serreze and Barry, 2011).

Warm Events and US Heat Wave in July 2012

In summer 2012, a number of different processes have been proposed to have contributed to the two major Greenland warm events. They often relate to the NAO−/ GBI+ situation described before. Additionally, the importance of the concurrent heat wave and associated moisture transport was highlighted. Over the North American continent, the most severe drought in 117 years occurred, which went along with hot surface temperatures (Hoerling et al., 2014). Atmospheric transport from lower latitudes towards the GrIS in early July was suggested to be closely linked to warm air advection from the North American heatwave and moisture uptake in the western subtropical North Atlantic Ocean (Neff et al., 2014; Bonne et al., 2015). Warm air advection obviously accounted for a large part of ice loss in all of July (Hanna et al., 2014). Directly related to the high liquid water content of the warm air masses were optically thin liquid clouds, which increased the downward longwave radiative flux over the normally dry GrIS inland plateau and enabled surface melt at elevations above 3000 m (Bennartz et al., 2013).

Atmospheric Water Content

Clouds, which were warming the Summit Station area in July 2012, however, can also have an inverse effect on surface temperature, depending on their optical thickness. For example, it was the GrIS-wide decrease in optically thick clouds that led to extra downward shortwave radiation in the past 20 years (Hofer et al., 2017). Atmospheric moisture tends to block solar energy, i.e., incoming shortwave radiation, if in the form of cloud water, while water vapor emits longwave radiation towards the surface (e.g., Ding et al., 2017; Wernli and Papritz, 2018). Gallagher et al. (2018) argue that the sum of these two competing effects is a net increase in incoming radiation resulting from clouds over the ice sheet. A recent comprehensive study by Wang et al. (2019) summarized the complex and spatially heterogeneous cloud radiative effect as follows: The net cloud radiative effect over the cold and rarely melting GrIS plateau, including Summit Station, is warming, while the dark and lower-elevated ablation area experiences a cooling by clouds, especially in West Greenland. We note here, that cloud radiative effects and the surface energy budget in general, are not the scope of this thesis. We

will cover the surface energy budget qualitatively in the discussion section, but will not quantify it in our analysis.

Research Questions

We follow two main objectives when analyzing Greenland warm events. First, we want to go beyond detailed case studies and investigate such events systematically in the period of 1979–2017. Second, we focus on the atmospheric dynamics enabling warm events and the thermodynamic processes warming air masses along their way, rather than on processes acting on the ice sheet locally, which is why we apply a Lagrangian trajectory method. There are several spatially heterogeneous mechanisms acting on the GrIS. So for example the concurrent occurrence of largest positive anomalies of surface temperature and of cloud radiative forcing at Summit Station during southerly circulation regimes (Gallagher et al., 2018). In this example, we would aim to investigate the southerly circulation regime, which was at the root of positive temperature anomalies and likely also of atmospheric moisture. Both main objectives are motivated by a lack of, or an additional need for understanding of the dynamics of Greenland warm events. More specifically, we use the Lagrangian analysis tool LAGRANTO (Wernli and Davies, 1997; Sprenger and Wernli, 2015) and ERA-Interim reanalysis data (Dee et al., 2011) to capture these processes, and to answer the following research questions:

(Q1) How often did warm events occur over the GrIS during 1979–2017?

(Q2) Which air mass transport pathways were responsible for these warm events?

(Q3) What were the characteristic physical processes contributing to warming of the air masses?

(Q4) Which synoptic flow configurations led to the different pathways?

(Q5) Do regions of the GrIS differ in terms of the main pathways (Q2), warming processes (Q3) and flow configurations present (Q4) during warm events?

To address the regionality of warm events (Q5), we gear our analysis to the drainage basins after Zwally et al. (2012). Besides their relevance to the GrIS TMB and the research field of cryosphere in general, these regions capture the main differences in atmospheric dynamics and climatological gradients. By answering Q1–Q5, we want to improve our understanding of the atmospheric evolution prior to warm events, which

is expected to become increasingly relevant to GrIS mass loss and global sea level rise. This study further serves as a starting-point for impact-oriented cryospheric studies.

Chapter 2

Data and Methods

This chapter describes the ERA-Interim reanalysis data (Sec. 2.1) and the methodology used for its analysis. We introduce a new definition of warm events (Sec. 2.2) and two different climatologies to assess warming over Greenland (Sec. 2.4). We apply existing tools to represent our data in the form of Lagrangian backward trajectories (2.3) and composites of both trajectory properties and synoptic fields (Sec. 2.5).

2.1   ERA-Interim Data

This study is based on ERA-Interim reanalysis data from the European Centre for Medium-Range Weather Forecasts (ECMWF) (Dee et al., 2011). The data is available every 6 h in 1979–2017 on a T255L60 grid, i.e., with a horizontal grid spacing of 1° and 60 vertical levels. Typically, a numerical weather model assimilates millions of ground- and space-born meteorological observations and generates a global, three-dimensional analysis of the atmospheric state. For ERA-Interim, all observations in 1979–2017 are assimilated with the same numerical model to then fill gaps in space, time and un-observed parameters. On the one hand, there are analysis fields (e.g., temperature), where a previous model forecast is blended with available observations. On the other hand, forecast fields (e.g., 6 h accumulated precipitation) are based on previous analyses and the numerical model to calculate these fields. The assimilation results in temporally, dynamically and thermodynamically consistent meteorological fields. One could describe reanalysis data as the "best guess" of the past atmospheric state. For that reason, we implicitly refer to it as the actual state of the atmosphere during this study.

To separate land and ice grid cells, we use the ice outline after Zwally et al. (2012) shown in Fig. 2.1, which is based on space-born surface elevation data. Grid cells with a center inside the ice outline are classified as ice grid cells, the remaining ones as land grid cells. The filtering procedure reduces the number of grid cells used here from 675 to 519. It results in a GrIS area of 1.73 million km^2, which is slightly overestimated (+0.7%) with respect to that observed (Zwally et al., 2012). Not only the ice outline, but also the eight drainage basins after Zwally et al. (2012) are a highly practical reference for cryospheric studies, and at the same time capture some of the main climatological characteristics (Fig. 2.1). We will define regions of interests according to these drainage basins and explain our underlying motivation in Sec. 3.5.
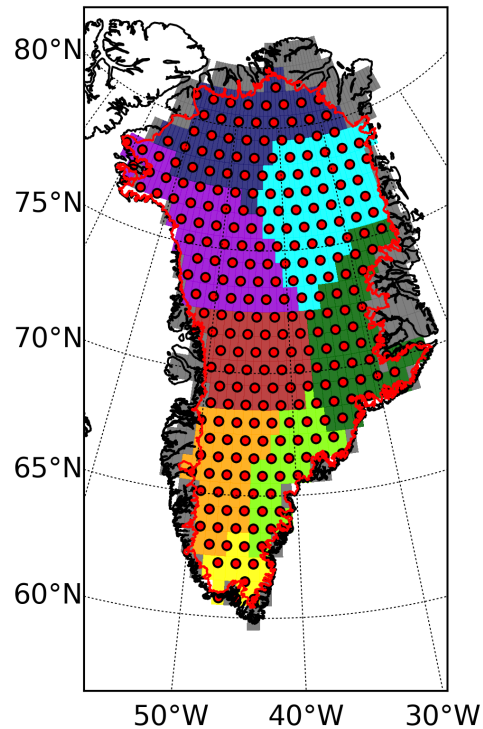
Figure 2.1: The trajectory starting locations (red circles) distributed with Δx=80 km inside ice grid cells. Grid cells are colored according to their drainage basin affiliation after Zwally et al. (2012) (blue 1, cyan 2, green 3, light green 4, yellow 5, orange 6, red 7, purple 8). Greenland grid cells centered outside the ice outline (Zwally et al., 2012; solid red line) are shown in grey and the coastlines in solid black.

2.2 Definition of Warm Events

As previous studies focused on single Greenland warm events, such as in July 2012 (e.g., Nghiem et al., 2012; Bennartz et al., 2013; Neff et al., 2014), there is yet no generally accepted definition of a warm event. In this work, to scan the past four decades systematically for warm events, we define warm events as follows:

First, surface melt is approximated by a skin temperature (SKT) greater or equal to $-1°$C, analogous to the threshold used for space-born ice surface temperature data to detect melt by Nghiem et al. (2012). A time step is then interpreted as part of a warm event if at least 5% of the total ice surface area is melting and located above 2000 m elevation. In order to account for the pronounced diurnal temperature cycle

Table 2.1: Number of events (N) and duration of the longest event resulting from different area and elevation thresholds used to identify warm events.

Min. Area [%]	Min. Elevation [m]	N	Longest Event [d]
5	2000	77	16.25
10	1500	123	36.25
	2000	33	10.75
15	1500	80	19.25
20	1500	41	12.25
	2000	4	5.25

in summer, time steps that are at maximum 24 hours apart are grouped to one event. So the warm event time steps are connected in time to yield a warm event with the starting (end) date defined as the first (last) time step when melt was detected, but not preceded (followed) by melt for more than 24 hours. Events shorter than 24 hours are neglected.

Elevation is used as an additional criterion because the GrIS topography spans an elevation range from sea level to 3175 m (highest ERA-Interim grid cell), and to emphasize the distinctiveness of the events from the typical summer melt. Below 1000 m on the northern to below 2000 m on the southern GrIS, surface melt generally occurs in more than 20% of the summer days in 1979–2017 (Fig. 2.2). The exact thresholds, 5% and 2000 m, were defined after careful analysis. Warm events defined with various area (5%, 10%, 15%, 20%) and elevation thresholds (1500 m, 2000 m) differ in terms of duration and total count (Tab. 2.1). With thresholds of 5% and 2000 m, a reasonable duration in the range of synoptic timescales of up to about two weeks results. Total count is desired to be large enough
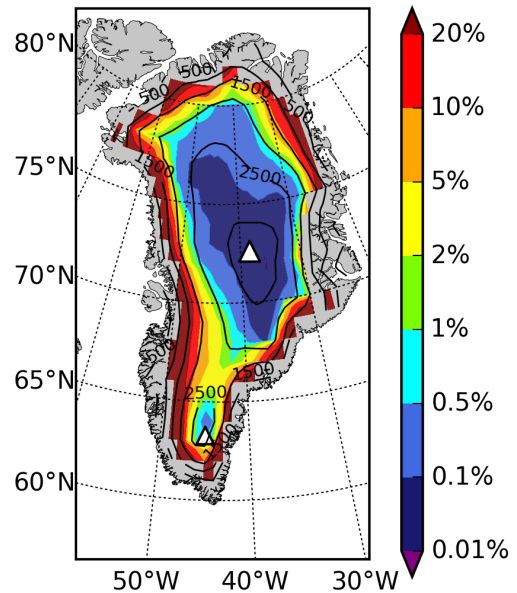
Figure 2.2: JJA melt frequency during 1979–2017. The two triangles show Summit (3216 m) and South Dome (2850 m) location, and solid contours indicate elevation [m] with 500 m spacing.

9

for a robust statistical evaluation.

2.3 Lagrangian Analysis

One way of depicting atmospheric phenomena is the Eulerian perspective, where the observer perceives the temporal evolution of the phenomena from a fixed point in space. In contrast, the Lagrangian perspective describes the atmospheric flow field from the point of view of individual air parcels or air masses in that flow. It can be used to describe air mass modifications (heat, moisture and momentum exchange) along the way, underlying physical processes and general structures of the flow field. In this study, we make use of both perspectives, but focus on the Lagrangian point of view.

2.3.1 The Lagrangian Analysis Tool LAGRANTO

A trajectory tool basically solves the trajectory equation 2.1 numerically:

$$\frac{D\mathbf{x}}{Dt} = \mathbf{u}(\mathbf{x}) \tag{2.1}$$

where $\mathbf{x}$ is the position of the air mass and $\mathbf{u}$ the 3D wind vector. The solution will be the position of every air parcel as a function of time. Example tools are FLEXTRA, the NASA Goddard trajectory model, HYSPLIT, the UGAMP offline trajectory model, and LAGRANTO (Sprenger and Wernli, 2015). Here we use the Lagrangian Analysis Tool LAGRANTO after Wernli and Davies (1997) and Sprenger and Wernli (2015). In its ECMWF version, LAGRANTO uses the three dimensional ERA-Interim wind fields to calculate air mass trajectories back in time from pre-defined starting locations. Along the trajectory, a selection of all archived variables (Berrisford et al.,
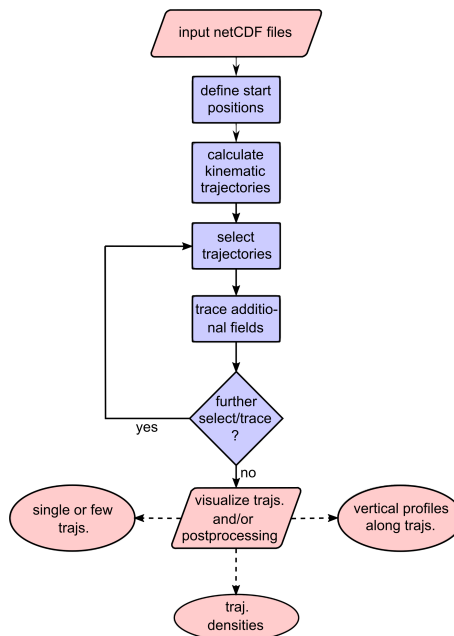
Figure 2.3: The typical steps in a LA-GRANTO trajectory calculation. The ERA-Interim fields as netCDF files, especially the 3D wind fields, serve as starting point for the trajectory analysis. *Figure adapted from Sprenger and Wernli (2015)*

Table 2.2: The variables traced along each trajectory with LAGRANTO.

Abbreviation	Variable Name	Unit
MASK	location over the GrIS or outside [0,1]	[ ]
T	temperature	[°C]
Θ	potential temperature	[K]
THCL1	potential temperature climatology (1979–2017)	[K]
THCL2	potential temperature climatology (9-yr transient)	[K]
SKT	skin temperature	[K]
PS	surface pressure	[hPa]
q	specific humidity	[g/kg]
dP	pressure difference: (p-PS)	[hPa]

2011) is traced. A typical application is illustrated in Fig. 2.3. In this study, we use LAGRANTO to calculate and select trajectories. Post-processing and plotting is mostly done in NCAR Command Language (NCL) Version 6.4.0 and Python 2.7.

2.3.2 LAGRANTO Setup

In addition to time and position (latitude, longitude, pressure) of the trajectory, the variables listed in Tab. 2.2 are traced. Relative humidity RH is derived from temperature T [K] (with $T_0 = 273.15\,\mathrm{K}$), pressure p [Pa] and specific humidity q [kg/kg] after the approximation in Eq. 2.2.

$$RH \approx 0.263 \cdot p \cdot q \cdot \left(exp \frac{17.67 \cdot (T - T_0)}{T - 29.65} \right)^{-1} \tag{2.2}$$

Starting locations $(n = 3 \times 267)$**:** We define the starting locations of the trajectories as follows. The 519 ice grid cells identified according to Sec. 2.1 serve as trajectory starting region. Within it, trajectory starting locations are equidistantly distributed every 80 km in the horizontal (Fig. 2.1). In the vertical, trajectories start at 20, 40 and 60 hPa above ground level (agl), respectively, i.e., from the lowermost ∼500 m of the atmosphere. We note that some of the starting columns are closely outside the actual ice outline. This is because grid cells are selected by their center location (Sec. 2.1), while trajectory starting locations are distributed within all of the area spanned by the ice grid cells. With 1° data resolution, however, it is reasonable not to resolve the sub grid-scale outline but to define the starting points based on the ERA-Interim grid. We

use all GrIS starting points in LAGRANTO and not only those that show melt during the warm events. The separation of trajectories arriving over the GrIS with skin temperature above or below $-1°C$ is done, whenever necessary, during the post-processing.

Starting times ($n = 1248$): The trajectories are calculated 10 days backward in time and start every 6 h during a warm event, equal to the ERA-Interim time resolution. This includes also time steps during which less than 5% of the GrIS area was melting and located above 2000 m, if they lie in between two maximally 24 h-spaced time steps that did so. For smoother plotting, trajectory positions and all variables are written out every 3 h along the trajectories.

2.3.3   Trajectory Categorization

To get insight into the warming mechanisms of each trajectory, we first evaluate the thermodynamic energy equation and then categorize trajectories similarly to Binder et al. (2017). This categorization is based on the different terms of the equation and helps to summarize the $\sim$1 million trajectories resulting from all warm events.

Thermodynamic Energy Equation

When assessing the processes that warm air masses along their trajectory, it is especially useful to use the Lagrangian point of view and examine the material derivative of temperature. According to Holton and Hakim (2012) and Bieli et al. (2015), the following relationship (Eq. 2.3) follows from the thermodynamic energy equation and the material derivative of potential temperature, $\theta = T(p_0/p)^{-\kappa}$ [K]. The total diabatic heating rate is $H = D\theta/Dt$ [K/s], and the vertical velocity equals $\omega = Dp/Dt$ [Pa/s]:

$$\frac{DT}{Dt} = \frac{\kappa T \omega}{p} + H \left(\frac{p_0}{p} \right)^{-\kappa} \tag{2.3}$$

$$\kappa \quad = R/c_p = 0.286 \text{ for air}$$
$$p, p_0 \quad \text{(reference) pressure [Pa]}$$

The material derivative of temperature (left-hand side of Eq. 2.3) denotes the change of an air masses' temperature. This occurs due to a combination of vertical motion and thus adiabatic compression or expansion (1st term on right-hand side of Eq. 2.3), and diabatic heating/cooling (2nd term). The latter can come from turbulent surface fluxes,

latent heating/cooling within clouds or radiation. In summer, sensible heat fluxes at the surface are expected to be weak, as the temperature gradient between land or sea surface and the atmosphere is typically small. The same applies to latent heat fluxes, as the moisture exchange at the surface is regulated by the highly temperature-dependent saturation vapour pressure. Temperature modifications due to latent heating/cooling are of importance for trajectories experiencing condensation of water vapor or evaporation/sublimation of hydrometeors in (the proximity of) clouds. Radiative temperature modification in the free troposphere happens mainly in the form of clear-sky cooling at a rate of $\sim 1\,\mathrm{K/d}$ (Cavallo and Hakim, 2013; Papritz and Spengler, 2017). Radiation processes acting on the ice sheet surface are not captured by the trajectory method.

Categorization Method

Trajectories are divided into four groups according to their maximum absolute change in potential temperature ($\Delta\Theta$) and temperature (ΔT). Both quantities can be positive or negative and combining all possible options gives four categories C1...C4. The maximum absolute change refers to the largest absolute difference between the (potential) temperature spectrum along the trajectory and its final (potential) temperature when arriving over the ice sheet. If, hereafter, we group the trajectories into categories C1–C4, we imply that all these trajectories arrive over melting ice, i.e., with $SKT_{final} \geq -1$ °C. We show their typical horizontal movement in trajectory density plots based on the gridding tool v2.4.2 after Škerlak (2014) in Appendix Figs. 1–4. Trajectories with $SKT_{final} < -1$ °C are neglected by that categorization method. An exemplary categorization for a time step during warm event EV69 is shown in Fig. 2.4.

Figure 2.4: Maximum absolute change in temperature (ΔT) and potential temperature ($\Delta\Theta$) along the trajectories at an exemplary time step 18 UTC 16 July 2012. Each quadrant represents one category, labelled as C1...4. Each circle represents one trajectory, colored according to the final surface elevation.

Combining $\Delta\Theta$ and ΔT gives some characteristics of the main processes acting on each group of trajectories, according to the thermodynamic energy equation introduced in the previous sub-

section (Eq. 2.3). Note that the trajectories in each category are not necessarily related in space or, over an entire event, not in time; they merely share the sign of $\Delta\Theta$ and ΔT. Category 1, top left in Fig. 2.4: $\Delta\Theta > 0°\text{C}$ and $\Delta T < 0°\text{C}$, represents trajectories that ascended along their route, experienced diabatic heating but cooled more due to expansion (1st term on right-hand side of Eq. 2.3). The complement of category 1 is category 3, bottom right in Fig. 2.4: $\Delta\Theta < 0°\text{C}$ and $\Delta T > 0°\text{C}$, including mainly descending trajectories that experienced radiative cooling and compression. Temperature changes due to diabatic processes are overruled by those due to adiabatic expansion/compression for these two categories. Category 2, top right in Fig. 2.4: $\Delta\Theta$ and $\Delta T > 0°\text{C}$, contains air masses that were mainly warmed diabatically (2nd term on right-hand side of Eq. 2.3). Category 4, on the other hand, bottom left in Fig. 2.4: $\Delta\Theta$ and $\Delta T < 0°\text{C}$, contains air masses that were mainly cooled diabatically. Weak latent heating and cooling, respectively, in addition to clear-sky radiative cooling are probably the main reasons for the diabatic changes in these categories. Vertical motion is less important to categories 2 and 4.

2.4 Summer Climatology of Potential Temperature

The 6 h-resolved potential temperature climatology is derived from a centered $\pm 10\,\text{d}$ (i.e., ± 40 time steps) average at each grid point. Climatology THCL1 represents the 39-yr long-term average climate in 1979–2017, i.e., every value is the average of 39×81 time steps. THCL2 is a 9-yr transient climatology in the period including the four previous and following years, respectively, and therefore approximates the prevailing, transient climate. Again, values are based on a centered $\pm 10\,\text{d}$ window, meaning that at every grid point, the potential temperature from 9×81 time steps are averaged for every THCL2 value.

The $\pm 10\,\text{d}$ window smooths the climatological temperature cycle and therefore, the typical peak in mid-July is less pronounced compared to the actual 6-hourly time series. In addition, single extreme days have a smaller influence on the daily climatology. This ensures that THCLx (x = 1,2) denotes climate, in the sense of a representative average, rather than an average strongly influenced by extreme short-term weather conditions.

2.5   Composites

In the course of this study, we will split the warm events into smaller subgroups. No matter what the criterion for selection is, the subgroup basically represents a set of time steps during one or several of the warm events, which share a specific pattern. The analysis of these subgroups will be performed in two ways.

First, the evolution of ERA-Interim variables along trajectories starting at the selected time steps of a subgroup can be summarized statistically. For example, we present a subgroup in terms of median and inter-quartile range (e.g., Fig. 3.11 in Sec. 3.4.3). The trajectories that are summarized are not necessarily linked in space or time, depending on the criterion. Second, we analyze the synoptic pattern during the time steps of a subgroup based on synoptic features. We make use of the Clim-ei tool to identify the synoptic features and create composites of their frequency or other ERA-Interim variables (Sprenger et al., 2017). We here quote the definitions of the features used in the study after Sprenger et al. (2017):

- "**Upper-level jet streams:** Regions where the vertically averaged horizontal wind speed between 100 and 500 hPa exceeds $30 \, \mathrm{m \, s^{-1}}$."

- "**Extratropical cyclones:** Regions determined by the outermost closed sea level pressure (SLP) contour enclosing one or several local SLP minima"

- "**Blocks:** Regions where the negative anomaly of vertically averaged PV between 150 and 500 hPa exceeds $-1.3 \, \mathrm{PVU}$ ($1 \, \mathrm{PVU} = 10^{-6} \, \mathrm{K \, kg^{-1} \, m^2 \, s^{-1}}$) and persists over at least 5 days. Anomalies are calculated as deviations from the monthly climatology of vertically averaged PV."

When mentioning feature composites of jets, cyclones or block(ing)s during the course of the study, we implicitly refer to these three definitions and concentrate on their frequency, respectively.

Chapter 3

Results

This chapter is the core of the study and shows all the insight gained on Greenland warm events. It starts with an analysis of the warming trend in summer between 1979–2017, and its attribution to climate change and seasonal weather dynamics (Sec. 3.1). In Sec. 3.2, we present the identified warm events and their change from the "recent past" to the "present day" (IPCC Special Report on the Ocean and Cryosphere in a Changing Cliamte reference periods). GrIS surface melt, as the impact-side of Greenland warm events, is subject to Sec. 3.3. The two main parts will follow in the end; First, a detailed look into the synoptic situation, melt extent and trajectory evolution during the most important warm event in July 2012, EV69, is of primary interest (Sec. 3.4). Second, we will identify the characteristic synoptic features and the trajectory pathways, and conduct a quantitative assessment of warming for all warm events in 1979–2017 (Sec. 3.5).

3.1   Potential Temperature Climatology

3.1.1   Transient Climate Anomaly

Fig. 3.1 shows the Greenland-wide anomaly of THCL2 on the lowest model layer, i.e., of near surface ($\sim$10 m) potential temperature ($TH10M$), in summer 1983–2014, compared to THCL2 in summer 1983. Remember that THCL2 represents a 9-yr average, here of $TH10M$, i.e., THCL2 in JJA 1983 stands for the 1979–1987 summer average. Over these 31 years, Greenland summer $TH10M$ increased by +0.5°C to +1.5°C over a wide area, with a stronger warming in North Greenland and along the west coast. Averaged over the ice mask, the GrIS summer warmed by 1.1 ± 0.3°C (the standard
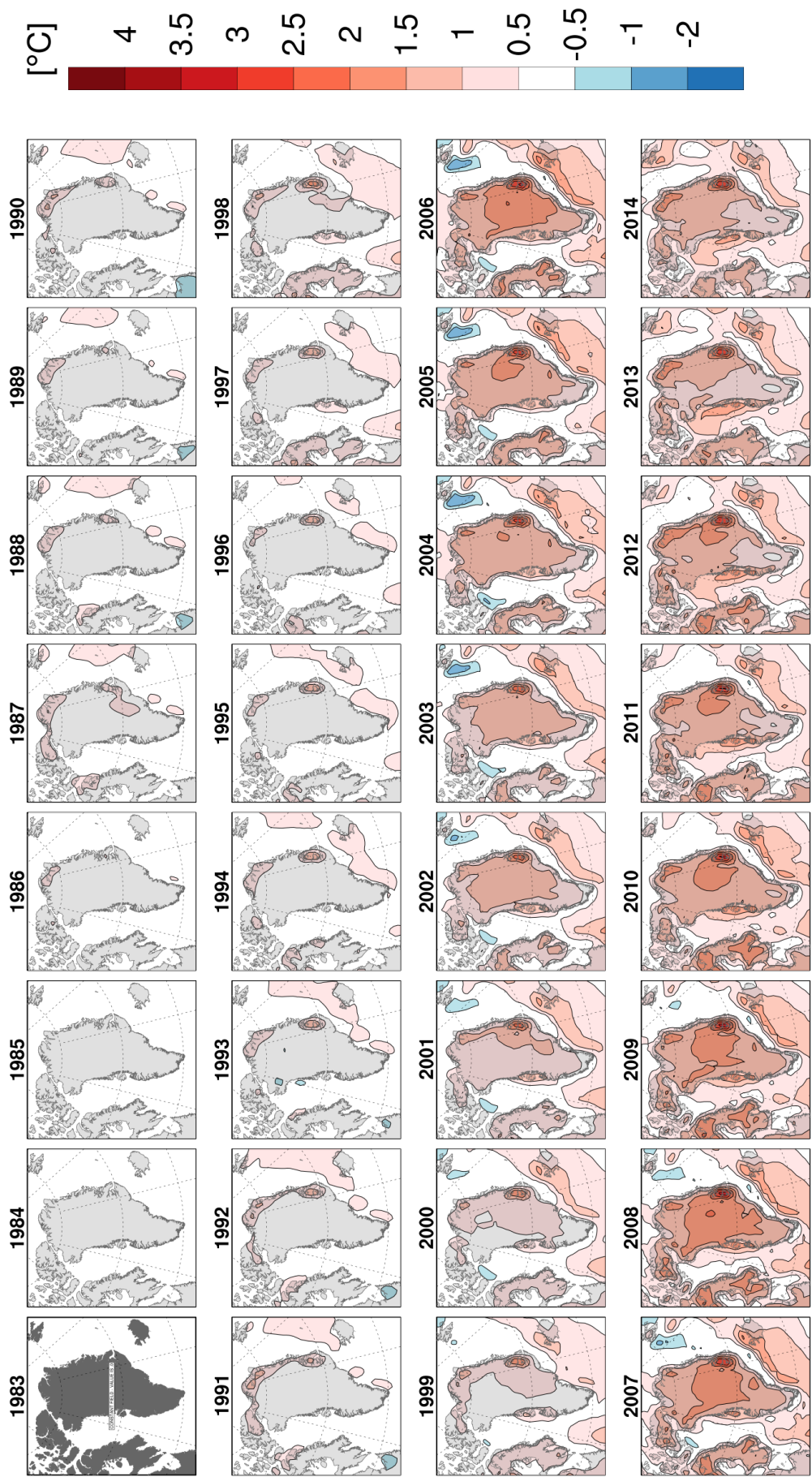
Figure 3.1: Anomaly of transient potential temperature summer climatology in 1983–2014 (THCL2), relative to THCL2 in summer 1983, both at ~10 m (lowest model layer). Note the irregular color interval.

deviation represents spatial variability) compared to THCL2 in JJA 1983. Locally, warming was strongest in the Scoresbysund fjord, which is the largest fjord worldwide, with up to 3°C. There, significant warming started in 1987 already. Averaged over the ice sheet, THCL2 shows a more than +0.5°C surface anomaly only after 1999 – 12 years later than near Scoresbysund fjord. Two weaker peak regions with a potential temperature anomaly of up to +2°C are located in the very northeast of the GrIS and ahead of the west coast over Disko Island. Contrarily, the area around South Dome warmed less than the rest of the ice sheet and locally shows a warm anomaly below +0.5°C by 2014. Between 2002 and 2012, summer climate in Greenland was warmer than just recently. THCL2 of $TH10M$ peaked in 2008 with an on average $+1.5 \pm 0.5$°C warmer transient climate than in 1983. Especially high elevations of the GrIS including South Dome and Summit showed a warm anomaly of +1.5°C to +2°C, locally exceeding +2°C, which after 2012 returned to around +1°C to +1.5°C or even lower. If this climate cooling is real or an artefact of our method will be addressed in Sec. 3.1.3.

One outstanding area of warming in Greenland is the Scoresbysund fjord. The fjord extends ~350 km inland from the East Greenland Sea Current, which transports large quantities of polar ice down the east coast of Greenland. The inner part of the fjord, however, is well-known for its polynya, a permanent open water area within closed sea ice, driven by strong (north-)westerly fall winds (Cappelen, 2014). The open water fuels local warming due to reduced albedo and higher skin temperature compared to ice. Reduced sea ice also breaks up the otherwise strong static stability of the atmospheric surface layer and thus triggers stronger upward sensible and latent heat fluxes (e.g., Zhang et al., 2011; Lesins et al., 2012). By and large, the Scoresbysund area experiences a stronger warming in the changing climate due to micro-climatic effects.

3.1.2 Annual Temperature Anomaly

Fig. 3.2 shows seasonally averaged anomalies of $TH10M$ compared to the 1983 transient summer climate (1979–1987 average). We find an accumulation of warm summer seasons in almost every year during the above-mentioned warm period 2002–2012. The warmest five summers of 1979–2017 were all in this period and their potential temperature anomalies averaged over the GrIS rank as follows: $+2.6 \pm 0.8$°C (2012), $+2.3 \pm 1.1$°C (2010), $+2.1 \pm 1.1$°C (2007), $+1.9 \pm 0.5$°C (2003) and $+1.7 \pm 0.6$°C (2005).
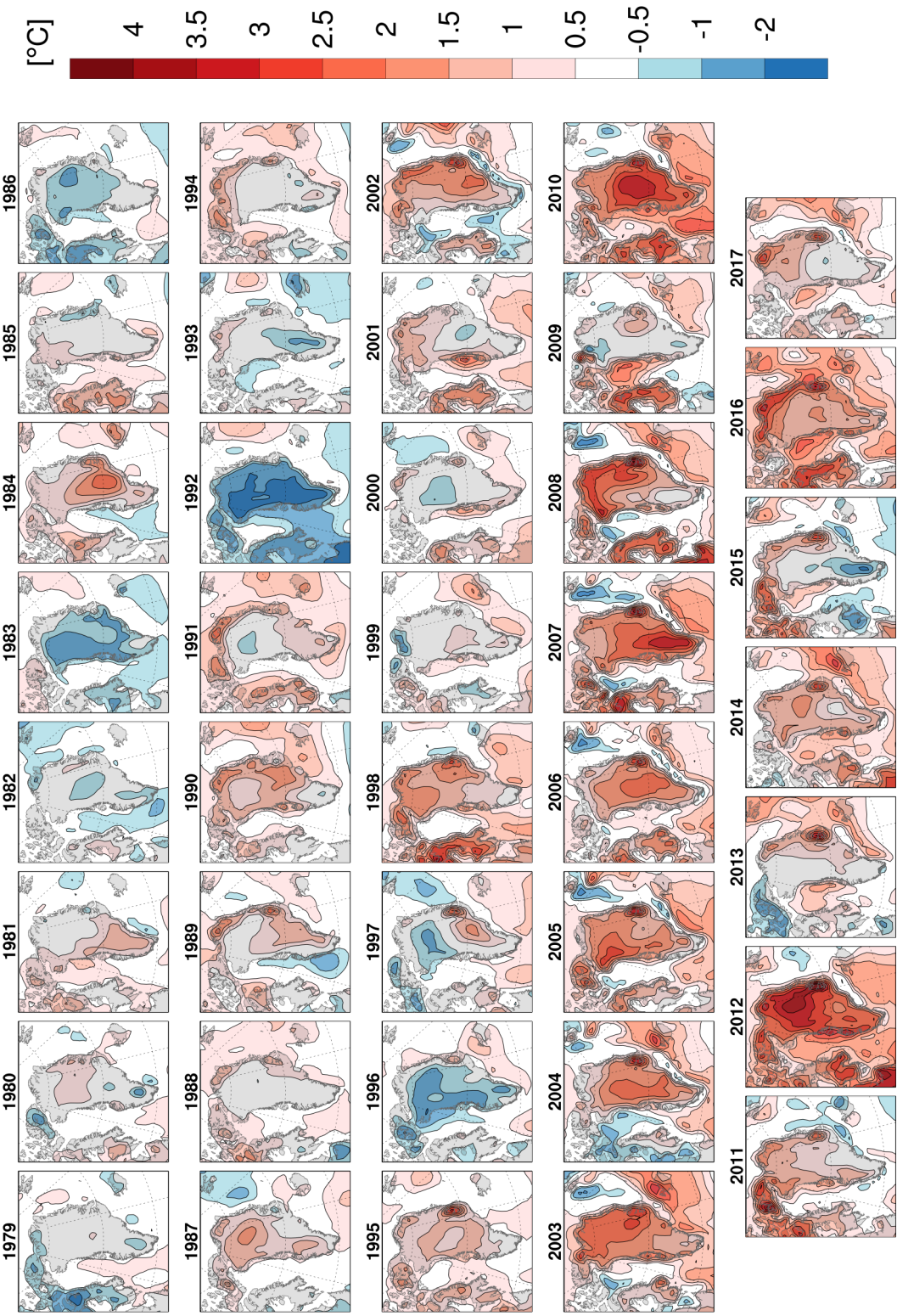
Figure 3.2: Anomaly of annual summer average of near surface ($\sim$10 m) potential temperature ($TH10M$) in 1979–2017, relative to THCL2 in summer 1983. Note the irregular color interval.

Here, standard deviations denote spatial variability.

In the last five years of the study period, however, some areas were colder or equal to the 1983 transient summer climate, so for example parts of West (2013), South (2015) or Central Greenland (2014 and 2017). Also in earlier years, summer averages reveal great inter-annual and spatial variation. For example, summer 1984 was on average 1.0 ± 0.5°C and locally up to 2.5°C warmer than 1983 THCL2. An opposite example is summer 1992, the coldest in our data set, with a spatiotemporally averaged cold anomaly of -1.9 ± 0.8°C. This highlights the large inter-annual variability and the impact of atmospheric circulation patterns – in addition to the warming climate – on the summer temperature near Greenland.

3.1.3 Circulation-Induced Temperature Anomaly

The previous two subsections brought up the two main features responsible for the temperature pattern in summer during the past 40 years: long-term climate change and short-term atmospheric circulation. One approach to quantitatively estimate their contributions to $TH10M$ is to calculate the difference between the total JJA anomaly (Fig. 3.2) and the THCL2 anomaly (Fig. 3.1). We interpret the remainder (Fig. 3.3) as the change in $TH10M$ caused by the prevailing circulation, whereas the THCL2 anomaly of $TH10M$ represents the warming due to climate change, both with respect to $TH10M$ THCL2 in summer 1983. In addition, we spatially average the three different $TH10M$ anomalies over the GrIS and show the resulting time series in Fig. 3.4.

Before 1997, the THCL2 anomaly of $TH10M$ was fluctuating around 0°C with an amplitude smaller than 0.3°C (Fig. 3.4a). From 1997 on, however, the transient near-surface climate has always been above that in summer 1983 – after 2002 by more than 1°C. Inter-annual circulation variability caused additional temperature anomalies (Fig. 3.4b), ranging from -1.8 ± 0.8°C (1992) to $+1.5 \pm 0.6$°C (2012). The large-scale circulation was thus responsible for 98% of the -1.9 ± 0.8°C cold anomaly in 1992 and for 57% of the $+2.6 \pm 0.8$°C warm anomaly in 2012, respectively (Fig. 3.4c). So on the one hand, the atmospheric dynamics is able to completely obscure the climate change signal, as for example in years 2000 or 2009. On the other hand, it can amplify climate warming by about a factor of two, e.g., in summers 2010 and 2012.
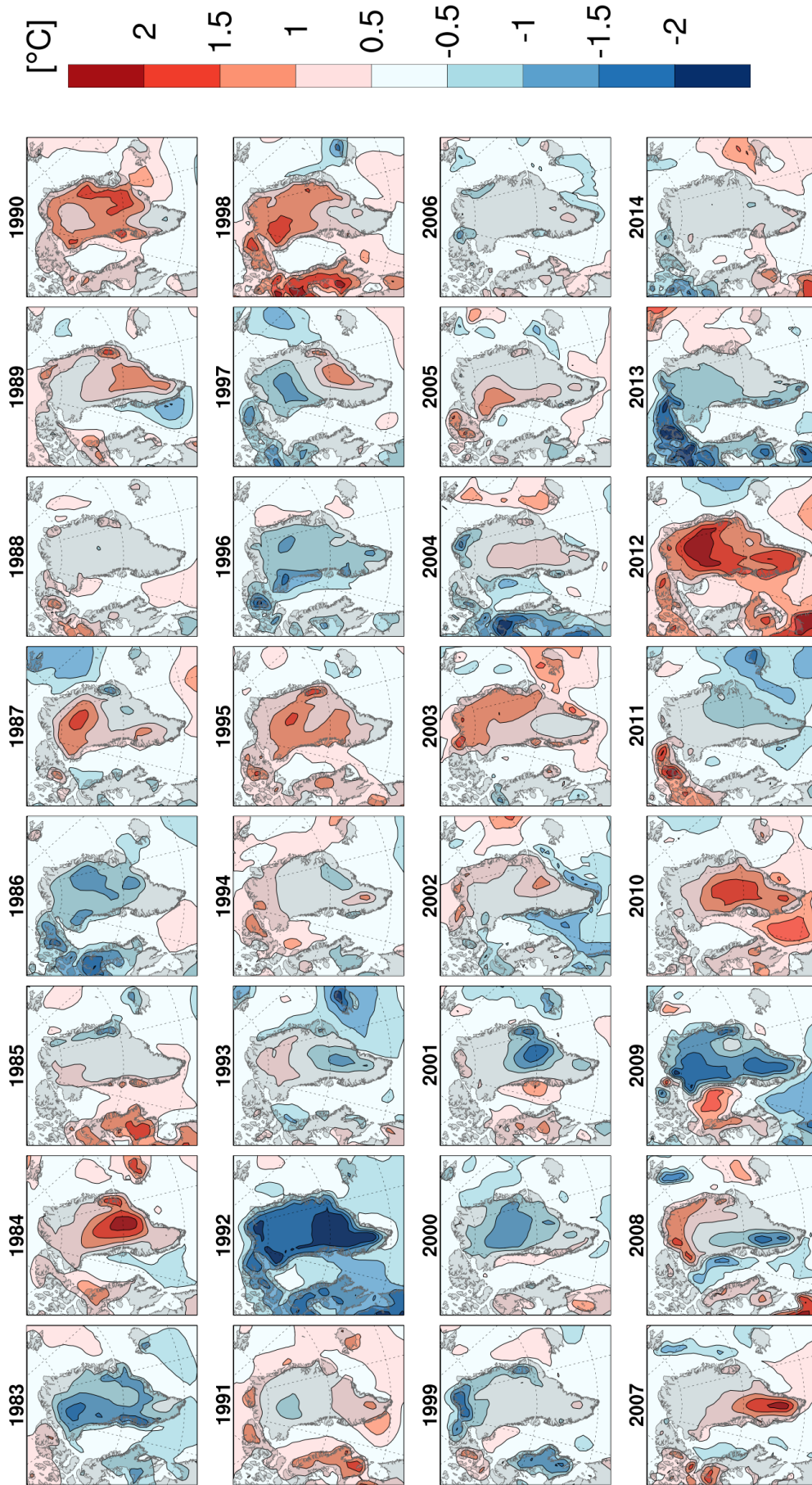
Figure 3.3: Difference between $TH10M$ summer average anomaly (Fig. 3.2) and $TH10M$ THCL2 anomaly (Fig. 3.1), indicating the temperature anomaly caused by circulation, relative to $TH10M$ THCL2 in summer 1983. Note the irregular color interval, which is different from that in Figs. 3.2 and 3.1.
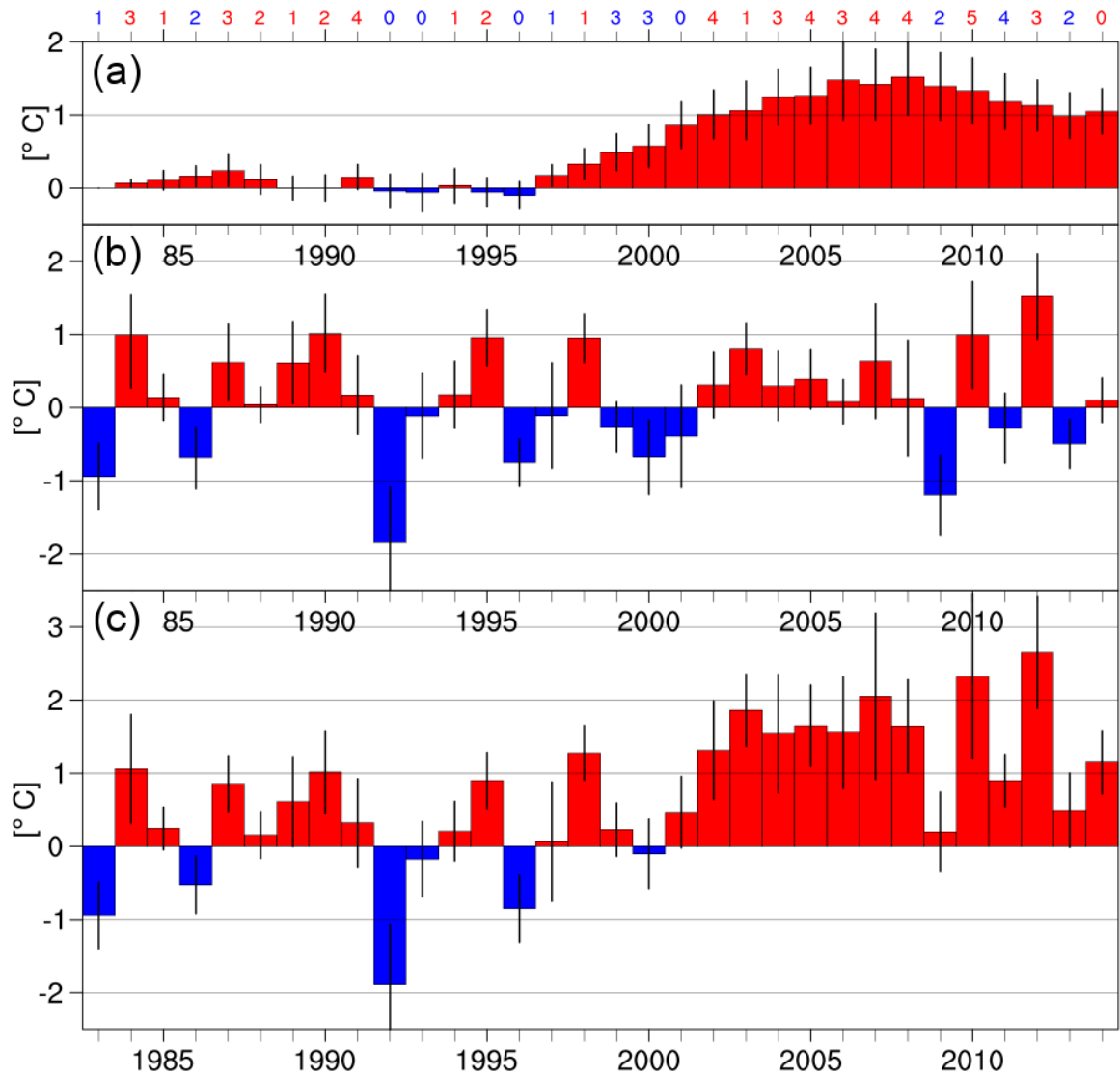
Figure 3.4: GrIS area-averaged $TH10M$ anomaly (a) of THCL2 (Fig. 3.1), (b) caused by circulation and (c) in total, i.e., the annual anomaly (Fig. 3.2) - all during JJA and with respect to THCL2 in summer 1983. Positive anomalies are shown in red, negative anomalies in blue, respectively. Thin black bars denote the spatial heterogeneity, i.e., ±one standard deviation from the GrIS average. Numbers at the top of the plot indicate the number of warm events per year, colored according to panel (b).

In years with positive or negative dynamically induced $TH10M$ anomaly, there were on average 1.6 and 2.4 warm events per summer, respectively. When weighted with the amplitude of the $TH10M$ anomalies, the distinction is even clearer with 1.3 and 2.6 warm events per summer, respectively. This difference of a factor of two indicates a relevant link between the occurrence of warm events and the dynamically induced seasonal warming. Overall, single warm events seem to be responsible for summer averages of $TH10M$ anomalies to a large degree. In Fig. 3.4, we identify summers with few

events but strong dynamically induced warming (e.g., 1998, 2003), but also summers with many events and little dynamically induced warming (e.g., 1991, 2002, 2006). This analysis, however, is insufficient in identifying whether few strong or many weak events cause a strong warm anomaly in general. It is for example plausible that "cold events" – circulation patterns causing cold anomalies over Greenland – offset strong warm events. Also does the limitation of our method used here, described in the following, obscure some of the dynamically induced warming, for example in 2002 or 2006.

The simple approach used here to differentiate the warming caused by circulation and by climate change has one clear limitation. It is especially apparent during 2002—2012. This period was dominated by persistent summer circulation anomalies characterized by NAO− (e.g., Fettweis et al., 2013; Hanna et al., 2015). A $TH10M$ anomaly caused by circulation that has the same sign over several years, is affecting the 9-yr $TH10M$ average so strongly that the latter cannot be regarded as a climate change signal only, i.e., THCL2 does not represent a meaningful climatological state. In such periods, climate warming is overestimated and the circulation-induced anomaly is too weak. This is probably to a lesser extent the case for other periods as well, when the circulation induced anomaly has the same sign over many consecutive summers. It further explains the decline of the climate change signal from 2008 on (Fig. 3.4a), which is rather an artefact than a real cooling trend.

To summarize, the method applied here is very useful to estimate the relative contribution of the two signals, climate change and the summer flow configuration. It shows that the inter-annual variability of atmospheric dynamics is able to compensate for, or more than double the current climate warming, respectively. The spatiotemporal average of $TH10M$ over nine years, however, is not fully sufficient in representing a climatological state that is completely separated from annual circulation anomalies.

3.2   Warm Event Characteristics

According to the definition in Sec. 2.2, there were 77 Greenland warm events during 1979–2017 as summarized in Tab. 3.1. They lasted between 1.25 and 16.25 d and on average 4.1 ± 3.4 d. Surface melt during short events typically covered around a third of the GrIS at maximum. So for example during EV20 (26–27 June 1991), when melt

Table 3.1: Average (Avg.), standard deviation (σ), minimum (Min.) and maximum (Max.) of warm event duration, maximum elevation (ME) and its average and maximum two meter temperature ($T2M$), respectively, as well as minimum and maximum melt extent during the event. For $T2M$ values at maximum elevation (@ME), the elevation at which it was observed is indicated in brackets. Total number of events is $N = 77$.

	Dur. [d]	ME [m]	Avg. T2M @ME [°C]	Max. T2M @ME [°C]	Min. Melt Extent [%]	Max. Melt Extent [%]
Avg.	4.1	2692	−3.5	−0.2	8.7	44.6
σ	3.4	193	1.8	1.3	5.2	10.7
Min.	1.25	2333	−7.8 [3175 m]	−2.6 [2826 m]	1.2	29.0
Max.	16.25	3175	+1.1 [2729 m]	+5.0 [2637 m]	25.6	94.8

covered up to 29.0% of the GrIS – the smallest melt extent maximum. The three warm events affecting the largest ice area over Greenland were EV69 (94.8%), EV35 (83.9%) and EV70 (70.3%) in early July 2012, end of June 2002 and end of July 2012, respectively (Appendix Tabs. 1–3). EV69 is the most closely investigated warm event (e.g., Nghiem et al., 2012; Bennartz et al., 2013; Tedesco et al., 2013; Neff et al., 2014; Bonne et al., 2015), where surface melt occurred up to Summit Station at 3216 m, 72.58°N/38.46°W (Nghiem et al., 2012) and several new records were set (Tedesco et al., 2013). Considering all events, the maximum elevation with surface melt was 2692 ± 193 m. At this most elevated grid point, $T2M$ averaged at -3.5 ± 1.8°C during the entire warm events, but maximum $T2M$ was on average close to zero degrees, with -0.2 ± 1.3°C.

We group the warm events into two groups to investigate the change of their main characteristics over time. According to the IPCC Special Report on the Ocean and Cryosphere in a Changing Cliamte (SROCC) reference periods, we group "present day" (2005–2015) and "recent past" (1986–2005) warm events. These periods refer to the hydrological year that starts in October and warm events as defined here occur in JJA. So the "recent past" period lasts from Oct 1985 through Sep 2005 and "present day" period from Oct 2005 through Sep 2015. There were 35 and 28 warm events in the "recent past" and the "present day", respectively.

Normalized histograms (Fig. 3.5) show trends of (a) warm event duration, (b) maximum elevation and its spatial extent by (c) minimum and (d) maximum melt extent.
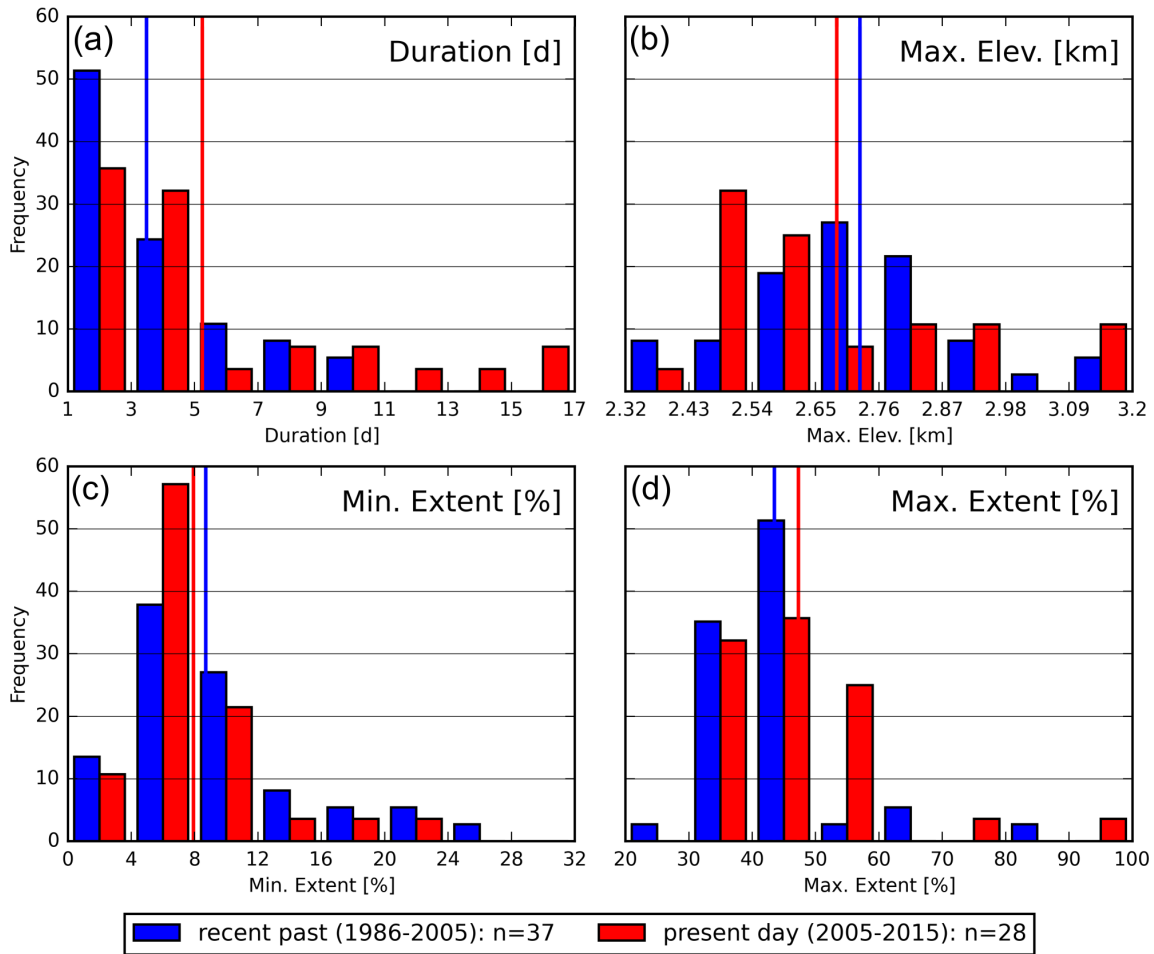
Figure 3.5: Normalized frequency histograms of (a) duration, (b) maximum elevation, (c) minimum elevation and (d) maximum extent of all warm events during the "recent past" (blue) and "present day" (red), according to the IPCC Special Report on the Ocean and Cryosphere in a Changing Cliamte (SROCC), respectively. Vertical lines denote the warm event average during each period.

First of all, in the "present day", warm events have become almost twice as frequent as in the "recent past", increasing from 1.75 (=35/20) to 2.8 (=28/10) warm events per year. This results from anthropogenic climate forcing, as it is evident that the Arctic warms as a response to climate change (Johannessen et al., 2004), warming is greatly attributable to human emissions (Gillett et al., 2008) and global land ice loss as well (Marzeion et al., 2014, 2018). Also, the persistent circulation anomaly of the European American North Atlantic region during the 2000s have caused a substantial amount of warming, with respect to NAO− (e.g., Fettweis et al., 2013) but also extremely high GBI+ during 2005–2015 (Hanna et al., 2018).

With climate warming, we would expect a shift of all four distributions towards

more positive values. This is the case for the longest events, which became longer, and the most extensive events, which spanned more and higher elevation ranges of the GrIS in the "present day" relative to the "recent past". But there is no such tendency for the minimum warm event extent. For all four quantities, we find that the lowest percentiles of the distribution increased, i.e., the frequency of events spanning 1–3 d (Fig. 3.5a), having a maximum elevation of 2320–2430 m (Fig. 3.5b), showing a minimum melt extent of 0–4% (Fig. 3.5c) and a maximum extent of 20–30% (Fig. 3.5d) decreased between 1986 and 2015. Except for an increase in frequency and duration, however, there is no clear shift of the whole distribution or the average over the reference periods.

3.3 GrIS Melt Climatology

During 1979–2017, summer melt showed a strong and approximately symmetric cycle peaking in mid-July, as expected from the pronounced annual solar variation. This cycle translates to the individual times of the day at 00, 06, 12 and 18 UTC (Fig. 3.6a). At 18 UTC, melt typically reaches the daily maximum extent with a maximum 39-yr median of 33.6% on 7 July. At this time of day, melt extent varied also strongest over the study period with a JJA average IQR of $8.9 \pm 2.1\%$ (average $\pm$ one standard deviation over the 39 yrs). JJA-averaged 06 UTC melt extent resembles the daily minimum with a median of $3.8 \pm 2.1\%$ over the years, with lowest variability (IQR = $3.7 \pm 1.3\%$). Time steps 00 and 12 UTC each show transition states between the two extremes with JJA melt area median of $6.3 \pm 3.0\%$ and $18.5 \pm 6.3\%$ of the GrIS, respectively, and intermediate variation. The pattern of more extensive and more strongly varying melt during daytime is similar for the 58% of the GrIS area above 2000 m. What is different is that melt occurs very rarely. In most of the years, melt does not reach above 2000 m at 00 and 06 UTC at all (JJA melt extent median = 0%). Of the higher elevated area, only $1.5 \pm 1.2\%$ is typically melting at 18 UTC.

The differentiation of total melt extent and melt extent above 2000 m, hereafter high elevation melt extent, highlights a peculiarity of the warm events as defined in this study (Sec. 2.2). While some of the warm events maximally spread over an area comparable to the normal 18 UTC total melt extent (Fig. 3.6a), they all lie above the 75th percentile in terms of high elevation melt extent (Fig. 3.6b). For most events, their maximum total and high elevation melt extent correlate well. But for some events, not
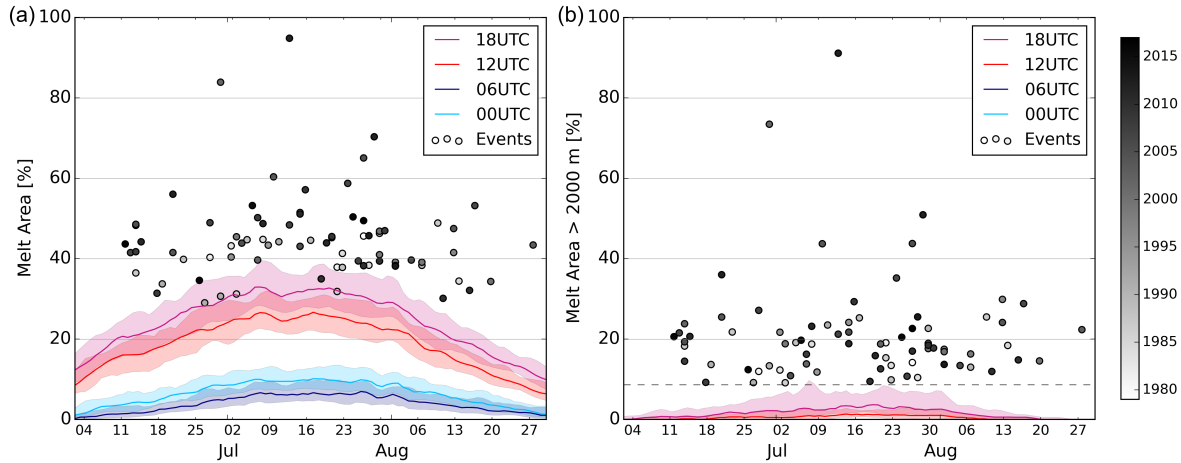
Figure 3.6: Climatological evolution of the melt extent for (a) all of the GrIS area and (b) that elevated above 2000 m. Reference is (a) the total GrIS area and (b) the total GrIS area above 2000 m, respectively. Solid lines denote the median and the shaded area represents the inter-quartile range of 1979–2017. Circles show the maximal melt extent of each warm event, colored according to the year it occurred in. The dashed line in (b) denotes the warm event area threshold.

the total melt extent is extraordinary, but only the high elevation melt extent. During those events, some of the typically warm regions, such as the coastal ablation area, remained cold with $SKT < -1°C$, while other, high elevated parts of the ice sheet melted instead. Such conditions prevailed, for example, during EV73 in July 2015, when the northern GrIS experienced above-normal surface temperatures and runoff, while the southern GrIS remained cold (Tedesco et al., 2016b). This points to the necessity of addressing the regionality of warm events (Sec. 3.5), as the impact of synoptic drivers likely varies over the whole GrIS.

3.4 Warm Event EV69

Warm event EV69 includes the most extreme period of surface melt in terms of elevation – up to the highest grid cell with 3175 m average elevation – and coverage: 94.8%. It lasted from 18 UTC 2 July to 18 UTC 17 July 2012.

3.4.1 Synoptic Situation

In general, the 15.25 days of EV69 were characterized by high SLP over the GrIS, visible in the 7 d average surface pressure charts in Figs. 3.7a,c,e. During 2–11 July, an atmospheric blocking over the Azores dominated the North Atlantic region, very

similar to Figs. 3.7c,d. The state of the atmosphere then returned to a more zonal flow with cyclones passing South Greenland, while a tropospheric cutoff and surface anticyclone, i.e., blocking, remained over the GrIS (Figs. 3.7e,f). Ubiquitous during JJA 2012 was an exceptional drought and heat wave in North America (Hoerling et al., 2014; Neff et al., 2014), evident from the near surface warm anomaly in Figs. 3.7a,c,e. Already before, as shown in Figs. 3.7a,c from 18 UTC 25 June to 12 UTC 9 July, the near surface warm anomaly over the Central and Eastern US deviated mostly by more than two standard deviations from the 39-yr THCL1 climatology. Additionally, the 14.25 d lasting EV68 ended only three days before the onset of EV69 and is still visible in the 18 UTC 25 June +7 d average (Fig. 3.7a). The near surface hot extreme ($> 2\sigma$) affected South and West Greenland and also large parts of Nunavut in the northern-most Canadian Arctic.

The week prior to the event (Figs. 3.7a,b), including the last four days of EV68, was in many ways similar to the central period of EV69 (transition between Figs. 3.7c,d and 3.7e,f). Increased $Z500$, named ridge DS (Davis Strait), and a positive temperature deviation larger than two sigma from THCL1 dominated the high latitudes. Towards the end of EV68, however, ridge DS was not kept up and the upper-level forcing for higher surface pressure over Greenland was reduced. Also, the positioning of the ridge and the associated warm anomaly were shifted westwards, which is why the surface signal mostly affected the Nunavut region and Southwest Greenland. The slightly different location and the shorter live span of ridge DS in the end prevented EV68 from becoming as extensive as EV69 (Appendix Tab. 3).

After the onset of EV69, the northward stretching Azores High developed to a North Atlantic blocking. The westerly flow was blocked throughout the troposphere. Below the southward extending trough over Newfoundland (NF), favoring cyclogenesis, dominant low pressure gave rise to one pronounced cyclone, hereafter cyclone NF. Cyclone NF grew in intensity and size, reaching a core SLP of around 990 hPa between 8 and 9 July (not shown). It amplified the Z500 ridge through upward and northward transport of low PV air and, together with cyclone EU over the British Isles and Scandinavia, stabilized the Atlantic block until 11 July. The former was also related to strong meridional moisture transport to the GrIS and rain in South and West Greenland up to high latitudes (Nghiem et al., 2012; Fausto et al., 2016). Then, a GrIS
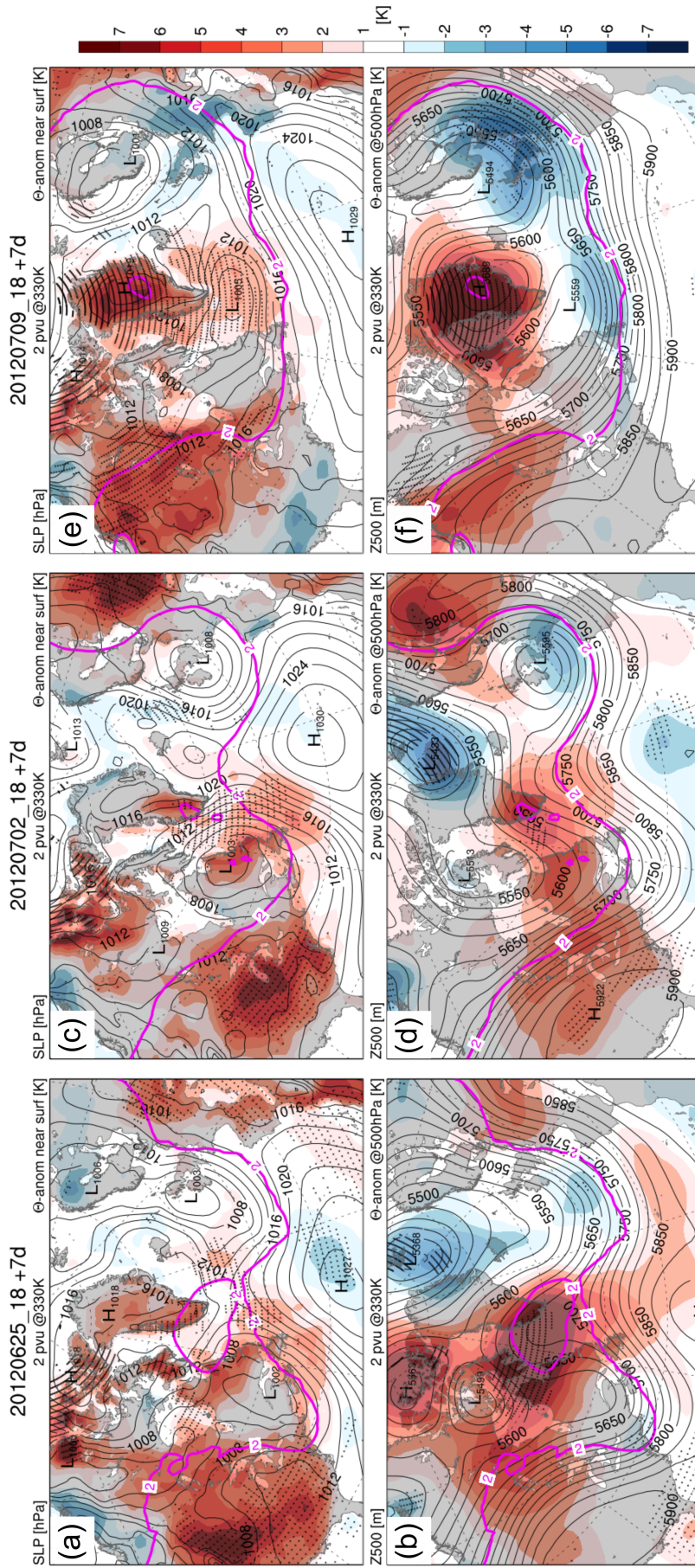
Figure 3.7: Seven day averages of synoptic fields during (a),(b) 18 UTC 25 June 2012 +7 d, (c),(d) 18 UTC 2 July +7 d, (e),(f) 18 UTC 9 July +7 d. The upper row (a),(c),(e) shows $TH10M$ anomalies from the long term climatology THCL1 in colors and contours of SLP. The lower row (b),(d),(f) shows the 500 hPa potential temperature ($TH500hPa$) anomaly in colors and contours of 500 hPa geopotential height ($Z500$). The 2 PVU line is shown in solid purple. Stippled areas denote grid points where $TH10M$ is outside the climatology ± two standard deviations during at least 50% of the seven days.

anticyclone intensified northeast of the region with high $Z500$ with maximum SLP of $\sim$1030 hPa. The strong, zonally oriented pressure gradient in between directed lower latitude air masses towards the GrIS. Near the Labrador Sea, the $TH10M$ anomaly grew to 4–5 K by 9 July (not shown). Including some foehn effects in South and West Greenland, which deviated the flow to the west (Nielsen, 2010), a southerly flow developed all along the Greenland west coast.

The NF ridge, visible as high $Z500$ and below 2 PVU air masses on the 330 K isentrope (Fig. 3.7d), expanded up to around 80°N during the blocking situation (not shown). The meandering $Z500$ pattern resembles a breaking Rossby wave over the Labrador Sea in the early second half of EV69. It fostered the formation of a tropospheric cutoff centered over the GrIS or rather a Greenland blocking, which was present over the following seven days (Fig. 3.7f). Also, the still stationary cyclone NF moved northwards before dissipating on 12 July (not shown).

While South and West Greenland were already influenced by moist-warm air masses, North Greenland remained rather cold during the first half of EV69. The persisting low $Z500$ even went along with an extraordinary $TH500hPa$ cold anomaly in Svalbard and East Greenland (Fig. 3.7d), associated with slightly colder to normal $TH10M$ (Fig. 3.7c). In the same period, air masses of on average +1 K to +4 K $TH10M$ anomaly in the Labrador Sea area was constantly advected north, into a climatologically colder region and therefore growing in magnitude. The anticyclonic flow onto the North GrIS let the warm anomaly spread over all of the GrIS (Fig. 3.7e). $TH10M$ anomaly was +1 K to +8 K during 11–13 July, higher in North and East Greenland. At 500 hPa, the Greenland blocking situation was stabilized by troughs NF and EU, over the Labrador and the Norwegian Seas, respectively. The $TH500hPa$ warm anomaly going along with the blocking was up to +9 K on average over 7 d. Both near the GrIS surface and at 500 hPa, the potential temperature anomaly was among the most extreme 3% during most of the 18 UTC 9 July +7 d period (stippled area in Figs. 3.7e,f). Such extreme $TH10M$ anomalies further affected large oceanic regions around Greenland, including the Labrador Sea, Davis Strait, Baffin Bay and Denmark Strait to the South, respectively, and the Wandel Sea to the North. After the event peak, air masses dried off all over the GrIS and set an end to the precipitation concentrated along West Greenland. The warm event ended concomitant with a weakening of the
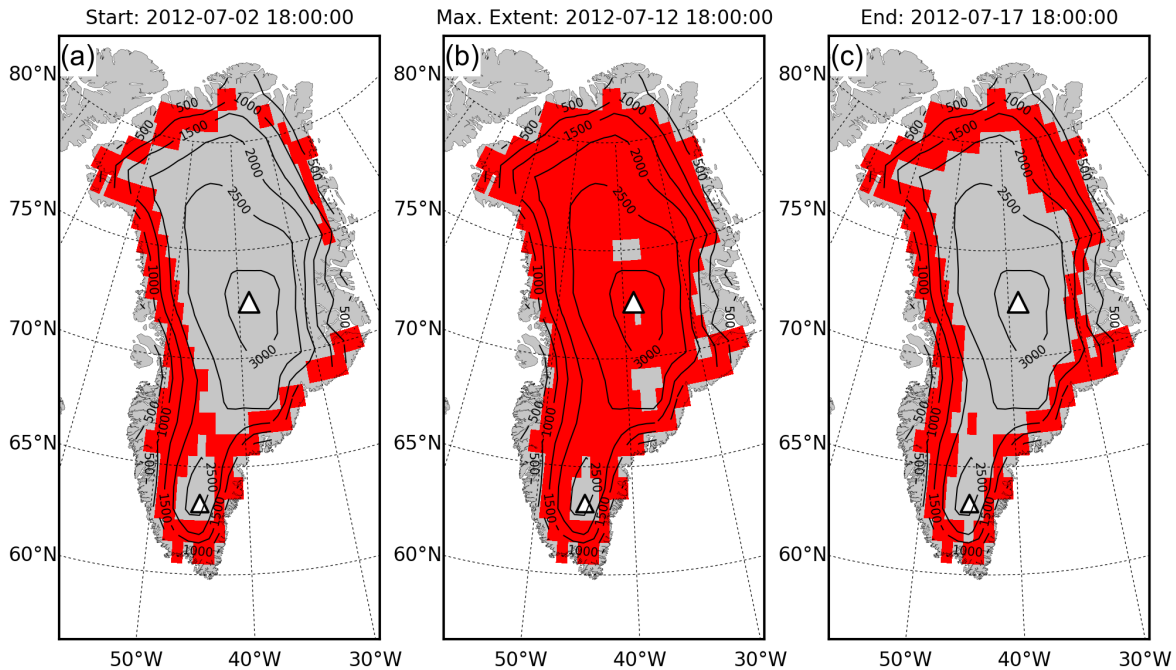
Figure 3.8: Melt extent during EV69 at (a) the beginning of the event at 18 UTC 2 July 2012, (b) maximum extent at 18 UTC 12 July and (c) the end of the event at 18 UTC 17 July. Melt area is shown in red. Contours represent 500 m spaced elevation contours and the two triangles denote Summit and South Dome location.

meridional surface flow over the Labrador Sea. The existing warm pool west of the GrIS was depleted to $<+4$ K by 12 July, and back to normal around 16 July (not shown). Thereafter, the GrIS blocking situation decayed completely, i.e., colder air masses were directed towards Southeast Greenland, the tropospheric cutoff was depleted and the anticyclonic flow onto North Greenland weakened. On 17 July, GrIS near surface potential temperature anomalies reduced to $+0$ K to $+5$ K (not shown).

3.4.2 Surface Melt

In terms of surface melt, the onset of EV69 happened in South Greenland, where melt already reached above 2000 m elevation at 18 UTC 2 July (Fig. 3.8a). Also the western GrIS, where warm air masses arrived early in EV69 (Sec. 3.4.1), was affected by the warm event up to 2000 m. The Northeast remained cold for a longer time due to the initially northwesterly flow discussed before. The peak of EV69 on 11–12 July was characterized by very high melt extent. During nighttime between 11 and 12 July, the North GrIS kept melting up to 2500 m (not shown), whereas the South GrIS was almost entirely frozen down to the lowest elevations. At that time, melting of the northern GrIS was accompanied by rain up to 2500 m (Nghiem et al., 2012). Then at 18 UTC

12 July melt stretched over 94.8% of the ice sheet (Fig. 3.8b). This number found here compares well with the 98.6% detected by satellite sensors on the same day (Nghiem et al., 2012). In the later stage of EV69, the dominant melt areas were located in North and Northeast Greenland. This is still evident at the last time step of EV69 shown in Fig. 3.8c, when northerly regions of the ice sheet melted up to 2000 m, as in the very South of Greenland.

3.4.3 Trajectory Analysis

The trajectory analysis reveals more details about the previously introduced synoptic weather development (Sec. 3.4.1) and the air mass evolution during transport, which both can indicate potential sources of air mass warming. To understand the different flow patterns and their significance for EV69, we first present the location of trajectories that will end up 20, 40 or 60 hPa above the entire GrIS during EV69 – not only that of trajectories with $SKT_{final} \geq -1°C$. Afterwards, we show the evolution of pressure, (potential) temperature and relative humidity along the trajectories that eventually caused melt over the GrIS.

Trajectory Location

Considering 10 d backward trajectories, the first air masses relevant to EV69 are identified at 18 UTC 22 June. The DS ridge, indicated by low tropospheric PV stretching isentropically northwards, extended over the Baffin Bay and high pressure dominated over most of the GrIS (Fig. 3.9a). It also represents an atmospheric Rossby wave and the weak and strongly meandering jet stream at that time. Northward advection directed warm air to Newfoundland and the high-latitude Canadian Arctic (see Sec. 3.4.1, Figs. 3.7a–d). These warm pools, largely more than two standard deviations above THCL1, are the main source region of early phase EV69 air masses (Fig. 3.9b). After the Rossby wave over Newfoundland broke, a more zonal flow from the North American east coast over the North Atlantic developed temporarily, relevant to the transport of low-level EV69 air masses (Figs. 3.9c–f). Other air masses originated from just above Greenland and a small branch was located above the colder than usual Scandinavian peninsula. These air masses were higher up in the atmosphere, i.e., still prone to thermodynamic modification before arriving at the GrIS.
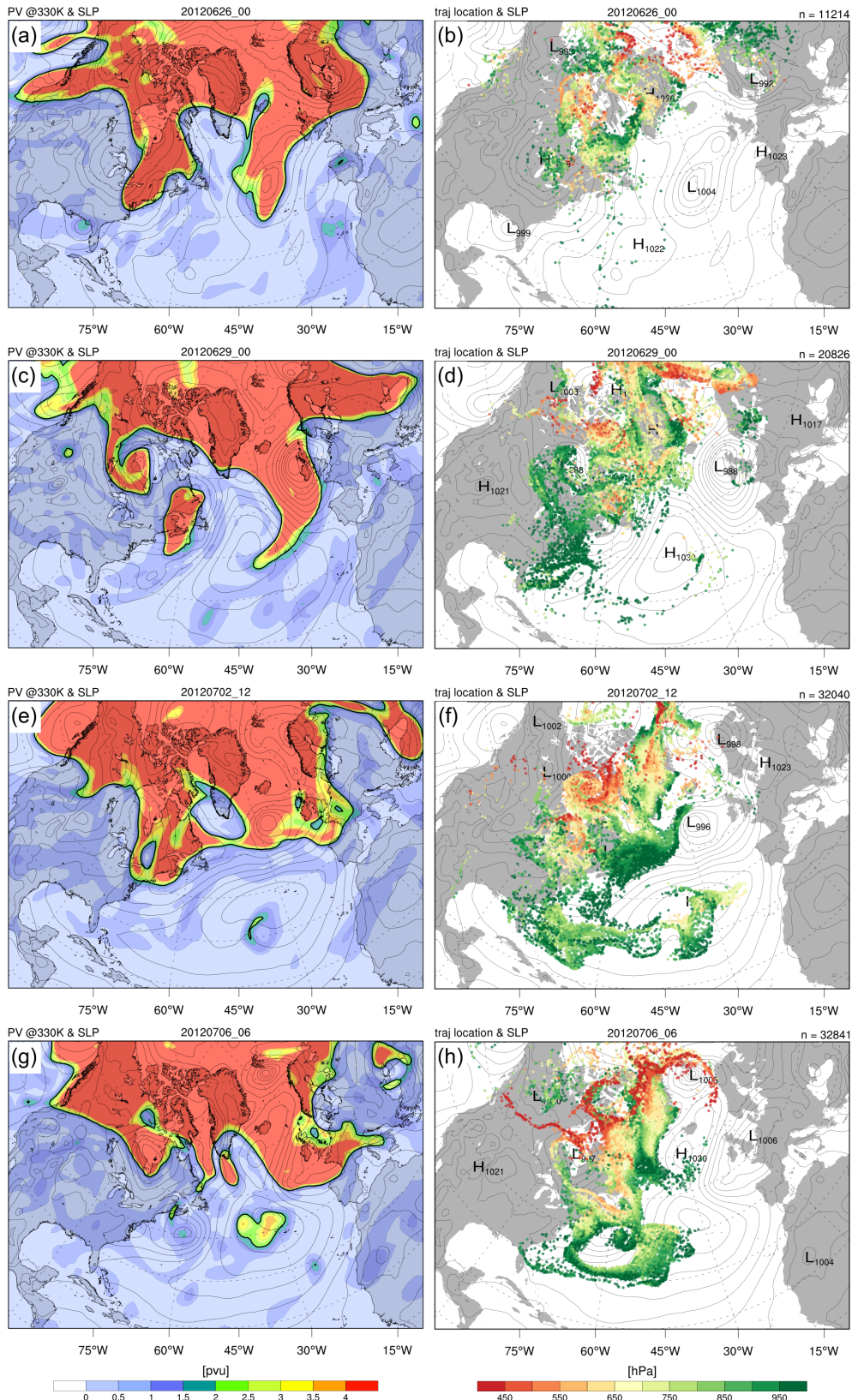
Figure 3.9: The left column (a),(c),(e),(g) shows PV on 330 K in colors and the 2 PVU contour in solid black. Dots in the right column (b),(d),(f),(h) show the location of trajectories that later end up in EV69, colored according to their pressure level. Thin black contours denote SLP in all panels. Rows indicate different time steps; (a),(b) 00 UTC 26 June 2012, (c),(d) 00 UTC 29 June, (e),(f) 12 UTC 2 July and (g),(h) 06 UTC 6 July.

After the onset of EV69 at 18 UTC 2 July, the westerly flow from North America became more and more blocked (Figs. 3.9g and 3.10a) and many air masses located between ∼20–55°N over the North Atlantic were in the pipeline for the peak phase of EV69 (Figs. 3.9f,h). Near surface air over the North Atlantic was 1–5 K above its THCL1 all along the east coast north of 30°N (not shown). The peaking of the ridge coincided with the sealing off of the southerly flow and EV69 air masses located poleward of ∼50°N (Figs. 3.10a–d).

Still, the warm event lasted seven more days, during which a stationary anticyclone over the GrIS was present (Figs. 3.10e–h). This Greenland blocking tapped air masses from upper levels (down to ∼400 hPa) that descended in the large-scale subsidence. In addition, a small stream of trajectories was transported rather close to the surface over the slightly warmer than usual North Pole area.

The trajectory location, especially its pressure level, illustrate some different synoptic features contributing to EV69. (i) Some air parcels, mostly associated with a cyclone, were located around 400–500 hPa or even higher prior to, or in the early phase of EV69. During the following days, they spiraled down by about 200–400 hPa in a cyclonic manner, likely indicating dry intrusion air streams (Wernli and Davies, 1997; Raveh-Rubin, 2017). (ii) Only a small group of trajectories originated from, or came across the Great Plains (Figs. 3.9d,f). A larger group of trajectories was located above eastern North America around 29 June, where the heat wave was present as well, with extensive near surface temperature anomalies of +10 K. Over the whole event, however, these parcels only made up a small fraction of all trajectories. The western subtropical North Atlantic or even the Azores High itself were larger contributing regions of air masses (Figs. 3.9f,h and 3.10b). (iii) After the peak of the warm event on 11–12 July, the entire remaining trajectory set showed little horizontal movement and, if at all, was mainly descending within the large-scale blocking subsidence over Greenland. (iv) In contrast, the trajectory movement before the event peak was fast with around 1300 km/d, in agreement with the strong horizontal pressure gradient ahead of the Canadian east coast.

So again, as in Sec. 3.4.1, we can identify the two weather systems relevant to almost all the trajectories. The first half of EV69 (Figs. 3.9g,h and 3.10a–d) was
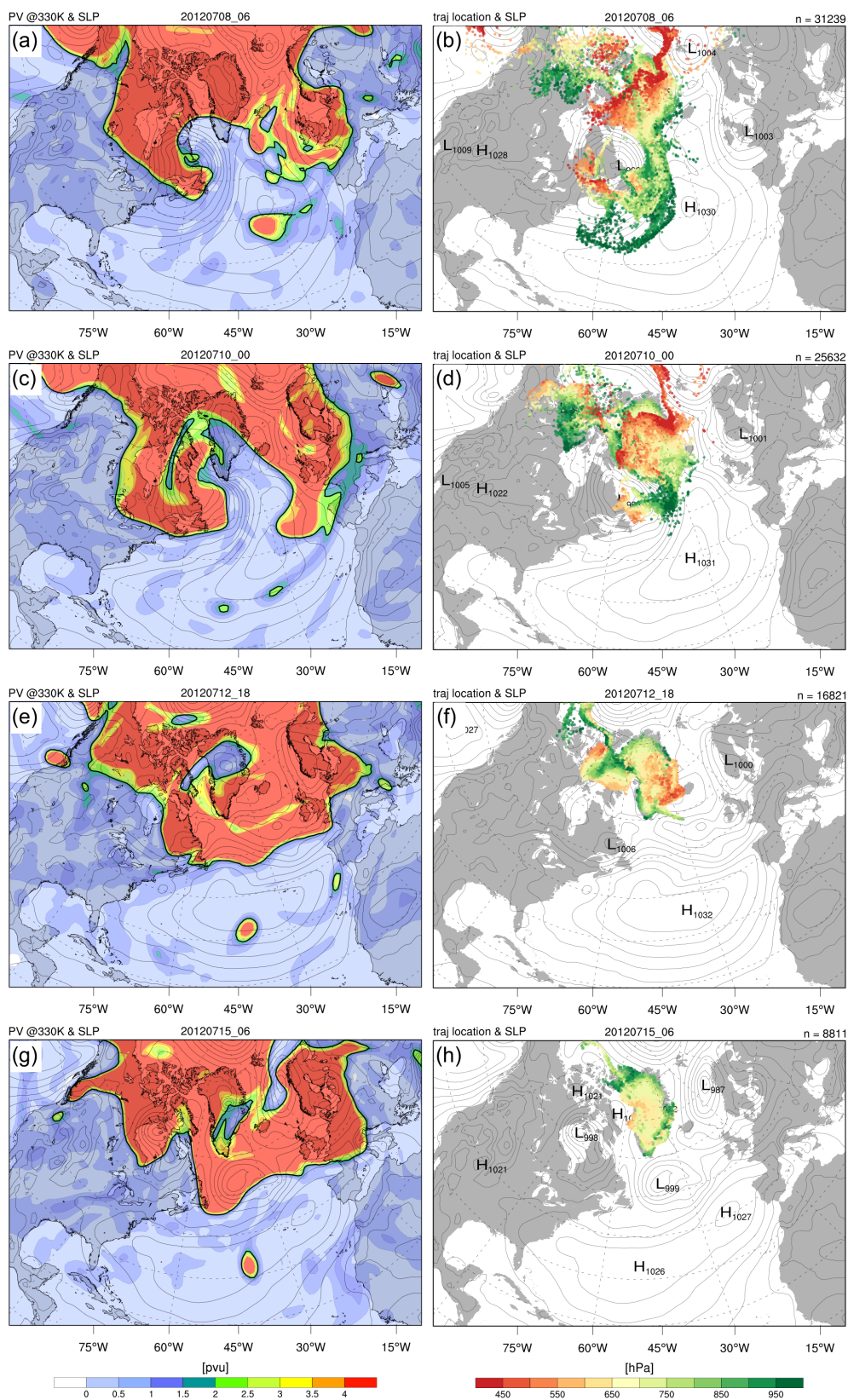
Figure 3.10: The same as Fig. 3.9, but for time steps (a),(b) 06 UTC 8 July 2012, (c),(d) 00 UTC 10 July, (e),(f) 18 UTC 12 July and (g),(h) 06 UTC 15 July.

dominated by the prominent NF low pressure system, blocked by the Azores High, and a strong pressure gradient in between. The jet stream was weak and the flow over Greenland primarily meridional. A $TH10M$ warm anomaly of 4–5 K had accumulated at the surface of the Labrador Sea by 9 July, and that of $TH500hPa$ peaked over South Greenland with +9 K. Then during the second half (Fig. 3.10e–h), a tropospheric cutoff at upper levels and a surface Greenland blocking anticyclone were the dominant features located over the central to northern GrIS.

Air Mass Evolution

When grouping the trajectories according to Sec. 2.3.3, 37% of all trajectories of EV69 fall into categories 1–4, i.e., where $SKT_{final} \geq -1°C$ ("warm" trajectories). Remember, that the trajectories summarized in Figs. 3.11 and 3.12 end up 20, 40 and 60 hPa above ground level (agl) and their final temperature can thus deviate substantially from 0°C. The relative occurrences of each category of all "warm" trajectories are: 19% C1, 5% C2, 36% C3 and 40% C4.
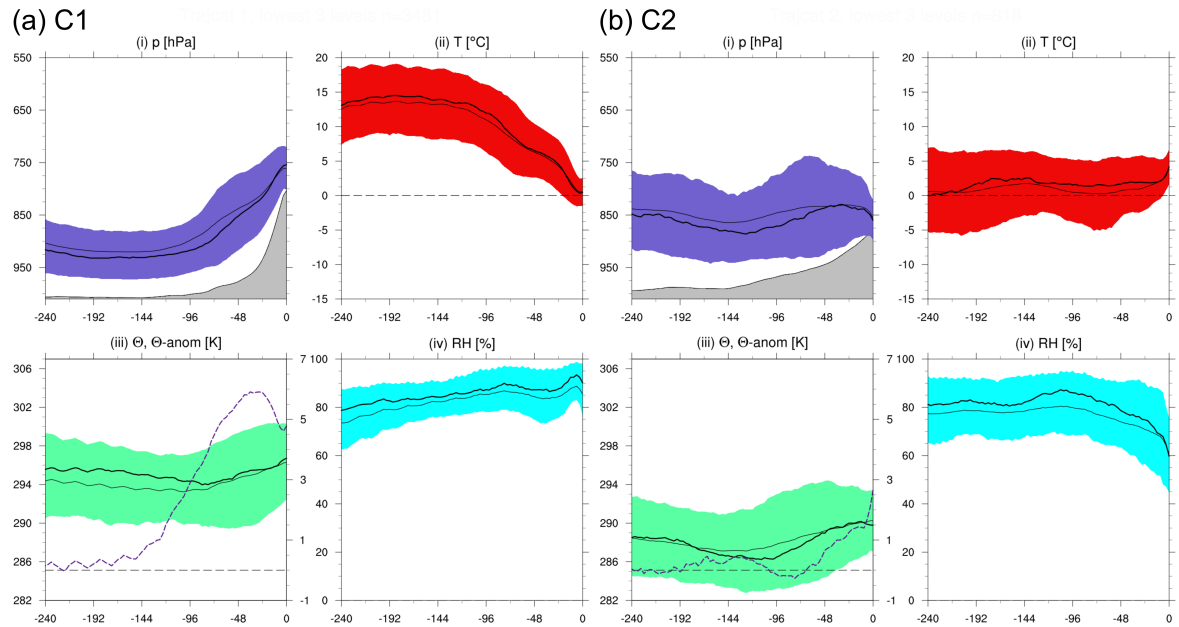
Figure 3.11: Evolution of (i) pressure (p), (ii) temperature (T), (iii) potential temperature (Θ) and its anomaly (Θ_{anom}) and (iv) relative humidity (RH) along all trajectories of (a) category 1 (C1, $n = 3481$) and (b) category 2 (C2, $n = 818$). Thick black lines show the median, thin ones the average and the color fill the inter-quartile range, respectively. Θ_{anom} median is shown with respect to THCL1 as purple, dashed line with a secondary axis (zero-line grey, dashed). The abscissa labels indicate time [h] before arrival on the GrIS. The grey area in (i) represents average surface pressure.

C1 (Fig. 3.11a) is most surprisingly found as a substantial contributor to the warm event. Within about the last four days, the trajectories rose by $\sim 150\,$hPa on average (Fig. 3.11a$_i$). This is due to the GrIS topography with an ice sheet margin that is sloping by around 2%. If synoptic conditions favor transport towards the ice sheet, the air deviates laterally or ascends onto the ice sheet. Most of C1 trajectories are lifted above resident coastal air masses and arrive at 40 or 60 hPa agl (Fig. 3.11a$_i$). This implies, that the air masses most directly responsible for surface melting (20 hPa agl) primarily sourced from a different category than C1. Still, the majority of trajectories arrived with a temperature greater than 0°C. The positive arrival temperature despite the adiabatic cooling during ascent likely roots in the high temperature (~ 13°C) when arriving at the Greenland coast at $-96\,$h (slope in Fig. 3.11a$_i$) and the fast transport or diabatic heating. Indeed, a striking property of these air masses is the high relative humidity all along the way (Fig. 3.11a$_{iv}$), likely also related to the observed rain events (Fausto et al., 2016). So the ascent went along with diabatic heating that balanced the longwave cooling. These effects resulted in a quickly growing potential temperature anomaly over the ascending topography (Figs. 3.11a$_i$ and 3.11a$_{iii}$). Further, many trajectories experienced a first strong ascent (bump, especially in the pressure curve) over the southern tip of the ice sheet (not shown), where pressure decreased quickly and most of the Θ-anomaly arose. In the end, they were 4.5 K warmer than THCL1, which is the strongest Θ-anomaly median of all four categories. Also, the final pressure level of C1 is with $\sim 750\,$hPa highest among all categories, i.e., C1 represents the trajectories arriving high up on the GrIS.

The least numerous trajectory group was C2, with a contribution of only 5% (Fig. 3.11b). Most of these air masses originate from Greenland's surroundings and arrive in coastal regions of the GrIS (not shown). This is why they generally show weak changes in all parameters shown in Fig. 3.11b. Some of them descend, others ascend, but on average they show weak vertical motion (Fig. 3.11b$_i$). The Θ-anomaly of C2 trajectories grows in the last two days, when most air masses become warmer than the climatology (Fig. 3.11b$_{iii}$). But as they arrive mostly in the typically warm coastal regions of the GrIS, the temperature anomalies are the lowest of all four categories. The slight increase in potential temperature (Fig. 3.11b$_{iii}$) points to a diabatic heating source, as the pressure decrease does not go along with a decrease in temperature (Figs. 3.11b$_i$ and 3.11b$_{ii}$). This is likely related to latent heating during condensation,
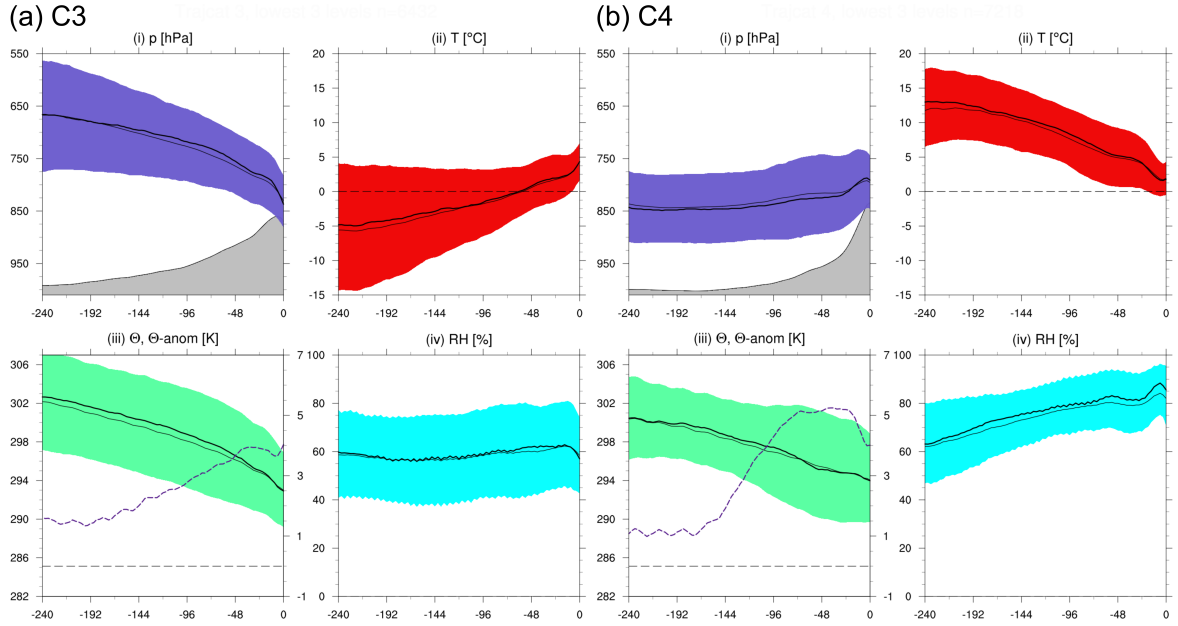
Figure 3.12: The same as Fig. 3.11, but for (a) categories 3 (C3, $n = 6432$) and (b) 4 (C4, $n = 7218$).

as relative humidity indicates the presence of clouds ($RH > 80\%$) – even more clearly during that period (Fig. 3.11b$_{iv}$). In the very end, a slight adiabatic descent reduces RH, increases T and lets the Θ-anomaly peak at around $+2.5\,\mathrm{K}$.

During the first few days of the event, C3 trajectories were rare. Afterwards, C3 was dominated solely by a substantial amount of cyclonically descending air masses until arrival date 8 July. The descent occurred from below $450\,\mathrm{hPa}$ in the surroundings of Nunavut cyclones and trajectories turned by 360–$720°$ (not shown). These air parcels arrived in Southwest Greenland and were accompanied by subtropical C3 air masses between 8–14 July, which in turn made C3 the most numerous trajectory group in the end phase of EV69 in Northeast Greenland. These second contributors of C3 air masses experienced direct northward transport and subsidence over the GrIS, mostly starting from somewhat lower levels between 600–$900\,\mathrm{hPa}$. On average, these parcels' temperature increased by $9°\mathrm{C}$ and potential temperature decreased by $10\,\mathrm{K}$ (Figs. 3.12a$_{ii}$ and 3.12a$_{iii}$). The descent of around $200\,\mathrm{hPa}$ (Fig. 3.12a$_i$) went along with clear-sky radiative cooling (decrease in Θ) and overcompensating adiabatic warming causing the increase in T. The final height of the trajectories was around $850\,\mathrm{hPa}$ and close to the ice sheet surface. The initial potential temperature of the air parcels at $-10\,\mathrm{d}$ was already $2\,\mathrm{K}$ above THCL1. Combining this anomaly with the trajectory

location at that time, we confirm the upper-level warm anomaly over the Canadian Arctic and lower-level warm anomaly over the western subtropical North Atlantic as source regions. Afterwards, this anomaly grew with a constant rate to up to $+4\,$K. A clear distinction to the other categories is the low saturation of these air masses – the relative humidity of most trajectories was far below the cloud range of 80–100% (Fig. 3.12a$_{iv}$). This is a logical consequence of drying downward motion (Fig. 3.12a$_{iv}$) and implies that there were, apart from radiative cooling, no significant diabatic processes acting on these air parcels.

C4 was together with C3 the most important group contributing to the warming during EV69. Similar to C3, these air masses arrive at around $800\,$hPa, rather close to the GrIS surface and show a final potential temperature anomaly of $+4\,$K (Figs. 3.12b$_i$ and 3.12b$_{iii}$). What was different is the contrarily evolving temperature and thus relative humidity (Figs. 3.12b$_{ii}$ and 3.12b$_{iv}$). The diabatic cooling of $6.5\,$K in C4 (Fig. 3.12b$_{iii}$) was slightly reduced compared to C3. The trajectories did not always travel under clear-sky conditions, as suggested by $RH > 80\%$, and possibly experienced mixing with warmer air masses. So in the last three days and before the trajectories slightly ascended onto Greenland (Fig. 3.12b$_i$), this processes hampered or offset radiative cooling. The evolution of the warm anomaly, which grew mainly between $-144\,$h to $-72\,$h, is more similar to C1 trajectories. Both categories, C1 and C4, include mainly subtropical air masses, which were initially warm with T IQR = 6–18°C (Fig. 3.12b$_{ii}$) and were advected into the climatologically colder region of the GrIS. Once C1 or C4 trajectories resided over ice, their Θ-anomaly no longer grew and dropped in the end due to a small ascent to higher regions of the GrIS. So C4 was as important as C3 and also affected similar regions, but the transport pattern and associated modifications were much more similar to C1.

3.5 Warm Event Analyses

In this section, we will analyze the 77 warm events in 1979–2017 with different methodologies. We define seven regions of interest, based on the trajectory starting locations (Sec. 2.3.2), as shown in Fig. 3.13. We then address the trajectory evolution of all warm event periods that were of importance for each region (Sec. 3.5.2), except for the Summit region, which is addresses separately (Sec. 3.5.1). The regions further serve as

basis for the synoptic assessment of specific weather features (Sec. 3.5.3) and a final quantification of the different warming mechanisms (Sec. 3.5.4).

The choice of the regions is mainly based on the eight Zwally basins (Fig. 2.1 in Sec. 2.1) and internal consistency in terms of elevation span around 2000 m. The Zwally basins are a highly practical reference for cryospheric studies, but do at the same time, besides hydrological flow patterns, capture general climatological characteristics. There is a clear east-to-west distinction due to orography, with the meridionally oriented ridging of the GrIS, representing the ice divide. Located in the North Atlantic storm track and with a height of ~3 km, the GrIS interacts with the upper atmosphere by wave interaction, distorts the westerly flow and causes several mesoscale and local phenomena like lee cyclogenesis (Petersen et al., 2003), tip jets or barrier winds (Renfrew et al., 2008; Våge et al., 2009; Harden and Renfrew, 2012). South-to-north contrasts arise mainly from the wide range of latitudes covered by the GrIS. While the GrIS southern tip is located at <60°N, about the same latitude as Oslo or Stockholm, its North comes closer than 1000 km to the North Pole and is distant from the North Atlantic storm track.

The first six boxes correspond to the Zwally basins as follows; Box SW to basins 5 and 6 (South-Southwest), box CW to basins 7 and 8 (West-Northwest), box NW to basin 1 (North), box NE to basin 2 (Northeast), box CE to basin 3 (East) and box SE to basin 4 (Southeast), respectively. The boxes span a similar elevation range, with lower elevations in the climatologically colder North of the GrIS, as summarized in Tab. 3.2. With elevation averages of around 2000 m, observing melt in most of the boxes is rather unusual. Histograms of the count of melt time steps for the 77 warm

Table 3.2: The table shows average (avg.), standard deviation (σ), minimum (min.) and maximum (max.) elevation [m] in ERA-Interim of the seven trajectory starting points in each box shown in Fig. 3.13.

	Box 1 SW	Box 2 CW	Box 3 NW	Box 4 NE	Box 5 CE	Box 6 SE	Box 7 S
Avg.	2218	2107	1883	1968	1995	2039	3120
σ	346	393	289	453	398	305	36
Min.	1770	1554	1452	1318	1508	1561	3045
Max.	2628	2564	2252	2484	2618	2412	3153
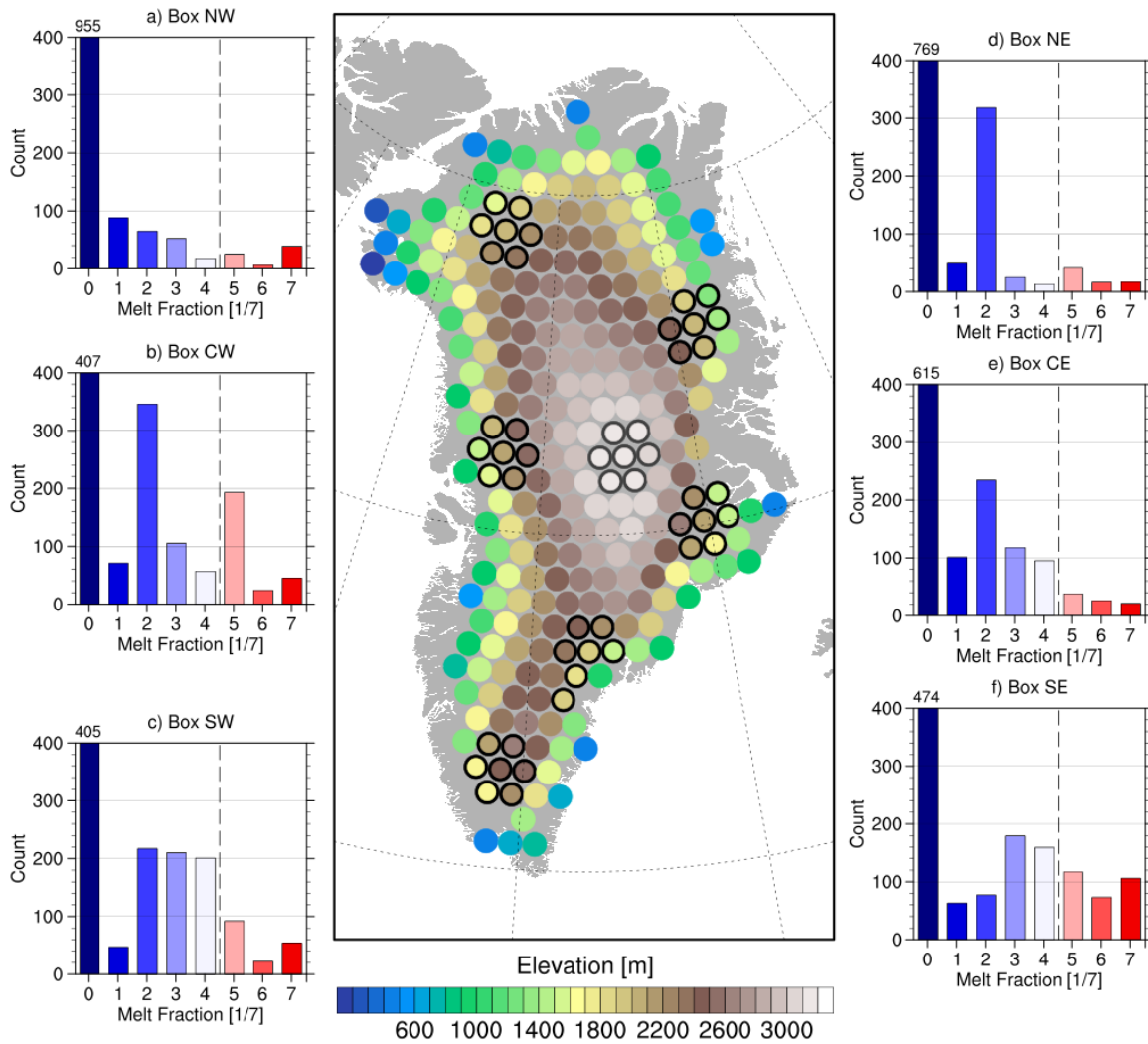
Figure 3.13: The map shows trajectory starting points colored according to their elevation. There are seven regions of interest (black/grey framed dots), each consisting of seven trajectory starting points. The panels show the count (number of 6 h time steps) of different melt fractions in six of these regions during all 77 warm events: (a) box "Northwest (NW)", (b) box "Central West (CW)", (c) box "Southwest (SW)", (d) box "Northeast (NE)", (e) box "Central East (CE)" and (f) box "Southeast (SE)". Vertical dashed lines show the threshold for detecting a melt event in each box. No histogram is shown for box "Summit (S)" (grey framed dots).

events (total $n = 1248$) show that the actual north-to-south melt gradient is not completely compensated by the elevation-adapted choice of the boxes (Figs. 3.13a–f). Melt fractions 5/7 to 7/7 are still two to three times less frequent in boxes NW and NE, compared to boxes SW and SE. But the choice helps to at least have some time steps, when melt occurred in the two northernmost boxes. Remember that the histograms only include time steps during warm events over Greenland. The numerous bin 0/7 in all histograms either denotes time steps during warm events that did not affect this

region or during nighttime of the events. Otherwise, the peaks of the distributions shown in Figs. 3.13a–f represent some inter-dependencies of the starting points within each box, mostly in terms of elevation.

The following analysis is based on the boxes defined in this section. For boxes SW...SE, we analyse the time steps, when melt was at least observed in five out of seven trajectory starting points of the region. Before that, we investigate the rare melt events around Summit Station in box S. Melt data is too scarce to apply our quantitative analysis methods, nevertheless, surface melt at high elevations of the GrIS is a main motivation for this study.

3.5.1 Summit Region S

Box S represents the dry inland plateau of the GrIS, i.e., Summit Station region. The average elevation of that box is 3120 m and none of the seven starting points lies below 3045 m (Tab. 3.2). No histogram is shown in Fig. 3.13, as melt occurred only seven times in that region during 1979–2017, of which five time steps belong to EV69 in 2012 (Tab. 3.3). During EV69, 11–13 July 2012 were the three days with most extensive melt, spreading over ∼90% of the entire GrIS and over >80% of the area above 2000 m. EV35 starting in June 2002 ranks second in terms of melt extent (84%), reaching up to 3156 m, while EV40 covered only 60% but affected the highest ERA-Interim grid cell of the GrIS at 3175 m – alike EV69 (Appendix Tab. 2). Even though these warm events were detected, as for example Hall et al. (2013) found a maximum melt extent of 87% for EV35, they have not been subject to more detailed research, despite parallels

Table 3.3: The table shows all time steps when melt occurred in box S together with the warm event they were part of and the observed melt fraction.

Date	Time	Warm Event	Melt Fraction
29 June 2002	18 UTC	35	1/7
9 July 2004	18 UTC	40	1/7
11 July 2012	18 UTC	69	2/7
12 July 2012	12 UTC	69	6/7
12 July 2012	18 UTC	69	7/7
13 July 2012	12 UTC	69	1/7
13 July 2012	18 UTC	69	5/7

to EV69. This is likely owing to a shorter peaking of wide-spread melt and shorter duration of EV35 and EV40 in general, of only 6.25 d and 7.25 d, respectively.

3.5.2 Trajectory Analysis

We here look at the evolution of air masses that ended up in the first six regions of interest (boxes SW...SE) when melt fraction was larger equal 5/7, analogous to Sec. 3.4.3.

Southwest GrIS

In the Southwest, significant melt was observed during 13% of the Greenland warm events. The general trend during these periods was a gradual but only slight descent of air masses between -10 d and -4 d (Fig. 3.14a). Then, the parcels remained approximately stationary in height, but ascended within the 24 hours prior to the event by around 100 hPa. Potential temperature decreased continuously due to radiative cooling until one day before the event (Fig. 3.14c). The median temperature T did not decrease until the very end, i.e., within the last 24 hours of strong ascent, when it dropped by around 8°C (Fig. 3.14b).

Despite the strong ascent and accompanying temperature drop within one day prior to the event, the air masses were around 5 K warmer than the climatology (Fig. 3.14c). Whit a rough calculation of DT/Dt by Eq. 2.3 (Sec. 2.3.3), we find that the ascent of $\sim$100 hPa at a temperature around 10°C ($\sim$283 K) causes a
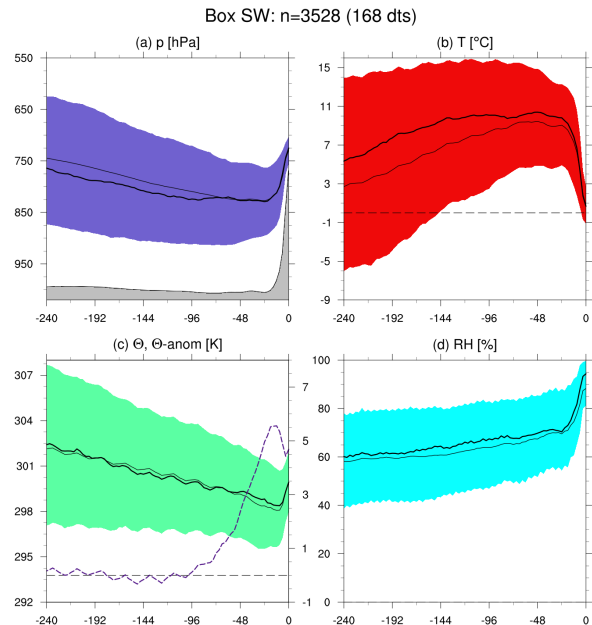
Figure 3.14: Evolution of (a) pressure (p), (b) temperature (T), (c) potential temperature (Θ) and its anomaly (Θ_{anom}) and (d) relative humidity (RH) along all trajectories arriving in SW warm events. Thick black lines show the median, thin ones the average, and color fill the inter-quartile range, respectively. Θ_{anom} median (purple, dashed line) is shown relative to THCL1 with a secondary axis (zero-line grey, dashed). The abscissa labels indicate time [h] before arrival. The grey area in (a) represents the average surface pressure. N denotes number of trajectories contributing and the number of time steps is shown in brackets.

~10°C temperature decrease. The remaining 2°C difference between the theoretical cooling due to vertical motion and the observed cooling, root in diabatic processes. There is a strong Θ-increase in the end of just about $2\,\mathrm{K}$, which is likely related to latent heat release during the ascent phase at the southern tip of the GrIS. Indeed, relative humidity increased to above 80%, confirming latent heat release (Fig. 3.14d).

From the strong increase in the potential temperature anomaly, it seems that transport is a very important process for warm events in Southwest Greenland (Fig. 3.14c). Transport either occurred very quickly or together with warming mechanisms opposing radiative cooling. As the majority of the trajectories is more than $200\,\mathrm{hPa}$ agl up to the day prior to arrival, they travelled in the absence of near-surface cooling by turbulent heat fluxes into the GrIS. The downward kink in the Θ_{anom}-curve in the very end is probably caused by advection into a climatologically warmer region. Air masses arrive with $T > 0$°C due to transport from climatologically warmer regions and diabatic warming due to the latent heat release during the final ascent.

Central West GrIS

Air masses that arrived in the western box had evolved similarly to those that arrived in box SW. The most striking differences are that air masses were less saturated (Fig. 3.15d) and the trajectories arrive earlier over topography, most likely the ice sheet, and therefore remain longer in its proximity (Fig. 3.15a). Average surface pressure increased at $-3\,\mathrm{d}$ instead of $-1\,\mathrm{d}$ for box SW. Also, the initial temperature and its increase to a median peak of $\sim$7°C during the first half of the trajectory evolution were not as strong (Fig. 3.15b). The median temperature of air masses at -4 d is around 3°C lower in the CW region than in the SW region. The reduced moisture content and earlier arrival in the ice sheet's proximity reflects in the slower ascent of the trajecto-
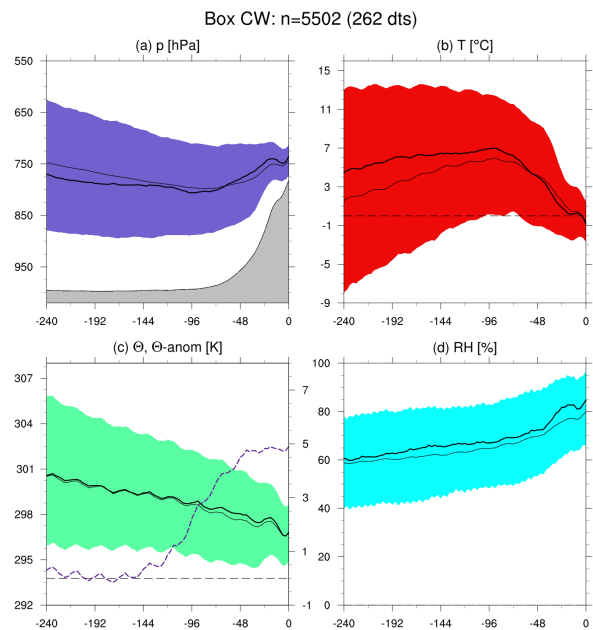
Figure 3.15: The same as in Fig. 3.14, but here for box CW (see Fig. 3.13). To facilitate comparison, axis limits are the same.

ries (Fig. 3.15a), slower and weaker temperature drop (Fig. 3.15b) and slower increase in Θ_{anom} (Fig. 3.15d).

Warm events significant to Central West Greenland are even more frequent than those to the Southwest, which is, however, mostly related to the box choice. 21% of the warm event periods cover box CW. And we deduce from the constant and slow decrease in potential temperature (Fig. 3.15c) that apart from radiative cooling at a rate of around $-0.4\,\mathrm{K/d}$, no diabatic processes were acting on these air masses until before $-2\,\mathrm{d}$. Then, as for box SW trajectories but to a lesser extent, diabatic warming by condensation occurred within the 48 h prior to arrival (Fig. 3.15d). The subtle vertical oscillation, causing fluctuations in the other parameters could also come from summarizing air parcels travelling in, and others slightly above clouds, respectively. The somewhat stronger decrease in Θ within the last day before arrival would then root in slightly enhanced cloud top cooling, as the trajectories remained relatively far above ground level.

Northwest GrIS

The trajectories arriving in the Northwest initially showed only weak vertical movement (Fig. 3.16a). Some of them descended slightly, but the median trajectory remained almost at the same pressure level during $-10\,\mathrm{d}$ to $-4\,\mathrm{d}$. This is represented by a more or less constant median temperature of 6°C (Fig. 3.16b) and only a slight decrease in Θ by radiative cooling (Fig. 3.16c). The latter is obvious from the diurnal fluctuation represented in Θ, also indicating that most of the air parcels were arriving at the same time of day (12 or 18 UTC) as the signal is not washed out over the 1470 trajectories.

The potential temperature anomaly
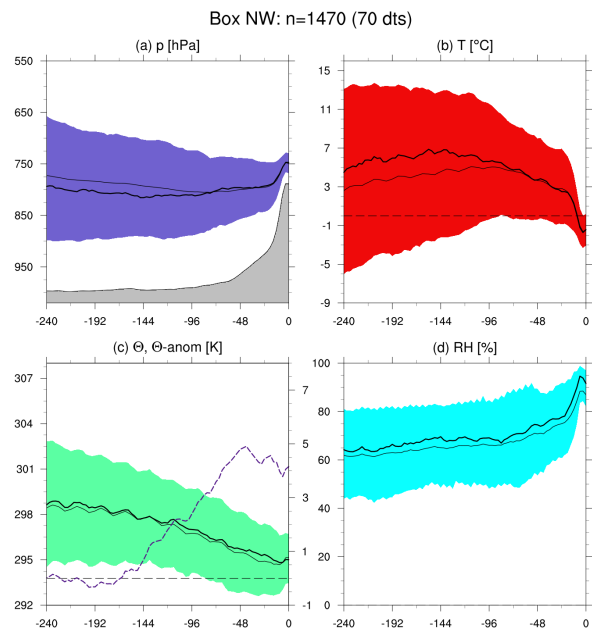
Figure 3.16: The same as in Fig. 3.14, but here for box NW (see Fig. 3.13). To facilitate comparison, axis limits are the same.

started growing earlier in time compared to boxes SW and CW, likely due to the stronger meridional transport to around 80°N (Fig. 3.16c). Also, merely 6% of the warm event periods were associated with melt in box NW. The ascent up to the box elevation, which mainly happened 24 hours prior to arrival (Fig. 3.16a), cooled the air masses substantially and reduced the final temperature of most air parcels to below 0°C (Fig. 3.16b). Consequently, the median relative humidity increased to over 90% and some condensational heat release was induced (Fig. 3.16d). Θ_{anom} finally was $\sim+4\,\mathrm{K}$.

Northeast GrIS

Box NE, the first one discussed on the eastern GrIS, differs from the previous boxes SW, CW and NW. First of all, the final Θ_{anom} of $+7\,\mathrm{K}$ is by about $2\,\mathrm{K}$ higher (Fig. 3.17d). This is a consequence of the GrIS, which usually (i) blocks the warm (south)westerly flow or (ii) cools air masses that make it close to the ice sheet surface to Eastern Greenland. Another difference is that the air parcels finally descend when they move into the climatologically colder region (Fig. 3.17a).
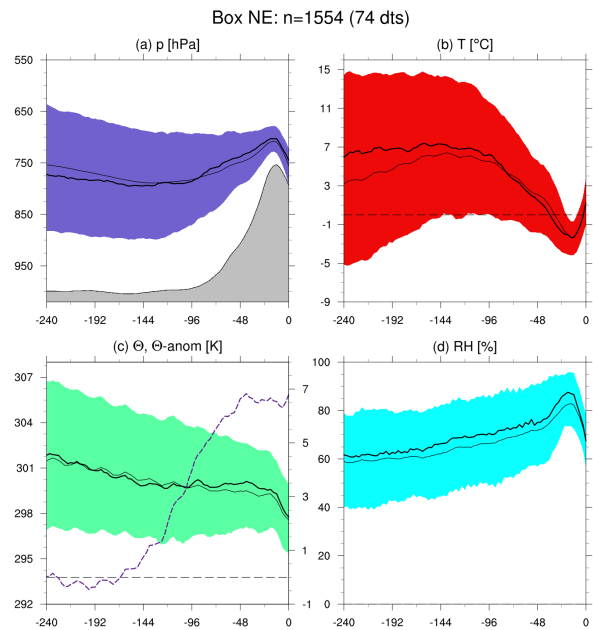
Figure 3.17: The same as in Fig. 3.14, but here for box NE (see Fig. 3.13). To facilitate comparison, axis limits are the same.

Between $-5\,\mathrm{d}$ to $-1\,\mathrm{d}$, the median trajectory ascended (Fig. 3.17a) and its temperature T decreased almost adiabatically (Figs. 3.17b,c). The rough estimate of changes in T are similar to that for SW warm events. The ascent of $\sim100\,\mathrm{hPa}$ would cause a ~10°C temperature decrease, but only a temperature decrease of around 8°C is observed. Over these four days, condensational heat release during cloud formation compensated longwave cooling. The median trajectory had a relative humidity peak of around 90% at –1 d (Fig. 3.17d). The compression within the last 24 hours then occurred together with evaporative cooling, as RH and Θ dropped along with respective changes in p and T. Θ_{anom} at the same time remained constant, despite the diabatic cooling, indicating the advection into a climatological colder region (Fig. 3.17c). As

northernmost region on the eastern GrIS, the frequency of warm events is as low as for box NW, namely 6%.

Central East GrIS

The peculiarity of CE warm event air masses was their altitude. Most of the trajectories did always remain below 750 hPa, i.e., higher up in the atmosphere (Fig. 3.18a). Also, Θ greatly lied above 300 K (Fig. 3.18c). Both is not the case for any of the other boxes (SE, CW, NW, NE, SE). Only in the very end, the median trajectory descended to just about this altitude of $\sim$750 hPa and 300 K. Otherwise, the trajectories are relatively diverse in terms of p- and T-evolution (Fig. 3.18b). Both descending and warming but also slightly ascending and cooling parcels were present in CE

Figure 3.18: The same as in Fig. 3.14, but here for box CE (see Fig. 3.13). To facilitate comparison, axis limits are the same.

warm events. These two kind of trajectories likely represent different pathways to the eastern GrIS: either from south along the eastern GrIS flank, or from the Northwest over the GrIS. The trend in Θ is more consistent, namely weak diabatic cooling at around -0.4 K/d (Fig. 3.18c). Only in the very end, other diabatic processes (again evaporative cooling) led to a short but sharp decrease in Θ. Relative humidity, however, was generally not in the range of where one would expect clouds (Fig. 3.18d) and the Θ-signal is thus only weak. The potential temperature anomaly of the trajectories is almost identical to that of region NE, but by about $+0.5$ K more positive overall (Fig. 3.18c).

The CE had the highest potential temperature anomaly during warm event periods of melt fraction 5/7 or higher (7% of all warm events). The final median temperature of $\sim$3°C is highest among all regions (Fig. 3.18b). Even those of box SW and SE are below 1°C. Region CE is neighbouring the Scoresbysund fjord, discussed in Sec. 3.1. During warm events in this box, air masses typically come from west of the GrIS. They

are only warm enough when arriving on the eastern GrIS, if the originate from the mid-troposphere. Hence, they have to descend afterwards, which induces adiabatic warming that is somewhat offset by evaporative cooling. Their behaviour seems related to the foehn effect, but is rather dynamically than orographically forced. Box NE showed similar air masses contributing, just with at a slightly lower Θ- and higher p-level and with stronger ascent and warming prior to crossing the GrIS ridge. For box NE trajectories, relative humidity was higher all along their way, especially did it mostly increase above 80% (smaller IQR) and likely more latent heating and evaporative cooling took place (Fig. 3.17d), compared to box CE trajectories (Fig. 3.18d).

Southeast GrIS

Box SE warm event trajectories are almost identical to those arriving in NW warm events. In the beginning, they hardly moved in the vertical but later ascended adiabatically by ~50 hPa (Figs. 3.19a–c). Θ is constantly decreasing, showing a pronounced diurnal cycle, and its anomaly was gradually increasing between −8 d to −2 d to ~+4 K (Fig. 3.19c). The ascent in group SE was, however, slightly less steep and final temperature remained just above 0°C. The only major difference is that Θ was constantly by 2–3 K above that of region NW trajectories. This is likely owing to the
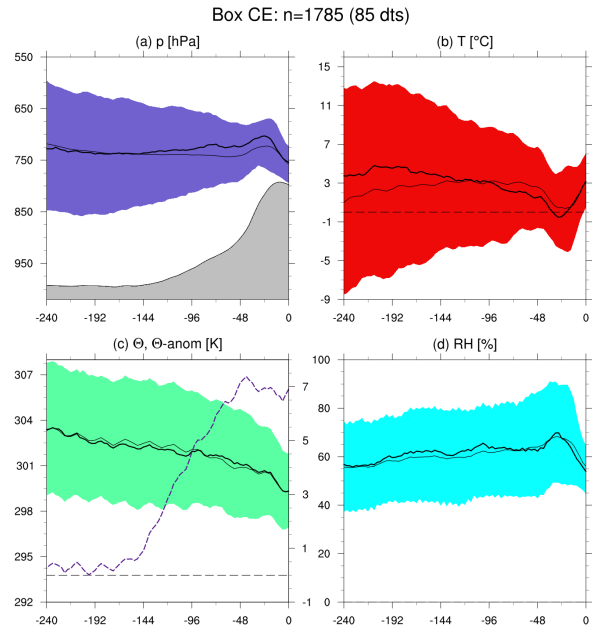

Figure 3.19: The same as in Fig. 3.14, but here for box SE (see Fig. 3.13). To facilitate comparison, axis limits are the same.

poleward slope of the isentropic surfaces, as the regions are by about 10° latitude apart but the air mass altitude is so similar.

The similarities to SW warm events are also obvious, during which the final ascent was even sharper. We do find, however, to a lesser extent the signal of condensational warming in the last 24 h, when median Θ stayed constant and RH was around 80%. SE warm events are most frequent, namely during 24% of all warm events.

Summary

The analyses of the chosen boxes suggests some similarities and discrepancies between two distinct overarching regions. The West and South GrIS share the pattern of air masses that were transported rather far from the surface until they impinged on the steep GrIS. Arriving with probably strong meridional velocity to the ice sheet, the air masses ended up with a Θ-anomaly of $+4\,\mathrm{K}$ to $+5\,\mathrm{K}$. Reduced radiative cooling under cloudy conditions and especially diabatic warming by condensation had contributed to the warmth of the air masses. These processes were most pronounced in the Southwest, where the ascent onto the GrIS mostly occurred within only 12 hours and relative humidity increased to 95%.

The second characteristic region is the eastern to northeastern GrIS. There, air masses that caused warm periods first had to ascend onto the ice sheet, during which they gained some latent heat by condensation or simply did not experience any radiative cooling due to high cloud cover. During the 24 hours prior to the warm event, they descended down the eastern ice sheet and got much drier. Prior to warm event periods in the CE GrIS, the ascent was less strong as air masses that crossed the Summit region directly are less frequent in general, or less likely to lead to a warm event. Most of the "warm" trajectories went around the northern GrIS by anticyclonic transport or travelled along the eastern flank of the GrIS.

We further deduce that the climatological gradients translate to warm events in the different regions. The air mass evolution prior to warm events is similar in the moist-warm South and for weather accessible West GrIS, respectively. In all these regions, arriving air masses were anomalously warm and close to saturation, i.e., they were anomalously humid. The colder and drier Northeast forms a distinct region in the lee of the GrIS. Air parcels there were partly also anomalously moist, but experienced descent and evaporation shortly before arrival.

3.5.3   Synoptic Feature Anomalies

In the following section, we will analyze the large-scale weather pattern during substantial melt in the six regions of interest. The synoptic situation is assessed by (feature) anomaly composites of all time steps associated with a warm event in one region and

the trajectory location prior to arrival. The latter gives an idea about origin but also horizontal and vertical advection of the air masses. Feature anomaly composites will be shown for blocking frequency, cyclone frequency and jet frequency, according to the feature identification after Sprenger et al. (2017), described in Sec. 2.5. In addition, we analyze the $Z500$ anomaly based on ERA-Interim data. All anomalies are shown with respect to the climatology of 1979–2017. We note that it would help to additionally look at the synoptic situation prior to the air mass arrival. For the evolution prior to the event, however, we rely on the previously described trajectory analysis to focus this section on the setting during the events themselves.

Southwest GrIS

Warm events in the Southwest are very frequent: There were 23 years in 1979–2017 during which SW warm events were observed. Due to the southernmost location around 63°N in the storm track region, there is more than one synoptic pattern that can cause surface melt.

$Z500$ (Fig. 3.20e) together with the blocking frequency (Fig. 3.20c) are higher during SW warm events, by up to >150 m and >30%, respectively. The $Z500$ anomaly shows an upper-level ridge over the Denmark Strait to the East of box SW. There is almost always a blocking present over the ocean south of Iceland, whereas the jet frequency is reduced to almost zero in that region of the storm track (Fig. 3.20f). Accordingly, the cyclone frequency is reduced to ∼0 (Fig. 3.20d). We thus see, that some upper-level (∼400–600 hPa) air masses coming from the Canadian Arctic subside within that blocking and the horizontal air mass transport during the four days prior to the event is mainly meridional (Figs. 3.20a,b).

As the majority of air parcels, however, are located at lower levels of the atmosphere (Figs. 3.20a,b), adiabtic descent can not be the only process of warming. Despite the presence of a blocking in the proximity of the GrIS, this blocking does not cover the GBI region of 60–80°N, 20–80°W (Hanna et al., 2016), i.e., the nearest surrounding of the GrIS, in about one third of the composite periods (not shown). In these and also other cases, more frequent cyclones over Newfoundland and the Baffin Bay (Fig. 3.20d) are mostly responsible for northward advection towards Greenland. This includes the about 10–20% of the composite period, when the blocking deviates the jet to the North

and the jet stretches over the Central GrIS (Fig. 3.20f). The presence of a jet over Greenland during warm events is unique to SW warm events. The zonally oriented
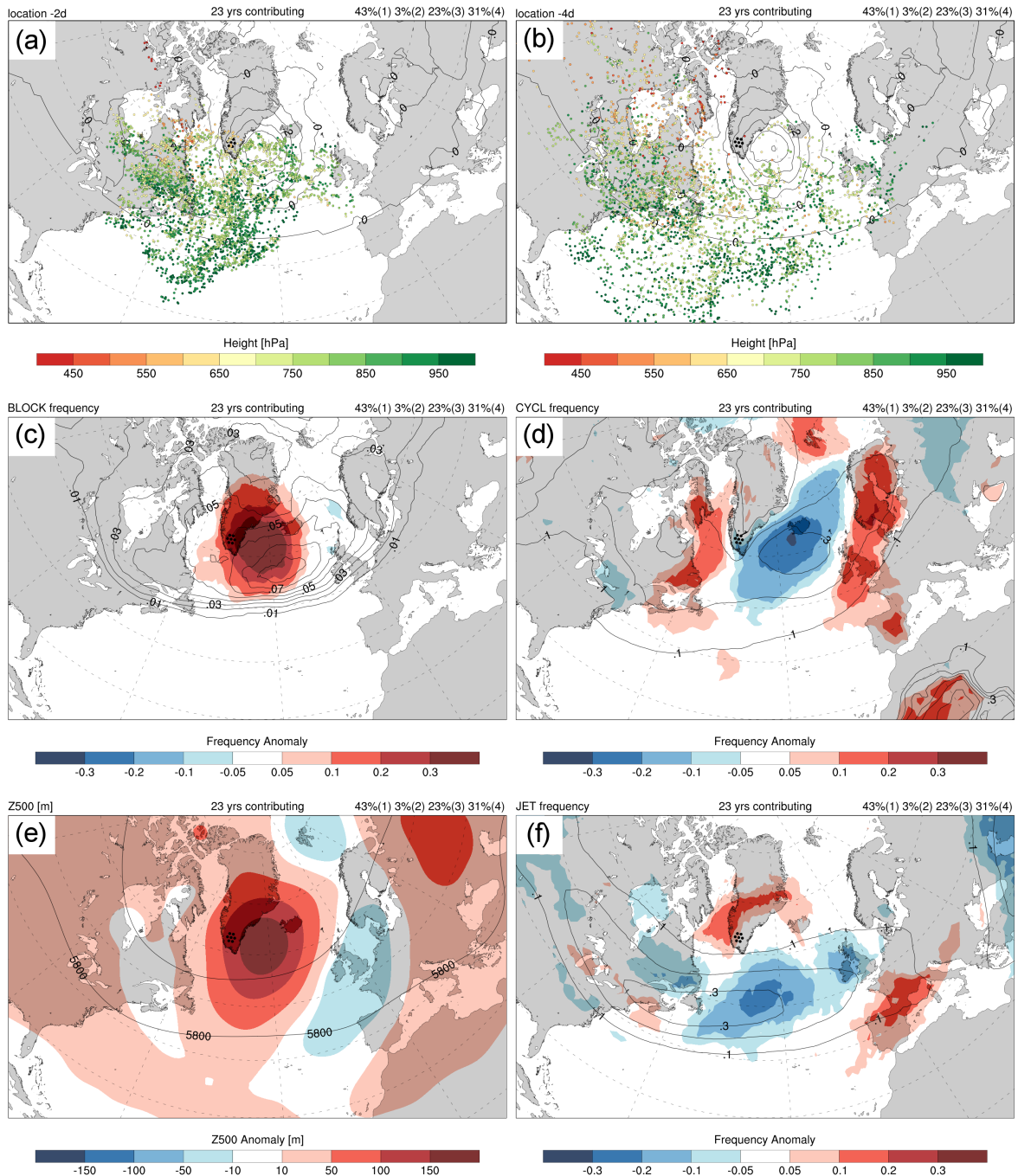
Figure 3.20: Trajectory location (a) 2 d and (b) 4 d prior to arrival, and anomaly composites (SW warm event periods) of (c) blocking frequency, (d) cyclone frequency, (e) $Z500$ and (f) jet frequency in color fill (c–f). Colors of circles in (a),(b) represent pressure. Contour lines in (a),(b) show the blocking frequency anomaly from subplot (c), and in (c–f) the 1979–2017 climatology of the respective features, respectively. In the top string, the number of unique years of time steps contributing to the composite and average category frequency (Sec. 2.3.3) of the trajectories are stated. Note the non-linear color interval of the frequency anomalies.

pressure gradient east of Newfoundland allowed for northward transport of subtropical and mid-latitude air masses by 20–40° latitude within four days (Fig. 3.20b).

The different contributions of transport described above, are also reflected in the distribution among the trajectory categories according to $\Delta\Theta$ and ΔT (Sec. 2.3.3). Almost no relevant southward advection took place (C2: 3%), which is the case for Greenland warm events in general. The dominant categories C1 (43%) and C4 (31%) summarize on low levels northward advected air masses. Some of them were forced by the GrIS topography to ascend, inducing some diabatic warming (C1), while others reached box SW on a more horizontal pathway (C4). The horizontal transport of C1 and C4 trajectories, however, was very similar. The diabatically cooled but overall warmed air masses belong to C3 and represent descending trajectories. They accounted for the remaining 23% of trajectories of the box SW composite.

Central West GrIS

CW warm events are even more common than in the Southwest, occurring in 29 yrs out of the 39-yr spanning study period. Signals of increased cyclone frequency or a northward deviated jet are negligible in the surroundings of box CW (Figs. 3.21d,f). The blocking anomaly is centered over the GrIS and the box CW lies at its northeastern edge (Fig. 3.21c). At -2 d, many trajectories are in close horizontal proximity, but with vertical distance of about 150 hPa to the box (Fig. 3.21a). These trajectories experience subsidence and are more frequent than for SW warm events (C3: 30%).

Even though air masses are generally located closer to the GrIS at -4 d, a substantial part resides up to 45° south of box CW. Thus, the largest contributions of trajectories are related to northward transport (C4: 41%) combined with upward vertical motion (C1: 26%). That C1 trajectories are by almost 20% less frequent in the Central- compared to the Southwest, is at least partially owing to the GrIS topography faced along the air mass trajectories. With a strong southerly wind component, box CW can only be reached via South Dome, or at least via somewhat elevated parts of the southern GrIS. Therefore, air masses are more likely to reach box CW from higher altitudes or with a weaker and less steep ascent over 10 days. On the other hand, air masses ending up over the southwestern GrIS hit the slope more or less directly when coming from the North Atlantic.

CW warm events, however, are not fully dependent on a Greenland-centered blocking. Again, about a third of the composite period does not contain any blocking in the GBI region. A typical cyclone path is the northward movement and accompanying decay of cyclones coming from Newfoundland. The consequently elevated climatological cyclone frequency west of box CW causes a southerly flow every fifth day on average.
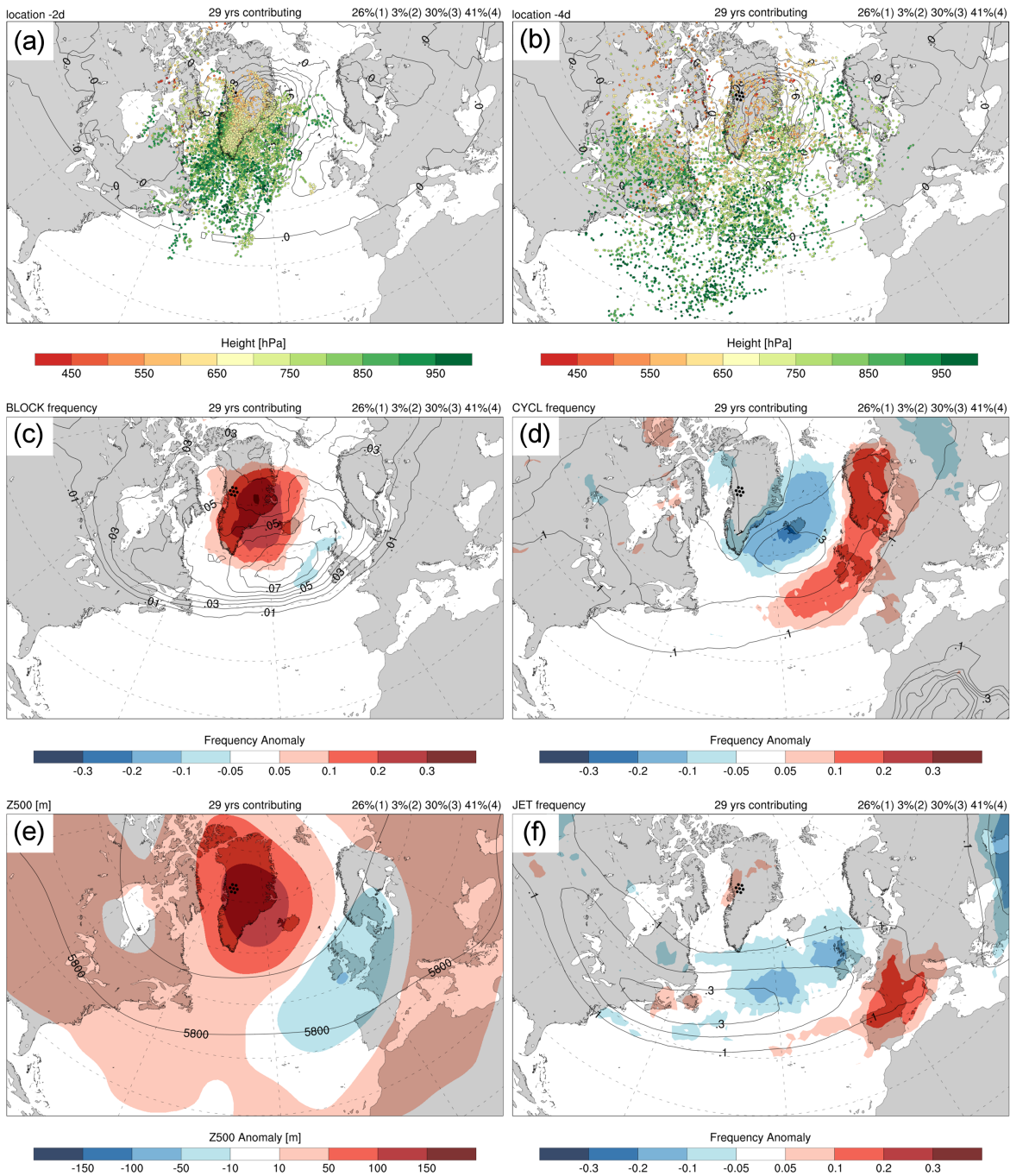
Figure 3.21: Trajectory location and anomaly composites of CW warm event periods analogous to Fig. 3.20.

To summarize, the CW GrIS is still far enough south, to be affected by the storm track region and accessible to southwesterly winds. Additionally, the location with respect to favourable blocking situations seems more prone to subsidence-induced warming, than it was the case for the Southwest GrIS.

Northwest GrIS

Northwest Greenland experiences significant melt when air masses reach the region from over the Baffin Bay. Air mass transport in the days prior to warm event periods is channelled in the narrow path between the GrIS and the Canadian Arctic (Fig. 3.22a). Trajectories reach the Baffin Bay mostly from southerly, and in a few cases from southwesterly regions (Fig. 3.22b). Some of the following synoptic features help to explain that path.

The $Z500$ (Fig. 3.22f) and blocking frequency (Fig. 3.22c) anomaly of the box NW composite are strongest among all six regions of interest. Large parts of the Central GrIS showed a $>+150$ m and $>+30\%$ anomaly of $Z500$ and blocking frequency, respectively. The Central GrIS is also a region of climatologically low $Z500$ and blocking frequency, respectively. The absolute strength of the upper-level ridge is consequently similar to that during other warm events, but clearly stands out in the far Northwest of the GrIS. The relative contribution to warming by adiabatic descent, however, is about as low as for SW warm events (C3: 24%). The largest contributions of trajectories come from C4 and C1, namely 44% and 30%, respectively, which are related to transport. Cyclones over Newfoundland and Nunavut occur 10–20% more often during NW warm events than on 1979–2017 average. In the Nunavut region, this goes along with upper-level troughs, i.e., on average 10–50 m lower $Z500$. The northward flow over the Baffin Bay is further fostered by reduced cyclone frequency right there.

All in all, the mechanisms of warming of NW warm events is similar to that in the SW, with more mainly northward moving trajectories at the expense of additionally ascending trajectories. The synoptic situation is highly comparable as well, with a northward shifted blocking anomaly. A substantial difference is, however, that warm events in box NW are, to a much larger extent reliant on a blocking in the GBI region. A Greenland blocking is present in more than 85% of NW warm events (not shown).

North- to Central East GrIS

The upper-level pattern of warm events relevant to boxes NE and CE consists of an East Greenland-centered ridge ($Z500$ anomaly of $+50$ to $+150\,\mathrm{m}$) and a trough over Northern Europe ($Z500$ anomaly of -10 to $-100\,\mathrm{m}$) (Figs. 3.23e and 3.24e). Also, blocks are $>30\%$ more frequent in that region (Figs. 3.23c and 3.24c) and the Icelandic
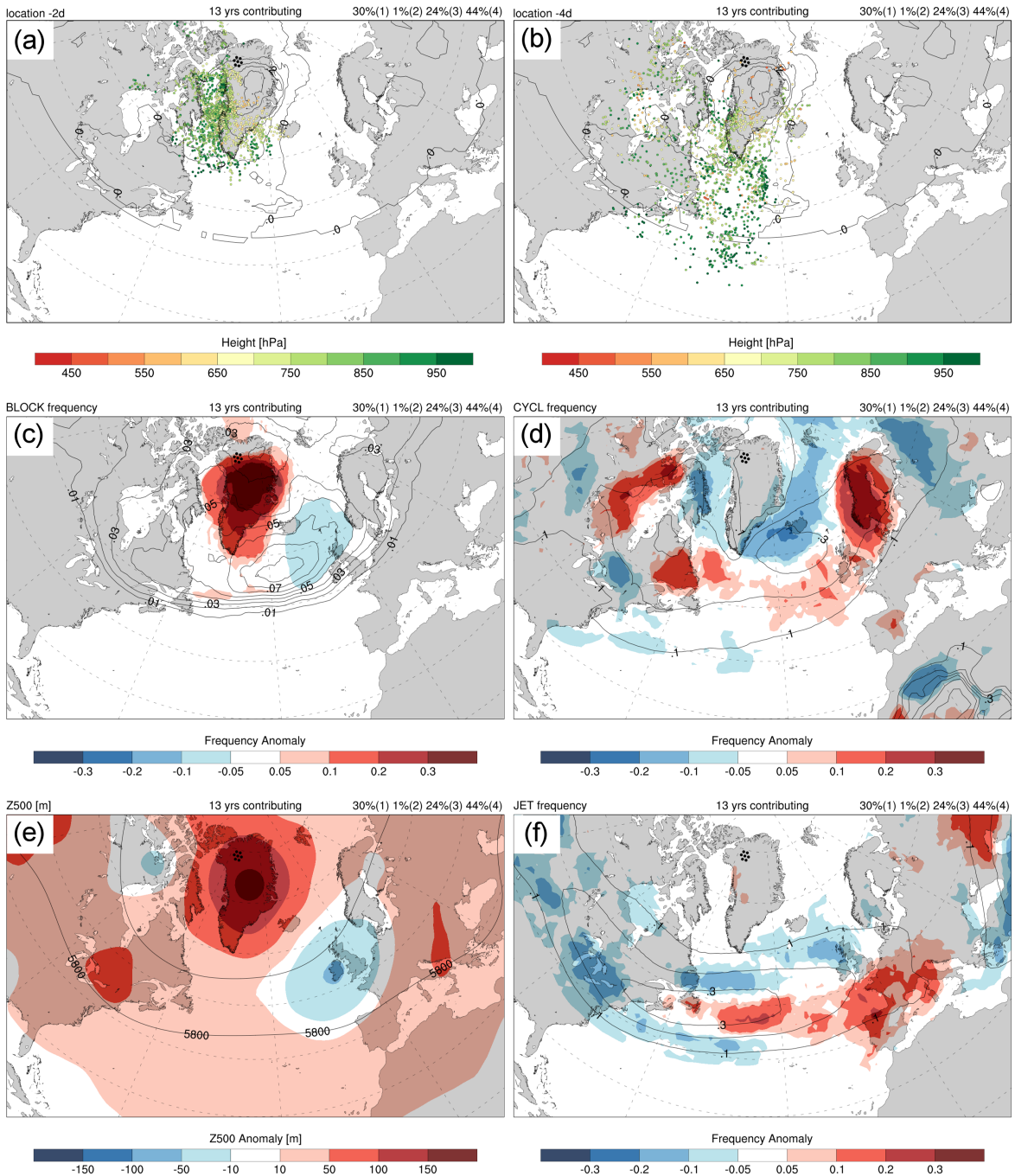
Figure 3.22: Trajectory location and anomaly composites of NW warm event periods analogous to Fig. 3.20.

Low is absent or shifted southwards (Figs. 3.23d and 3.24d).

For both regions, a cyclone near Nunavut is apparently favourable (Figs. 3.23d and 3.24d) as it advects mid-latitude air masses to the northwestern GrIS. With a Greenland blocking present in the GBI region during ∼85% of the warm event periods, that
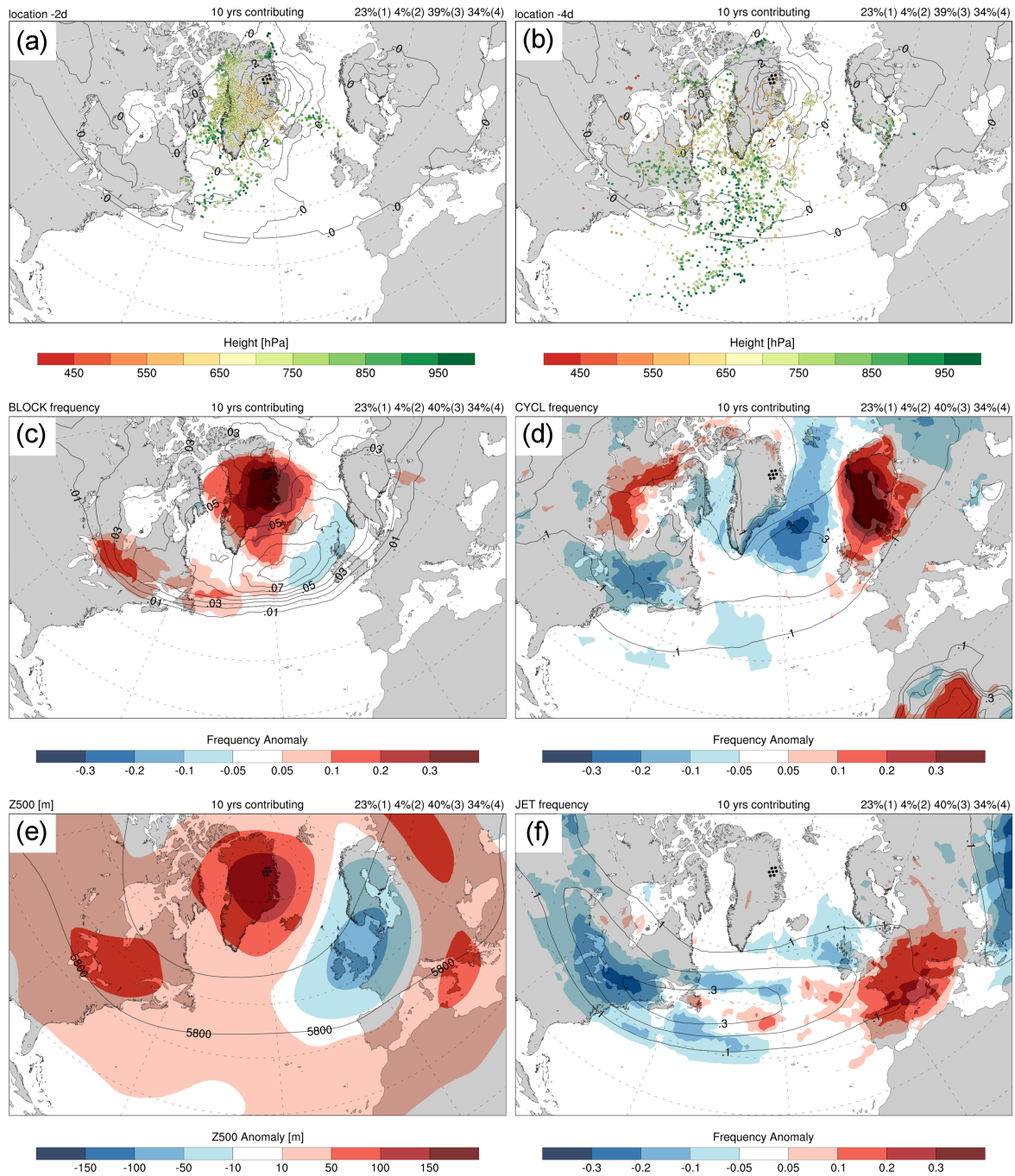
Figure 3.23: Trajectory location and anomaly composites of NE warm event periods analogous to Fig. 3.20.

air is then brought over the ice sheet ridge to its eastern side. A Greenland blocking is highly relevant for those two regions, as for box NW. Note, that these three regions were also affected equally often by a warm event, namely in 10–13 yrs of the study period. Apart from advection, the warming by subsidence is key to CE warm events, where most trajectories fall into C3 (54%). Already four days prior to a warm event,
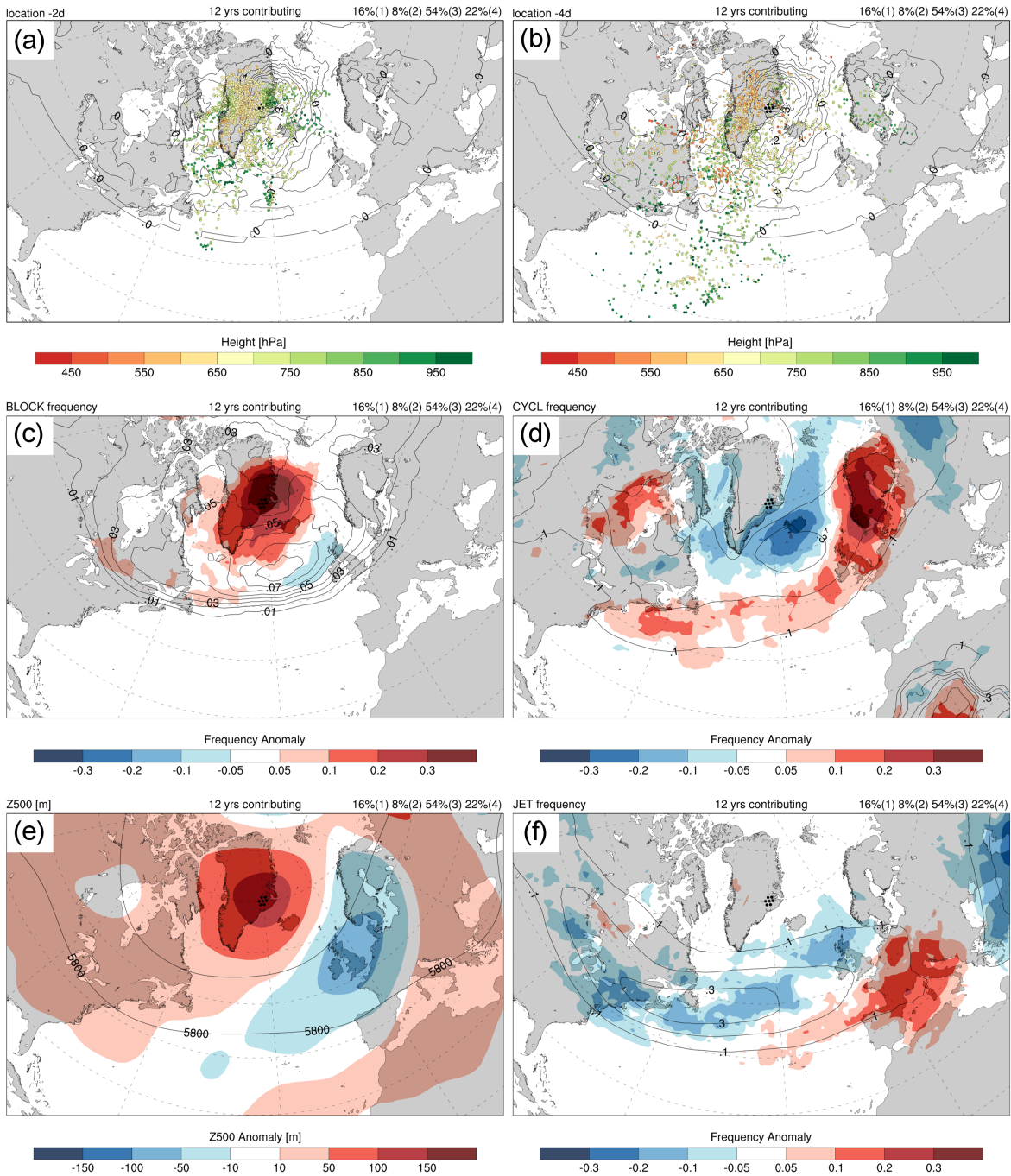
Figure 3.24: Trajectory location and anomaly composites of CE warm event periods analogous to Fig. 3.20.

many trajectories are in the nearest proximity of box CE (Fig. 3.24b). But also for the NE, C3 is the most numerous trajectory category with 39%. At -2 d, the two main trajectory groups also split into two residence regions. One group, we assume mainly C1/C4 trajectories, is located at intermediate levels above the Greenland west coast, while mostly C3 trajectories reside at upper levels over the central to eastern GrIS (Fig. 3.23a).

While air masses are transported mainly over the GrIS (from west of the ice divide) before arriving in box NE, the trajectory to box CE is sometimes more direct from the Denmark Strait. In 20–40% of the CE composite period, a cyclone is located in the North Atlantic storm track. When located just south of Iceland, a cyclone opens the direct gateway for mid-latitude or even subtropical air masses to the eastern GrIS.

Box NE and CE share the same blocking-dominated synoptic pattern, but the box location is in different spatial relation to the blocking center. The block center typically lies south of box NE, but north of box CE, respectively. As a consequence, C1 and/or C4 trajectories likely represent different pathways for box NE and CE. Further, mostly lying in the center of the blocking system, box CE experiences warm events that are more strongly related to subsidence compared to box NE. Nonetheless, warming from adiabatic descent is relevant to the (north-)eastern GrIS as a whole.

Southeast GrIS

The general synoptic weather pattern for warm events significant to SE Greenland deviates the least from the climatology (Figs. 3.25c-f). This is due to a combination of different atmospheric constellations causing the arrival of warm air masses in that location, which dilutes the composite signals.

The cyclone frequency over Iceland is reduced the least, in the sense that its anomaly does not extend as far south as during SW...CE warm events (Fig. 3.25d). This is because the Icelandic Low can, if located south of Iceland, also foster warm events in Southeast GrIS by southerly winds. Along with that, the jet frequency is reduced along the northern edge of the storm track (Fig. 3.25f). Further, there is a sign of more cyclones over Newfoundland during 5–10% of SE warm event periods, which was already the case for boxes SW and NW. The transport pattern transfers to the trajec-

tory categorization, with C4 as the most frequent one (39%). C1 accounts for 30% of the air masses.

The presence of the Icelandic Low comes at the cost of a blocking over Southeast Greenland and the Denmark Strait (Fig. 3.25c). As for box SW and CW, there is
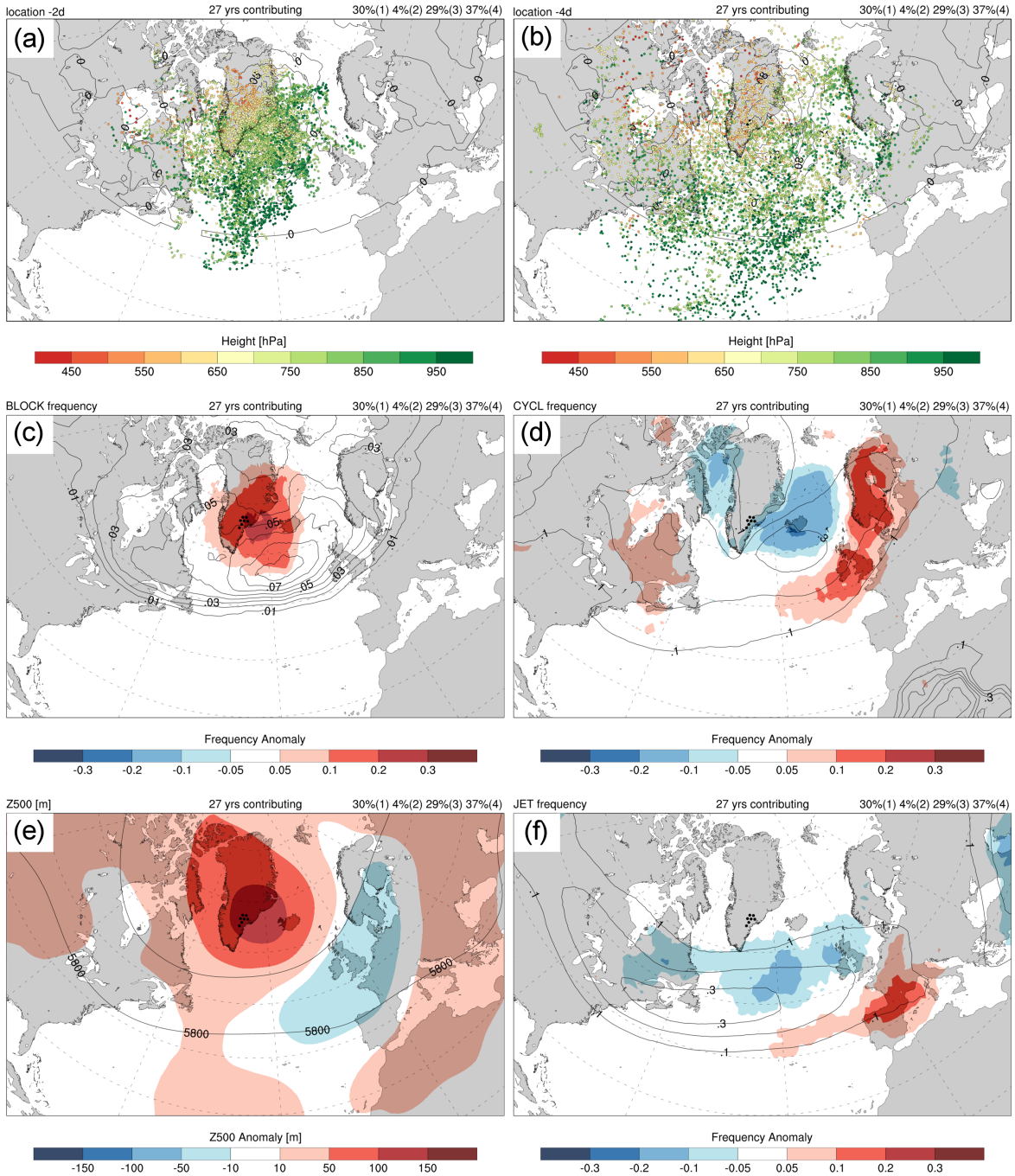
Figure 3.25: Trajectory location and anomaly composites of SE warm event periods analogous to Fig. 3.20.

no blocked situation in the GBI region at all during a third of the box SE composite periods (not shown). Nevertheless, blocking-induced subsidence plays a role in box SE as well, with 29% of the trajectories falling into C3. The vertically further and horizontally closer trajectory group, is shown in Figs. 3.25a,b. Otherwise, trajectories mostly approach the SE GrIS from east of the ice divide. Only a few air masses cross South Dome region and descend to box SE. Even though some air masses were located as far south as ∼20°N at −4 d (Fig. 3.25b), most of them are located roughly 10° latitude further north than the southernmost ones of box SW.

Summary

The dominant synoptic features among all the six regions of interest are a pronounced $Z500$ ridge and atmospheric blocking, centered over the regions (box CE, NE) or located to their Southeast (box SW, CW, NW, SE). A blocking is defined as a negative anomaly (of at least $-1.3\,\mathrm{PVU}$) of vertically averaged PV (150–500 hPa) that persists over at least five days (Sprenger et al., 2017). Blocks are especially important for warm events in the northern and eastern GrIS, where warm events were observed during 10–13 yrs in 1979–2017. They are present in the GBI region during about 85% of the warm event periods. In addition to the associated high pressure system, cyclones over the Canadian Arctic or the North Atlantic south of Greenland favour the northward advection of air masses from lower latitudes. During SW, CW and SE warm events, the blocking occurrence in the GBI region is reduced to ∼70%. Warm events are also observed during periods of cyclone passages in the storm track region, partly concentrated over Newfoundland. In the SW and NW, subsidence induced warming (C3 trajectories) is weakest, as air parcels originate from the lowest atmospheric levels among all regions (Sec. 3.5.2). Still, warm events are generally more frequent in South and West Greenland with warm event-related surface melt in 23–29 yrs during 1979–2017.

In all regions, the main air mass trajectory during warm events is meridional, except for C3 trajectories which show little horizontal movement and primarily descend (Appendix Figs. 1–4). The northward advection occurs faster along the western than along the eastern GrIS. In the northerly regions, transport occurs often anticyclonically prior to the air mass arrival. For box NW, trajectories are almost entirely restricted to come from over the Baffin Bay. The jet associated with the North Atlantic storm

track, is typically shifted southwards or completely weakened during warm events – a typical NAO− pattern. Only during 10–20% of warm events in the SW GrIS, a strong jet is present over Central Greenland.

Another important process causing surface melt during atmospheric blocking, apart from warm air advection, is enhanced incoming solar radiation. It has not been mentioned so far as it is obscured by the Lagrangian perspective. Evaporation in descending air masses causes clear-sky conditions within large areas of the high pressure system. We will address the surface energy balance in the discussion chapter (Chap. 4), as a longer discourse is needed on the different contributions from incoming shortwave and longwave radiation – not only in clear-sky, but also under cloudy conditions. But the results presented above – high blocking frequency but minor importance of C3 trajectories – indicate, that radiation could be a substantial contributor to surface melt during warm events.

3.5.4 Transport Characteristics and Their Climatology

The results from Secs. 3.5.2 and 3.5.3, as well as the case study from July 2012 (Sec. 3.4) highlighted that strong advection of moist-warm air masses occurred during almost all warm events. A prominent pathway is from southerly source regions over the North Atlantic to the GrIS. As for EV69, however, other source regions of warm air masses are upper, potentially anomalously warm levels of the atmosphere – independent on their latitude. The mostly present blocking over Greenland then induces subsidence and adiabatic warming. We will address both meridional and vertical transport in this section by comparing the minimum latitude and minimum pressure of warm event trajectories, using the 1979–2017 trajectory climatology. Results from EV69 further demonstrated that some warm event trajectories originate from anomalously warm high-latitude regions, such as the Northern Canadian Arctic. Also, besides warm origin and adiabatic heating, diabatic processes are a second warming source acting on the trajectories before arriving over the GrIS. This is why we conclude the result section with a qualitative assessment of three potential warming sources: anomalously warm air mass origin, diabatic heating and transport between climatologically distinctive regions.
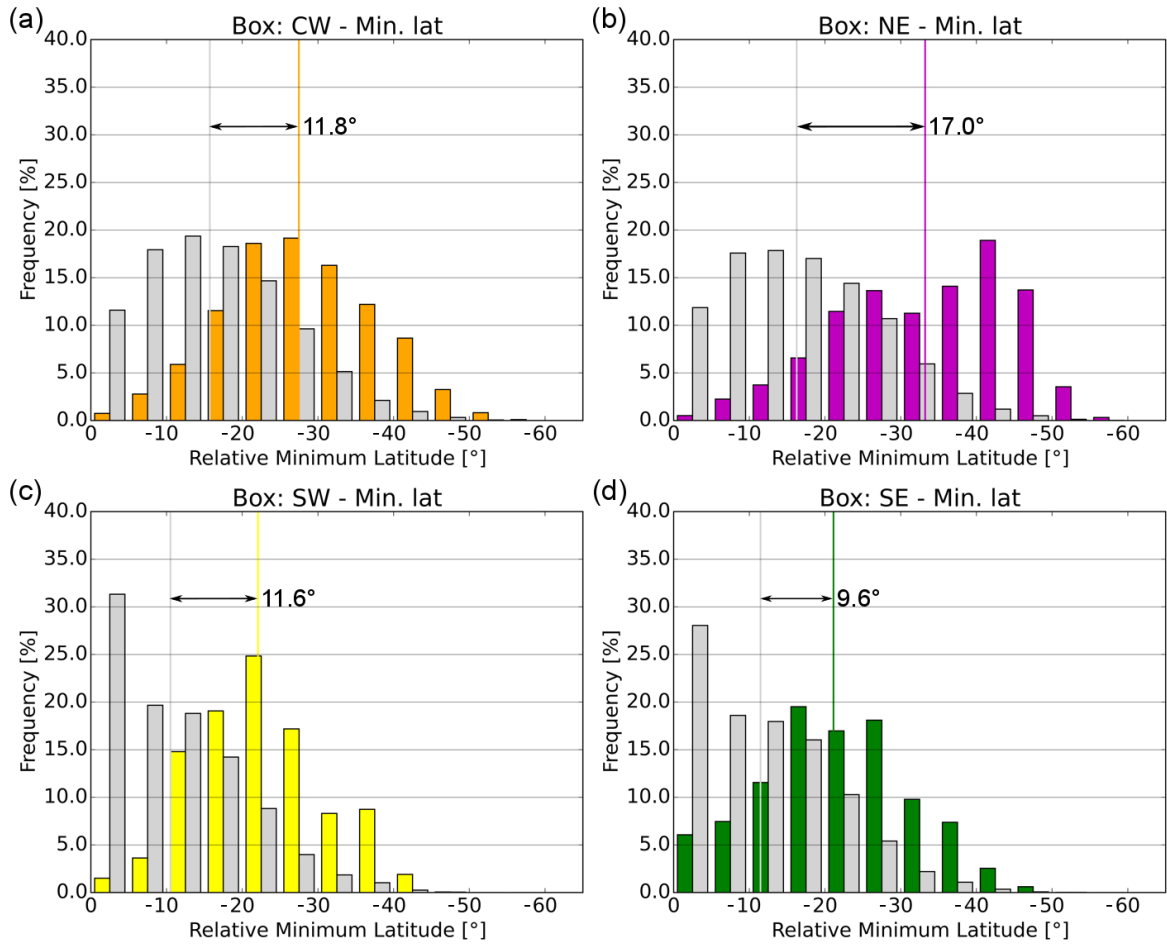
Figure 3.26: Normalized histograms of minimum latitude relative to latitude of arrival. Yellow, orange, purple and green bars show histograms of SW, CW, NE and SE warm event trajectories, respectively. For comparison, grey bars denote the occurrence frequencies of all JJA 1979–2017 trajectories reaching the respective region. Vertical lines show the histogram averages and their difference is stated next to the arrow in between.

Horizontal Transport: Relative Minimum Latitude

In all regions of the GrIS, we see a clear signal that the relative minimum latitude is further south during warm events compared to climatology (Fig. 3.26). During warm events, there are almost no trajectories that come from the North and thus show a relative minimum latitude of 0°, except for about 6% of the trajectories arriving in box SE (Fig. 3.26d). Averaged over all six regions, the relative minimum latitude is anomalous by $-12.9°$ for warm events compared to climatology.

The influence of the upper bound of the distribution at 0° is obvious in the 1979–2017 climatology. During the warm event periods, however, the relative minimum latitude is close to normally distributed for regions SW, CW and SE (Figs. 3.26a,c,d).

63

In the northern and eastern GrIS (boxes NW, NE, CE), there seem to be two groups of trajectories, exemplary shown by a secondary peak for NE trajectories at around $-40°$ relative minimum latitude (Fig. 3.26b; Appendix Fig. 5). Trajectories crossing more than $40°$ latitude prior to the event are most relevant to box NE ($\geq 35\%$). In boxes NW and CE, these trajectories make up around 30% and 15%, respectively. This highlights, compared to the analysis before, a closer similarity between the two north-ernmost boxes rather than between boxes NE and CE. Over the whole study period as well as during warm events only, the relative minimum latitude distribution of box CE is more similar to that of box SE.

Combining the relative minimum latitude with the location of the chosen boxes, we find that air masses of Greenland warm events largely come from the 30–50°N latitude band. Also, there are, except for SE warm events, less than 2% of air masses coming from further north.

Vertical Transport: Relative Minimum Pressure

More southerly origins indicate that originally warmer air masses are responsible for the warm event. Potentially warm air masses can, however, originate from higher up in the atmosphere as well. Fig. 3.27 shows the relative minimum pressure and ad-dresses the ascent-descent-ratio. For boxes NE and CE, the average relative minimum pressure is not significantly different from the climatology. This is different for the remaining regions, with an average difference of -20.3 hPa, -29.2 hPa and -31.7 hPa during warm events in boxes CW, NW and SE, respectively, and even of -42.4 hPa for box SW. Over all six regions, the difference averages at -17.2 hPa. We focus on two aspects of the distribution shift during warm events compared to climatology. On the one hand, trajectories that show ascent or weak vertical motion are more frequent. On the other hand, there is a subtle but important shift towards strongly (>300 hPa) descending air masses.

In Sec. 3.5.3, box NE and especially box CE showed the largest contribution from mainly descending trajectories responsible for warm events; C3 accounted for 39% and 54% of all trajectories, respectively. They typically descend shortly prior to arrival (Sec. 3.5.2). It is also those two regions that show the strongest subtle shift to trajec-tories descending >300 hPa (Fig. 3.27b). The lowest minimum relative pressure bin,
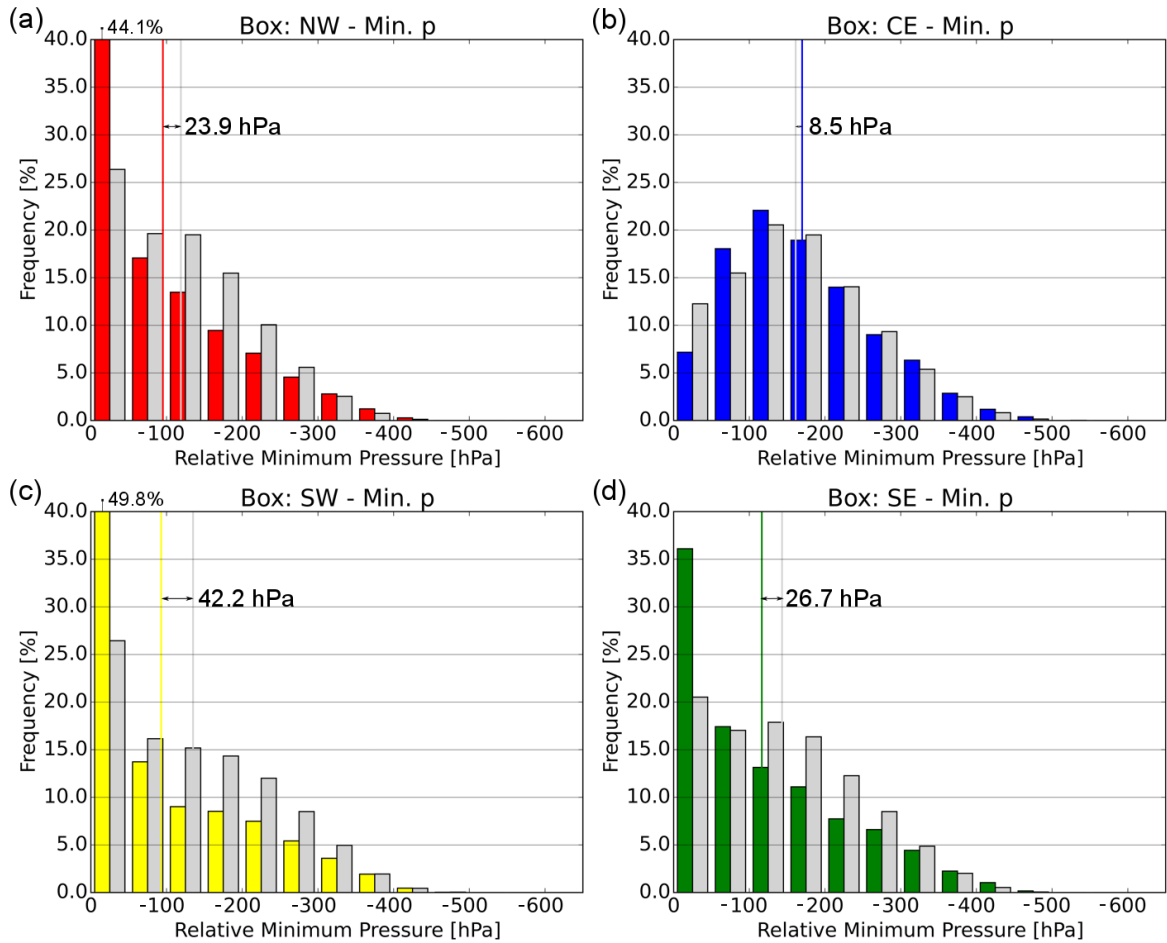
Figure 3.27: Normalized histograms of minimum pressure relative to pressure of arrival. The histograms are analogue to those in Fig. 3.26. Note, that different regions are shown here: Yellow, red, blue and green bars show histograms of SW, NW, CE and SE warm event trajectories, respectively.

i.e., trajectories that ascended or descended by less than 50 hPa, is less frequent than normal.

This bin of weakly descending or even ascending air masses is much more frequent for regions SW and NW (Figs. 3.27a,c). Its frequency was more than 20% above normal and almost doubled for the Southwest GrIS. The majority of increase in bin count comes from ascending trajectories; The percentage of ascending trajectories in box SW increases from 10.7% (climatology) to 29.4% during warm events, and in box NW from 8.4% to 13.7%, respectively (not shown). Remember that these air parcels typically show a sharp ascent when hitting the GrIS within the last 24 h prior to arrival (Sec. 3.5.2), and C1 and C4 together accounted for 74% of all trajectories. Contrarily, the increase in strongly descending air masses is not present (SW) or small (NW).

Finally, boxes SE and CW are sharing the same pattern of relative minimum pressure to a large extent. The typical distribution for the two regions is almost identical between 1979–2017 (Fig. 3.27d). SE warm events are associated with much more trajectories in the lowest bin, $-50\,\text{hPa}$ to $0\,\text{hPa}$ (Fig. 3.27d), which likely represent trajectories in C1 and C4. 15.2% of warm event trajectories in the SE ascend, while only 6.7% do so in the climatology (not shown). So do warm event trajectories arriving in box CW, with a tendency towards some more strongly descending air masses (Appendix Fig. 6) and only a slight increase in ascending trajectories compared to climatology (not shown).

Transport vs. Diabatic Processes

We have yet not quantified to which extent originally warm air masses, which possibly also experienced adiabatic warming, or diabatic processes in the $10\,\text{d}$ of transport are responsible for air mass warmth in Greenland warm events.

$$\Theta_{anom}(0) = \Theta_{anom}(-10) + Tr + Di$$
$$Tr = \Theta_{clim}(-10) - \Theta_{clim}(0) \tag{3.1}$$
$$Di = \Theta(0) - \Theta(-10)$$

$\Theta(t)$	potential temperature [K]
$\Theta_{anom}(t)$	potential temperature anomaly [K]
$\Theta_{clim}(t)$	climatological potential temperature [K]
t	time along backward trajectory [d]
Tr	transport-induced Θ_{anom} [K]
Di	diabatically induced Θ_{anom} [K]

The method described with Eqs. 3.1 splits the potential temperature anomaly at the time of arrival, $\Theta_{anom}(t = 0)$, into three components: (i) The initial potential temperature anomaly, $\Theta_{anom}(t = -10)$, (ii) transport from a warmer climate to that of the GrIS, Tr, and (iii) diabatic warming, Di. Di describes the sum of all diabatic processes acting on an air mass. With Tr, we assess warming due to the distinctive climate in the source region and Greenland. For positive Tr, the source region is warmer than during normal transport towards the GrIS. So in adiabatic flows ($D\Theta/Dt = 0$), $\Theta_{anom}(t = 0)$ is the result of $\Theta_{anom}(t = -10)$ and Tr. In addition we introduce a parameter $R_{Di/Tr}$, to estimate the relative contribution of diabatic processes excluding longwave cooling, which every air mass typically experiences and thus is of minor interest, and transport.

Based on experiments by Cavallo and Hakim (2013) and observations of trajectories in the remote Arctic (Papritz and Spengler, 2017), we approximate the pure long-wave cooling rate with $-1\,\mathrm{K/d}$. The parameter $R_{Di/Tr} = (Di - (-10\ K))/(Tr)$ then represents the ratio of net diabatic warming and transport along the $10\,\mathrm{d}$ backward trajectories.

Calculating medians for all warm event time steps relevant to the six regions, we find the different contributions as listed in Tab. 3.4. In addition, we state the same values for EV69 ("warm") trajectories, which are discussed at the very end of this section. We note here that the spread within one trajectory group is on the same order of magnitude as the values themselves (Appendix Tab. 4).

Ten days prior to the warm event, all trajectories reaching the different GrIS regions did not show any significant warm anomaly. In the following, the anomaly grew to $+4\,\mathrm{K}$ to $+5\,\mathrm{K}$ when arriving over the southern and western GrIS, respectively, and to around $+7\,\mathrm{K}$ when arriving in regions NE and CE. That the anomaly in the North- and Central East is stronger has two reasons: prevailing climate is colder and arriving trajectories are the warmest among all groups in terms of temperature and potential temperature (Sec. 3.5.2). During transport to the GrIS, the NE and CE trajectory

Table 3.4: The table shows median values for trajectories arriving in box SW, CW, NW, NE, CE, SE during warm events and during EV69, respectively. Values for EV69 are shown for all GrIS trajectories (EV69$_{all}$) and only those causing melt (EV69$_{warm}$). The air mass Θ-anomaly at arrival $\Theta_{anom}(t=0)$ equals the sum of (i) initial Θ-anomaly $\Theta_{anom}(t=-10)$, (ii) transport-induced warm anomaly and (iii) diabatic cooling. The ratio of net diabatic warming excl. radiative cooling and transport $R_{Di/Tr}$ is calculated from the median values.

	$\Theta_{\mathbf{anom}}(0)$	$\Theta_{\mathbf{anom}}(\text{-10})$	**Transport**	**Diabatics**	$\mathbf{R_{Di/Tr}}$
Box SW	$+4.7\,\mathrm{K}$	$+0.2\,\mathrm{K}$	$+6.6\,\mathrm{K}$	$-2.6\,\mathrm{K}$	1.13
Box CW	$+4.9\,\mathrm{K}$	$+0.3\,\mathrm{K}$	$+8.3\,\mathrm{K}$	$-4.0\,\mathrm{K}$	0.72
Box NW	$+4.2\,\mathrm{K}$	$+0.0\,\mathrm{K}$	$+7.6\,\mathrm{K}$	$-3.7\,\mathrm{K}$	0.83
Box NE	$+6.8\,\mathrm{K}$	$-0.0\,\mathrm{K}$	$+10.3\,\mathrm{K}$	$-4.4\,\mathrm{K}$	0.54
Box CE	$+6.9\,\mathrm{K}$	$+0.3\,\mathrm{K}$	$+10.6\,\mathrm{K}$	$-4.5\,\mathrm{K}$	0.52
Box SE	$+4.2\,\mathrm{K}$	$+0.3\,\mathrm{K}$	$+7.3\,\mathrm{K}$	$-4.1\,\mathrm{K}$	0.82
EV69$_{\mathbf{warm}}$	$+4.1\,\mathrm{K}$	$+1.0\,\mathrm{K}$	$+8.4\,\mathrm{K}$	$-5.6\,\mathrm{K}$	0.53
EV69$_{\mathbf{all}}$	$+2.8\,\mathrm{K}$	$+1.2\,\mathrm{K}$	$+6.4\,\mathrm{K}$	$-5.1\,\mathrm{K}$	0.76

groups also experienced most net diabatic cooling of $-4.4\,$K and $-4.5\,$K, respectively. Reasons for that are stronger longwave cooling, as they showed a larger Θ-anomaly, but also the evaporative cooling or the absence of latent heating that was observed only along these trajectories (Sec. 3.5.2). But transport from a $10.3\,$K and $10.6\,$K warmer climate, respectively, overcompensated for that cooling by far.

Also for the other trajectory groups, a stronger transport-induced warm anomaly typically goes along with stronger diabatic cooling – most likely explained by the larger Θ-gradient to their surroundings. Air masses related to warm events in the SW show weakest diabatic cooling of $-2.6\,$K over ten days. There, the strong final ascent induced latent heating for almost the entire trajectory set with a final median relative humidity of 95% (Sec. 3.5.2). Relative humidity increased to similar levels along NW trajectories, where net diabatic cooling is still rather weak with $-3.7\,$K. For regions CW and SE, where relative humidity increased only along about half of the trajectory groups to above 80% while other trajectories remained above cloud level, diabatic heating is reduced and hence less important to warm event trajectories.

When neglecting typical radiative cooling at a rate of $-1\,$K/d, diabatic processes are more important than transport for warming the SW GrIS, as $R_{Di/Tr} = 1.13$. For the NW and SE, transport already takes priority over net warming diabatic effects, but $R_{Di/Tr}$ is still comparably high with 0.83 and 0.82, respectively. We suggest that the main warming diabatic process acting on any warm event trajectory is latent heating by condensation, when the trajectory ascends on the GrIS. This is also confirmed by the lower $R_{Di/Tr} = 0.72$ in box CW, where air masses ascend less steeply and become less saturated than for example in the SW (Sec. 3.5.2). Of course, latent heating is mostly happening due to advection towards the steep GrIS, but it is still a warming mechanism separate from transport itself. Again, the central- and northeastern GrIS shows a distinct pattern. Warm events there are highly dependent on transport, which is about twice as important as diabatic warming mechanisms, i.e., $R_{Di/Tr}$ equals 0.54 in box NE and 0.52 in box CE. The air masses causing warm events are initially loaded with warmth, due to their origin in climatologically warmer regions, which is then transported to the (north-)eastern GrIS, and partly released due to adiabtic descent (Sec. 3.5.3).

We close the result section with a note on the most extreme warm event EV69, where surface melt reached up to Summit box at five time steps. The GrIS was 2.8 K warmer than the climatology in EV69. The warm anomaly was higher (+4.1 K) when only accounting for regions that experienced surface melt. A high transport-induced temperature anomaly, rather strong diabatic cooling and a very low $R_{Di/Tr}$ highlight the similarities to box NE and CE warm events, and thus a peculiarity of EV69; it included the North and East of the GrIS, which are usually not affected by melt. In contrast to the regional analysis from above, we find that EV69 trajectories that cause melt were initially already 1.0 K warmer than normal – a confirmation of the anomalously warm Canadian Arctic, Labrador Sea and the North American continent, respectively, as origin. This could explain why net diabatic cooling during EV69, -5.6 K and -5.1 K, respectively, is higher than for warm events in the six regions of interest. By and large, EV69 is an exemplary warm event dominated by transport patterns. When comparing $EV69_{all}$ with $EV69_{warm}$, we see that Tr is significantly higher and $R_{Di/Tr}$ lower. So transport was especially relevant to regions experiencing surface melt. The difference in Di further explains that melting affected climatologically colder regions.

Chapter 4

Discussion

We focus our discussion on the air mass origin during the most extensive warm event in July 2012 (Sec. 4.1) and the characteristic physical processes of warming (Sec. 4.2). The latter section is about horizontal and vertical transport (Sec. 4.2.1), surface energy budget anomalies related to warm events, which were not yet investigated in this study (Sec. 4.2.2), and the placement of Greenland warm events in the broader context of climate change (Sec. 4.2.3).

4.1   Case Study of Warm Event in July 2012: Air Mass Origin

Warm event EV69, which took place from 18 UTC 2 July to 18 UTC 17 July 2012, is the most extensive warm event in 1979–2017, as it covered 94.8% of the GrIS (based on 1° horizontal data resolution). During the first week of EV69, the jet stream over the North Atlantic was meandering, with a prominent zonal surface pressure gradient between cyclones over Newfoundland and the Azores High. During southerly wind regimes, the near surface potential temperature anomaly around South Dome increased already up to +9 K. An extensive warm anomaly of around +5 K spread over the entire Labrador Sea, Baffin Bay as well as South and West Greenland on 9 July. The southerly flow further brought a lot of moisture to those regions, which, in the following days, got advected towards and over the GrIS (Mattingly et al., 2016), and resulted in several rain events along the western GrIS (Nghiem et al., 2012; Fausto et al., 2016). After the breaking of the Rossby wave, an anticyclone centered over Greenland developed and dominated the synoptic situation over Greenland for the remaining eight days. Except

for coastal areas in the very South, Greenland near surface and upper-level potential temperature were mostly more than two standard deviations above the long-term average. At Summit Station (3216 m), positive $T2M$ were measured and observed in a continuous melt layer (Nghiem et al., 2012). Warm events of similar duration and with maximum melt extent of 56.0% and 70.3%, respectively, preceded and followed EV69. With such exceptional atmospheric forcing, 2012 showed the largest melt extent in the satellite era (Nghiem et al., 2012), set new records in terms of albedo, bare ice exposure and surface and total mass loss (Tedesco et al., 2013; Fettweis et al., 2017).

We confirm, which has been agreed on by the literature (e.g., Nghiem et al., 2012; Fettweis et al., 2013; Tedesco et al., 2013; Hanna et al., 2014; Neff et al., 2014), that an anomalous ridge of warm air reached Greenland and was stationary for several days. This blocking is evident in the lowest station-based JJA NAO index of -2.8 since 1864 (Hurrell and National Center for Atmospheric Research Staff (Eds.), 2018) and highest JJA GBI since 1851 (Hanna et al., 2016). Air masses from the subtropical North Atlantic around $\sim$20°N were advected to the GrIS.

Neff et al. (2014) argued that the North American heat wave (Hoerling et al., 2014) was a key factor during the warm event. Bonne et al. (2015) picked up their perspective and found that dry warm air advection from the North American continent was essential to the Greenland warm event. Indeed, the air masses causing melt during EV69 show an initial Θ-anomaly of $+1.0$ K. We, however, find that air masses originating from the North American continent were only a small fraction of all air masses arriving over the GrIS during EV69. Some trajectories from the Great Plains converge with others from the western subtropical North Atlantic and likely follow the pattern described by Neff et al. (2014) and Bonne et al. (2015). So those trajectories were exceptionally warm and dry, took up a lot of moisture, became part of an atmospheric river and ended up around Summit Station, as argued by Neff et al. (2014). But melt during EV69 spread all over the GrIS, showing a maximum daily extent above 40% and even above 80% in 12 and four out of the 15 days, respectively. So despite the importance of low-level air masses from the US continent, the major source regions of air masses that contributed to the extensive July 2012 warm event were (i) the anomalously warm lower- and upper-levels of the Canadian Arctic, Newfoundland and the Labrador Sea, and (ii) also regions without significant temperature anomalies such as the subtropical

North Atlantic (low-levels) and, to a small extent, the Arctic Ocean (upper-levels). For the warm anomaly over melting parts of the GrIS, transport from these regions was about twice as important as diabatic warming along the trajectories. Transport seems even more relevant regarding the thermodynamical trajectory categorization, where descending (C3) and northwards advected (C4) air masses account for 75% of air masses arriving over the GrIS during EV69. In the following, we will discuss the reasoning from these two methodologies applied to all 77 warm events in 1979–2017.

4.2   Warm Event Climatology: Physical Processes of Warming

We categorized the trajectories causing GrIS melt into four categories according to their thermodynamic evolution, characterized as groups of mainly (C1) ascending, (C2) southward moving, (C3) descending and (C4) northward moving air masses, respectively. C2 air masses, identified by diabatic warming along their trajectory, appear to be negligible for warm events. The other three groups of trajectories are all contributing substantially to Greenland warm events and their frequency depends on the region of the GrIS. We will discuss vertical motion and transport in general together with the related heating/cooling mechanisms in Sec. 4.2.1. Warmer than usual air masses can contain more moisture, which is highly relevant for the surface energy budget via emission of longwave radiation and cloud modulation, which we will discuss in Sec. 4.2.2. Finally, Sec. 4.2.3 addresses the combination of climate warming and circulation anomalies observed over the past decades.

4.2.1   Transport and Adiabatic Warming

During ∼70–85% of the warm events affecting the regions SW, CW, NW, NE, CE and SE, all elevated around 2000 m, an atmospheric blocking is located in the GBI region with its center over the central to southeastern GrIS. Our warm event climatology (Appendix Tabs. 1–3) is in good agreement with extreme blocking days identified by McLeod and Mote (2016). Additionally, the Icelandic Low is mostly absent while cyclones are more frequent over Newfoundland during SW warm events, over the Canadian Arctic during NW, NE and CE warm events and along the southern edge of the North Atlantic storm track during CE warm events, respectively. This synoptic setup

shifts the air mass origin significantly southwards compared to climatology, ranging from 9.6° latitude in the SE to 17.0° latitude in the NE of Greenland, respectively.

Southerly and anomalously warm air masses bring a lot of moisture to the western inflow of the blocking (e.g., Pfahl et al., 2015), i.e., to the southern and western GrIS. The air masses experience orographic lifting in the surroundings of Greenland, which induces condensation and also precipitation. The associated diabatic heating is typically around 2 K within 12 h prior to arrival over the SW GrIS. The final steep ascent of ∼100 hPa is further evident during NW warm events, and, less pronounced, for some trajectories arriving in the CW or SE of the ice sheet. Mainly northward moving (C4) and additionally ascending (C1) trajectories make up the majority (∼70%) of air masses causing melt in these four regions. Warm event air masses arriving over the north- and central eastern GrIS show very distinct properties. Air masses from the mid-troposphere descend in the anticyclonic flow over the GrIS ridge. As a consequence, the air masses dry off and are warmed adiabatically to the highest temperatures (+1°C to +3°C) and largest $TH10M$ anomaly (∼+7 K) of all regions. Thus, the most frequent trajectory category is C3, representing mainly descending air masses, as expected in the proximity of the blocking center (e.g., Sousa et al., 2018).

Adiabatic warming by descent releases potential warmth by compression. It is thus equivalent to transport from a climatologically warmer region and different from diabatic processes that generate warming themselves. After excluding longwave cooling, diabatic processes along the trajectories (Di) cause the majority of the warm anomaly in SW Greenland (contribution ratio $R_{Di/Tr} = 1.13$). On the contrary, transport (Tr) is about twice as important as diabatic warming for warm events in the north- and central eastern GrIS ($R_{Di/Tr} = 0.54$ and 0.52, respectively). In SE and NW Greenland, where ascent is weaker than in the SW, the ratio of the contributions of Di and Tr is 0.82 and 0.83, respectively.

4.2.2 Moisture and Surface Radiation Budget

Except for the (north-)eastern GrIS, warm events typically involve moist air streams, which, as such or later as clouds, strongly influence the surface energy budget. Also, incoming radiation in the dry, clear-sky regions of a blocking is a substantial contribu-

tor to surface melt. We detect warm events based on skin temperature, resulting from the surface energy balance (Berrisford et al., 2011), and thus accounting for (cloud) radiative effects. The representation of spatiotemporal heterogeneity and the current decrease in albedo in ERA-Interim, however, is insufficient (Cao et al., 2016). Hence we tend to underestimate the duration and frequency of Greenland warm events with our definition. More importantly, our trajectory analysis presumably obscures most (cloud) radiative effects at the ice sheet surface, due to the Lagrangian framework and the lowest trajectories arriving 20 hPa ($\sim$200 m) agl. Discussing the net energy budget at the ice sheet surface will complete the assessment of Greenland warm events.

Simple temperature-based indices show reasonable performance to estimate GrIS surface melt (e.g., Ohmura, 2001; Van den Broeke et al., 2010). Longwave radiation and non-radiative turbulent fluxes including rain, which are highly temperature dependent, did indeed contribute substantially to extreme melting periods (Tedesco et al., 2008; Fausto et al., 2016). Over the whole GrIS, however, the spatially heterogeneous effects of solar radiation and clouds become increasingly important during atmospheric blocking conditions. During polar winter and nighttime, it is clear that the cloud radiative effect is warming and thus enhancing melt, as there is no incoming solar radiation (Park et al., 2015; Van Tricht et al., 2016). The cloud radiative effect over an entire summer day, however, is highly disputed.

On the one hand, warm air advection (sensible heating) and reduced snowfall lead to an albedo decrease, which triggers the albedo feedback that causes melt via an increased downward shortwave flux (Box et al., 2012). As the low albedo areas are typically melting in summer (ablation area), net radiation towards the GrIS margin increases rapidly (Van den Broeke et al., 2008). On the other hand, around Summit Station, in the high albedo accumulation area, surface melt would not have been observed during EV69 without the presence of optically thin low-level liquid clouds (Bennartz et al., 2013). Their optical thickness optimally lies in an intermediate range that lets solar radiation penetrate, but blocks and emits longwave radiation downward. The study by Van Tricht et al. (2016) is representative for the common idea of clouds as a warming shield with a net warming effect over the whole GrIS. This is opposed to the concurrent reduction of summer cloud cover and triggered melt albedo feedback in periods with above-normal $Z500$ (Hofer et al., 2017). Hofer et al. (2017) found very

low correlation between longwave downward radiation and cloud cover anomalies, but much better agreement of the total effect of (i) increased shortwave downward radiation plus (ii) longwave downward radiation from higher free-atmosphere temperatures with surface melt. Circulation-induced (NAO−/GBI+) moistening and warming of the lower atmosphere, which was observed in the 2000s, directly increases the net surface radiation and accelerates GrIS melt (Mattingly et al., 2016; Ding et al., 2017).

We conclude, that (i) clear-sky moistening, going along with warm events, increases the net radiation at the surface; (ii) clouds that were observed during SW, CW, NW and SE warm events, respectively, reduce melt in the ablation area, where surface albedo is low and the melting effect of solar radiation would be amplified by the albedo feedback – Wang et al. (2019) found that this effect is especially important to melting of the western GrIS; (iii) rain, mostly affecting the southern and western GrIS, enhances melt directly and with hindsight via the albedo feedback (Fausto et al., 2016); and (iv) clouds in the high albedo accumulation area are warming, especially if their optical thickness lies in the optimal intermediate range. Let us additionally consider that cloud radiative effects are unevenly distributed within an atmospheric blocking, which is the key feature of Greenland warm events. Downward shortwave radiation in the blocking center is enhanced, while its moist periphery promotes increased downward longwave radiation (Wernli and Papritz, 2018). All in all, blocking conditions could induce a net zero radiative effect at the ice sheet surface in moist South and West Greenland – as cloud cooling and warming by elevated moisture content balance – and enhance surface melt in the dry and clear-sky inland and Northeast of the GrIS. If cloudy conditions go along with rain, the additional rain energy flux into the GrIS fosters melt in the respective regions.

4.2.3 Climate Change and Inter-Annual Variability

We compare summer $TH10M$ over the GrIS with its 9-yr moving average, i.e., the transient climate, and attribute the remainder to inter-annually variable large-scale dynamics. In our study period, the transient climate remained stationary until 1996 and then warmed by about 1°C. The additional dynamically induced temperature anomaly ranged from -1.8 ± 0.8°C in 1992 (98% of the total cold anomaly) to $+1.5 \pm 0.6$°C in 2012 (57% of the total warm anomaly). Fettweis et al. (2013) attributed 70% of the

1993–2012 warming trend to atmospheric circulation changes. For years after 2002 – years of high geopotential $Z500$ around Greenland manifest in constantly high GBI (Hanna et al., 2018) and low NAO index (Fettweis et al., 2013; Hanna et al., 2015) – our analysis is limited and thus underrates the importance of large-scale circulation. We, however, identify that Greenland blocks are relevant to more than 70% of the warm events in 1979–2017, and understanding of their development and lifespan are highly relevant to Greenland's climate, GrIS mass loss (Hanna et al., 2014; Van den Broeke et al., 2017) and global sea-level rise (Van den Broeke et al., 2016; Box et al., 2018). Global climate models are yet not able to capture the strong and persistent NAO− circulation anomalies of recent years (Fettweis et al., 2012, 2013). If these changes are the result of natural variability, long-term trends predicted by the models could still be trustworthy, as the model performance is limited by the internal variability of the climate system (Fischer et al., 2013; Knutti and Sedláček, 2013). Predicted long-term trends of summer NAO predict no significant changes towards the end of this century (e.g., Gillett and Fyfe, 2013). If the current decrease in summer NAO, however, is systematic, the ability of today's climate models to simulate future trends in the North Atlantic circulation is questionable, and GrIS mass loss at the end of this century could be underestimated by a factor of two (Delhasse et al., 2018).

Other studies based on reanalysis and model data, however, suggest an increase in extratropical blocking frequency and duration due to climate change (Coumou and Rahmstorf, 2012; Mokhov et al., 2013). We agree on these trends; the warm event frequency increased from 1.8 to 2.8 events per year between the "recent past" (1986–2005) and "present day" (2005–2015) reference periods according to IPCC Special Report on the Ocean and Cryosphere in a Changing Cliamte (SROCC); the average warm event duration increased from below four to above five days and the longest events increased from 9–11 d to 15–17 d. The typical eastward propagation of Rossby waves is hypothesized to slow down as a result of weaker zonal winds and growing amplitude due to the Arctic amplification (Francis and Vavrus, 2012). Blocking, i.e., stationary wave patterns, are thus more likely, which is also the case in winter (Liu et al., 2012). An example of a stationary, large-amplitude wave was observed in July 2015, when a geopotential height anomaly of 3.7σ evolved over the Arctic ocean and promoted higher surface temperatures, increased runoff and lower albedo over North Greenland (Tedesco et al., 2016b). As the ridge was not centered over Greenland itself,

surface melting in the southern GrIS was inhibited and we detect a warm event with maximum melt extent of 53%.

It remains difficult to pigeonhole the recent series of NAO− years. Is it a statistically plausible clustering of extreme years or rather a systematic shift in the North Atlantic circulation? Global climate models do not predict a decrease in summer NAO with climate change. Theoretical and observational evidence, however, point to an increase in blocking days over Greenland, in parallel with the reduced temperature gradient between polar and equatorial regions. Warm events would thus become much more frequent, enhance melting, especially in the ablation area of the GrIS, and would further accelerate Greenland mass loss towards the end of this century.

Chapter 5

Conclusions

We present a climatology of 77 Greenland warm events in summer 1979–2017, when at least 5% of the Greenland Ice Sheet (GrIS) area was melting and located above 2000 m (Sec. 3.2 and Appendix Tabs. 1–3), based on the ERA-Interim reanalysis. Such warm events have become 60% more frequent and increased in duration between the "recent past" (1986–2005) and "present day" (2005–2015) reference periods. Since the late 1990s, many summers characterized by NAO−/GBI+ circulation and thus increased geopotential height, surface pressure and blocking frequency over the GrIS followed each other. A link between the GrIS near-surface temperature anomaly induced by such atmospheric flow configurations and the occurrence of warm events is evident from our results. The GrIS near-surface climate warmed on average by about +1°C – warming hot spots are North and East Greenland including the Scoresbysund fjord (Sec. 3.1). Yet circulation-induced summertime temperature anomalies are on the same order of magnitude and result in a pronounced year-to-year variability.

Increased geopotential height and blocking anticyclones over Greenland are the key synoptic features during Greenland warm events – besides increased cyclone frequency over Newfoundland or the Canadian Arctic. 70–85% of the warm events are linked to a Greenland blocking, more often when they affect the northern and eastern GrIS (Sec. 3.5.3). There, air masses originate from the mid-troposphere, 14.0–17.0° latitude further south than usual and descend anticyclonically after crossing the GrIS ice divide (Secs. 3.5.2 and 3.5.4). Trajectories descending by more than 300 hPa are more frequent than in the 1979–2017 average flow, and consequently, most trajectories gain warmth by adiabatic descent. Northwest Greenland is typically approached by air masses from the Baffin Bay. During Central West, Southwest and Southeast Green-

land warm events, respectively, trajectories come from both sides of the ice divide but preferably from Newfoundland. Their southernmost position during the ten days prior to the event was 9.6–13.3° latitude more south than in the climatology. Subsidence is found as a relevant contributor to warming, especially in Central West and Southeast Greenland, but the major source of warming in these four regions comes from northward advection in combination with orographic ascent onto the GrIS.

The thermodynamic effect of adiabatic descent is equivalent to that of air mass advection from a climatologically warmer region, summarized as transport. For warm events affecting North and East Greenland, and also for the extensive July 2012 event, transport is about twice as important as diabatic heating (Sec. 3.5.4). In the remaining parts of the ice sheet, both warming processes are relevant. But only in Southwest Greenland, the temperature anomaly in the lowermost $\sim$500 m of the atmosphere mainly comes from diabatic heating related to the ascent of moist air masses. During warm events, moist air masses are advected towards the Southwest of Greenland, which is located in the western periphery of the blocking, leading to a pronounced moisture gradient over the GrIS (Sec. 3.5.3). This has implications for the spatial distribution of surface energy budget anomalies, which we suggest induce additional ice melt; mainly by turbulent heat fluxes in South and West, and increased downward shortwave radiation in Central, North and East Greenland, respectively (Sec. 4.2.2). More detailed research on the effects of cloud cover and atmospheric moisture content on the surface energy budget is needed to get a coherent picture of surface melt during Greenland blocking.

Our Lagrangian analyses shed light on the air mass evolution prior to warm events, which modified, for example, our understanding of the July 2012 extreme melt event. Most air masses ending up over the GrIS did not come from the US Great Plains, which experienced a historic heat wave, but from the Canadian Arctic, Newfoundland and the subtropical North Atlantic. We therefore promote the use of trajectory-based analyses, in addition to more conventional methodologies, to assess the insitu modification of air masses. Further, as Greenland warm events are highly dependent on the atmospheric flow configuration, a better understanding of the effect of global climate change on the atmospheric dynamics in the North Atlantic region is crucial to more accurately predict the future mass loss from the GrIS.

References

Andersen, M. L., Stenseng, L., Skourup, H., Colgan, W., Khan, S. A., Kristensen, S. S., Andersen, S. B., Box, J. E., Ahlstrøm, A. P., Fettweis, X., et al. (2015). Basin-scale partitioning of Greenland ice sheet mass balance components (2007–2011). *Earth Planet. Sci. Lett.*, 409:89–95. https://doi.org/10.1016/j.epsl.2014.10.015.

Bennartz, R., Shupe, M. D., Turner, D. D., Walden, V. P., Steffen, K., Cox, C. J., Kulie, M. S., Miller, N., and Pettersen, C. (2013). July 2012 Greenland melt extent enhanced by low-level liquid clouds. *Nature*, 496(7443):83. https://doi.org/10.1038/nature12002.

Berrisford, P., Dee, D., Poli, P., Brugge, R., Fielding, K., Fuentes, M., Kallberg, P., Kobayashi, S., Uppala, S., and Simmons, A. (2011). The ERA-Interim archive version 2.0, era report series 1, ecmwf, shinfield park. *Reading, UK*, 13177. http://www.ecmwf.int/publications/library/do/references/show?id=90276.

Bieli, M., Pfahl, S., and Wernli, H. (2015). A lagrangian investigation of hot and cold temperature extremes in Europe. *Quart. J. Roy. Meteor. Soc.*, 141(686):98–108. https://doi.org/10.1002/qj.2339.

Binder, H., Boettcher, M., Grams, C. M., Joos, H., Pfahl, S., and Wernli, H. (2017). Exceptional air mass transport and dynamical drivers of an extreme wintertime Arctic warm event. *Geophys. Res. Lett.*, 44(23). http://dx.doi.org/10.1002/2017GL075841.

Bonne, J.-L., Steen-Larsen, H. C., Risi, C., Werner, M., Sodemann, H., Lacour, J.-L., Fettweis, X., Cesana, G., Delmotte, M., Cattani, O., et al. (2015). The summer 2012 Greenland heat wave: In situ and remote sensing observations of water vapor isotopic composition during an atmospheric river event. *J. Geophys. Res. Atmos.*, 120(7):2970–2989. https://doi.org/10.1002/2014JD022602.

References

Box, J. E., Bromwich, D. H., and Bai, L.-S. (2004). Greenland Ice Sheet surface mass balance 1991–2000: Application of polar mm5 mesoscale model and in situ data. *J. Geophys. Res. Atmos.*, 109(D16). https://doi.org/10.1029/2003JD004451.

Box, J. E., Colgan, W. T., Wouters, B., Burgess, D. O., O'Neel, S., Thomson, L. I., and Mernild, S. H. (2018). Global sea-level contribution from Arctic land ice: 1971–2017. *Environ. Res. Lett.*, 13(12):125012. https://doi.org/10.1088/1748-9326/aaf2ed.

Box, J. E., Fettweis, X., Stroeve, J. C., Tedesco, M., Hall, D. K., and Steffen, K. (2012). Greenland Ice Sheet albedo feedback: thermodynamics and atmospheric drivers. *Cryosphere*, 6(4):821–839. https://doi.org/10.5194/tc-6-821-2012.

Cao, Y., Liang, S., He, T., and Chen, X. (2016). Evaluation of four reanalysis surface albedo data sets in Arctic using a satellite product. *IEEE Geoscience and Remote Sensing Letters*, 13(3):384–388. https://doi.org/10.1109/LGRS.2016.2515159.

Cappelen, J. (2014). Greenland- DMI historical climate data collection 1784–2013. *Denmark, The Faroe Islands and Greenland.* http://www.dmi.dk/laer-om/generelt/dmi-publikationer/.

Cavallo, S. M. and Hakim, G. J. (2013). Physical mechanisms of tropopause polar vortex intensity change. *J. Atmos. Sci.*, 70(11):3359–3373. https://doi.org/10.1175/JAS-D-13-088.1.

Chen, L., Fettweis, X., Knudsen, E. M., and Johannessen, O. M. (2016). Impact of cyclonic and anticyclonic activity on Greenland Ice Sheet surface mass balance variation during 1980–2013. *Int. J. Climatol.*, 36(10):3423–3433. https://doi.org/10.1002/joc.4565.

Coumou, D. and Rahmstorf, S. (2012). A decade of weather extremes. *Nat. Clim. Change*, 2(7):491. https://doi.org/10.1038/nclimate1452.

Dee, D. P., Uppala, S. M., Simmons, A. J., Berrisford, P., Poli, P., Kobayashi, S., Andrae, U., Balmaseda, M. A., Balsamo, G., Bauer, d. P., et al. (2011). The ERA-Interim reanalysis: Configuration and performance of the data assimilation system. *Quart. J. Roy. Meteor. Soc.*, 137(656):553–597. https://doi.org/10.1002/qj.828.

Delhasse, A., Fettweis, X., Kittel, C., Amory, C., and Agosta, C. (2018). Brief communication: Impact of the recent atmospheric circulation change in summer

on the future surface mass balance of the Greenland Ice Sheet. *Cryosphere*. http://dx.doi.org/10.5194/tc-12-3409-2018.

Ding, Q., Schweiger, A., L'Heureux, M., Battisti, D. S., Po-Chedley, S., Johnson, N. C., Blanchard-Wrigglesworth, E., Harnos, K., Zhang, Q., Eastman, R., et al. (2017). Influence of high-latitude atmospheric circulation changes on summertime Arctic sea ice. *Nat. Clim. Change*, 7(4):289. https://doi.org/10.1038/nclimate3241.

Enderlin, E. M., Howat, I. M., Jeong, S., Noh, M.-J., Van Angelen, J. H., and Van Den Broeke, M. R. (2014). An improved mass budget for the Greenland Ice Sheet. *Geophys. Res. Lett.*, 41(3):866–872. https://doi.org/10.1002/2013GL059010.

Fausto, R. S., van As, D., Box, J. E., Colgan, W., Langen, P. L., and Mottram, R. H. (2016). The implication of nonradiative energy fluxes dominating Greenland Ice Sheet exceptional ablation area surface melt in 2012. *Geophys. Res. Lett.*, 43(6):2649–2658. https://doi.org/10.1002/2016GL067720.

Fettweis, X., Box, J., Agosta, C., Amory, C., Kittel, C., Lang, C., van As, D., Machguth, H., and Gallée, H. (2017). Reconstructions of the 1900–2015 Greenland Ice Sheet surface mass balance using the regional climate MAR model. *Cryosphere*, 11:1015–1033. http://dx.doi.org/10.5194/tc-11-1015-2017.

Fettweis, X., Franco, B., Tedesco, M., Van Angelen, J. H., Lenaerts, J. T. M., Van den Broeke, M. R., and Gallée, H. (2012). Estimating Greenland Ice Sheet surface mass balance contribution to future sea level rise using the regional atmospheric climate model MAR. *Cryosphere*, 6:3101–3147. https://doi.org/10.5194/tc-7-469-2013.

Fettweis, X., Hanna, E., Lang, C., Belleflamme, A., Erpicum, M., and Gallée, H. (2013). Important role of the mid-tropospheric atmospheric circulation in the recent surface melt increase over the Greenland Ice Sheet. *Cryosphere*, 7:241–248. http://dx.doi.org/10.5194/tc-7-241-2013.

Fischer, E. M., Beyerle, U., and Knutti, R. (2013). Robust spatially aggregated projections of climate extremes. *Nat. Clim. Change*, 3(12):1033. https://doi.org/10.1038/nclimate2051.

Francis, D., Eayrs, C., Chaboureau, J.-P., Mote, T., and Holland, D. M. (2018). Polar jet associated circulation triggered a saharan cyclone and derived the poleward

transport of the african dust generated by the cyclone. *J. Geophys. Res. Atmos.*, 123(21):11–899. https://doi.org/10.1029/2018JD029095.

Francis, J. A. and Vavrus, S. J. (2012). Evidence linking Arctic amplification to extreme weather in mid-latitudes. *Geophys. Res. Lett.*, 39(6). https://doi.org/10.1029/2012GL051000.

Gallagher, M. R., Shupe, M. D., and Miller, N. B. (2018). Impact of atmospheric circulation on temperature, clouds, and radiation at Summit Station, Greenland, with self-organizing maps. *J. Climate*, 31(21):8895–8915. https://doi.org/10.1175/JCLI-D-17-0893.1.

Gillett, N. P. and Fyfe, J. C. (2013). Annular mode changes in the CMIP5 simulations. *Geophys. Res. Lett.*, 40(6):1189–1193. https://doi.org/10.1002/grl.50249.

Gillett, N. P., Stone, D. A., Stott, P. A., Nozawa, T., Karpechko, A. Y., Hegerl, G. C., Wehner, M. F., and Jones, P. D. (2008). Attribution of polar warming to human influence. *Nat. Geosci.*, 1(11):750. https://doi.org/10.1038/ngeo338.

Hall, D. K., Comiso, J. C., DiGirolamo, N. E., Shuman, C. A., Box, J. E., and Koenig, L. S. (2013). Variability in the surface temperature and melt extent of the Greenland Ice Sheet from MODIS. *Geophys. Res. Lett.*, 40(10):2114–2120. https://doi.org/10.1002/grl.50240.

Hanna, E., Cropper, T. E., Hall, R. J., and Cappelen, J. (2016). Greenland Blocking Index 1851–2015: a regional climate change signal. *Int. J. Climatol.*, 36(15):4847–4861. https://doi.org/10.1002/joc.4673.

Hanna, E., Cropper, T. E., Jones, P. D., Scaife, A. A., and Allan, R. (2015). Recent seasonal asymmetric changes in the NAO (a marked summer decline and increased winter variability) and associated changes in the AO and Greenland Blocking Index. *Int. J. Climatol.*, 35(9):2540–2554. https://doi.org/10.1002/joc.4157.

Hanna, E., Fettweis, X., Mernild, S. H., Cappelen, J., Ribergaard, M. H., Shuman, C. A., Steffen, K., Wood, L., and Mote, T. L. (2014). Atmospheric and oceanic climate forcing of the exceptional Greenland Ice Sheet surface melt in summer 2012. *Int. J. Climatol.*, 34(4):1022–1037. https://doi.org/10.1002/joc.3743.

Hanna, E., Hall, R. J., Cropper, T. E., Ballinger, T. J., Wake, L., Mote, T., and Cappelen, J. (2018). Greenland blocking index daily series 1851–2015: Analysis of changes in extremes and links with North Atlantic and UK climate variability and change. *Int. J. Climatol.* https://doi.org/10.1002/joc.5516.

Hanna, E., Huybrechts, P., Janssens, I., Cappelen, J., Steffen, K., and Stephens, A. (2005). Runoff and mass balance of the Greenland Ice Sheet: 1958–2003. *J. Geophys. Res. Atmos.*, 110(D13). https://doi.org/10.1029/2004JD005641.

Hanna, E., Jones, J. M., Cappelen, J., Mernild, S. H., Wood, L., Steffen, K., and Huybrechts, P. (2013). The influence of North Atlantic atmospheric and oceanic forcing effects on 1900–2010 Greenland summer climate and ice melt/runoff. *Int. J. Climatol.*, 33(4):862–880. https://doi.org/10.1002/joc.3475.

Harden, B. E. and Renfrew, I. A. (2012). On the spatial distribution of high winds off southeast Greenland. *Geophys. Res. Lett.*, 39(14). https://doi.org/10.1029/2012GL052245.

Hoerling, M., Eischeid, J., Kumar, A., Leung, R., Mariotti, A., Mo, K., Schubert, S., and Seager, R. (2014). Causes and predictability of the 2012 Great Plains drought. *Bull. Amer. Meteor. Soc.*, 95(2):269–282. https://doi.org/10.1175/BAMS-D-13-00055.1.

Hofer, S., Tedstone, A. J., Fettweis, X., and Bamber, J. L. (2017). Decreasing cloud cover drives the recent mass loss on the Greenland Ice Sheet. *Sci. Adv.*, 3(6):e1700584. https://doi.org/10.1126/sciadv.1700584.

Holton, J. R. and Hakim, G. J. (2012). *An introduction to dynamic meteorology*, volume 88. Academic Press, 5th edition.

Hurrell, J. and National Center for Atmospheric Research Staff (Eds.) (2018). The climate data guide: Hurrell North Atlantic Oscillation (NAO) index (station-based). https://climatedataguide.ucar.edu/climate-data/hurrell-north-atlantic-oscillation-nao-index-station-based. Last modified 04 Aug 2018. Accessed 18 Mar 2019.

Hurrell, J. W., Kushnir, Y., Ottersen, G., and Visbeck, M. (2013). *An Overview of the North Atlantic Oscillation*, pages 1–35. American Geophysical Union (AGU).

References

Johannessen, O. M., Bengtsson, L., Miles, M. W., Kuzmina, S. I., Semenov, V. A., Alekseev, G. V., Nagurnyi, A. P., Zakharov, V. F., Bobylev, L. P., Pettersson, L. H., et al. (2004). Arctic climate change: observed and modelled temperature and sea-ice variability. *TELLUS A*, 56(4):328–341. https://doi.org/10.3402/tellusa.v56i4.14418.

Kjeldsen, K. K., Korsgaard, N. J., Bjørk, A. A., Khan, S. A., Box, J. E., Funder, S., Larsen, N. K., Bamber, J. L., Colgan, W., Van Den Broeke, M., et al. (2015). Spatial and temporal distribution of mass loss from the Greenland Ice Sheet since AD 1900. *Nature*, 528(7582):396. https://doi.org/10.1038/nature16183.

Knutti, R. and Sedláček, J. (2013). Robustness and uncertainties in the new CMIP5 climate model projections. *Nat. Clim. Change*, 3(4):369. https://doi.org/10.1038/nclimate1716.

Lenaerts, J. T. M., Van den Broeke, M. R., Van Angelen, J. H., Van Meijgaard, E., and Déry, S. J. (2012). Drifting snow climate of the Greenland Ice Sheet: a study with a regional climate model. *Cryosphere*, 6:891–899. https://doi.org/10.5194/tc-6-891-2012.

Lesins, G., Duck, T. J., and Drummond, J. R. (2012). Surface energy balance framework for Arctic amplification of climate change. *J. Climate*, 25(23):8277–8288. https://doi.org/10.1175/JCLI-D-11-00711.1.

Liu, J., Curry, J. A., Wang, H., Song, M., and Horton, R. M. (2012). Impact of declining Arctic sea ice on winter snowfall. *PNAS*, 109(11):4074–4079. https://doi.org/10.1073/pnas.1114910109.

Marzeion, B., Cogley, J. G., Richter, K., and Parkes, D. (2014). Attribution of global glacier mass loss to anthropogenic and natural causes. *Science*, page 1254702. https://doi.org/10.1126/science.1254702.

Marzeion, B., Kaser, G., Maussion, F., and Champollion, N. (2018). Limited influence of climate change mitigation on short-term glacier mass loss. *Nat. Clim. Change*, 8(4):305. https://doi.org/10.1038/s41558-018-0093-1.

Mattingly, K. S., Ramseyer, C. A., Rosen, J. J., Mote, T. L., and Muthyala, R. (2016). Increasing water vapor transport to the Greenland Ice Sheet

revealed using self-organizing maps. *Geophys. Res. Lett.*, 43(17):9250–9258. https://doi.org/10.1002/2016GL070424.

McLeod, J. T. and Mote, T. L. (2016). Linking interannual variability in extreme Greenland blocking episodes to the recent increase in summer melting across the Greenland Ice Sheet. *Int. J. Climatol.*, 36(3):1484–1499. https://doi.org/10.1002/joc.4440.

Meese, D. A., Gow, A. J., Grootes, P., Stuiver, M., Mayewski, P. A., Zielinski, G. A., Ram, M., Taylor, K. C., and Waddington, E. D. (1994). The accumulation record from the GISP2 core as an indicator of climate change throughout the Holocene. *Science*, 266(5191):1680–1682. https://doi.org/10.1126/science.266.5191.1680.

Mokhov, I. I., Akperov, M. G., Prokofyeva, M. A., Timazhev, A. V., Lupo, A. R., and Le Treut, H. (2013). Blockings in the Northern hemisphere and Euro-Atlantic region: estimates of changes from reanalysis data and model simulations. In *Doklady Earth Sci.*, volume 449, pages 430–433. Citeseer. https://doi.org/10.1134/S1028334X13040144.

Neff, W., Compo, G. P., Ralph, F. M., and Shupe, M. D. (2014). Continental heat anomalies and the extreme melting of the Greenland ice surface in 2012 and 1889. *J. Geophys. Res. Atmos.*, 119(11):6520–6536. https://doi.org/10.1002/2014JD021470.

Nghiem, S. V., Hall, D. K., Mote, T. L., Tedesco, M., Albert, M. R., Keegan, K., Shuman, C., DiGirolamo, N. E., and Neumann, G. (2012). The extreme melt across the Greenland Ice Sheet in 2012. *Geophys. Res. Lett.*, 39(20). https://doi.org/10.1029/2012GL053611.

Nielsen, A. B. (2010). Present conditions in Greenland and the Kangerlussuaq area. Technical report, Posiva Oy. http://www.posiva.fi/files/1244/WR_2010-07web.pdf.

Noël, B., Fettweis, X., Van De Berg, W. J., Van Den Broeke, M. R., and Erpicum, M. (2014). Sensitivity of Greenland Ice Sheet surface mass balance to perturbations in sea surface temperature and sea ice cover: a study with the regional climate model MAR. *Cryosphere*, 8:1871–1883. http://dx.doi.org/10.5194/tc-8-1871-2014.

Ohmura, A. (2001). Physical basis for the temperature-based melt-index method. *J. Appl. Meteorol. Climatol.*, 40(4):753–761. https://doi.org/10.1175/1520-0450(2001)040<3C0753:PBFTTB>3E2.0.CO;2.

Papritz, L. and Spengler, T. (2017). A Lagrangian climatology of wintertime cold air outbreaks in the Irminger and Nordic Seas and their role in shaping air–sea heat fluxes. *J. Climate*, 30(8):2717–2737. https://doi.org/10.1175/JCLI-D-16-0605.1.

Park, H.-S., Lee, S., Kosaka, Y., Son, S.-W., and Kim, S.-W. (2015). The impact of Arctic winter infrared radiation on early summer sea ice. *J. Climate*, 28(15):6281–6296. https://doi.org/10.1175/JCLI-D-14-00773.1.

Petersen, G. N., Ólafsson, H., and Kristjánsson, J. E. (2003). Flow in the lee of idealized mountains and Greenland. *J. Atmos. Sci.*, 60(17):2183–2195. https://doi.org/10.1175/1520-0469(2003)060<3C2183:FITLOI>3E2.0.CO;2.

Pfahl, S., Schwierz, C., Croci-Maspoli, M., Grams, C. M., and Wernli, H. (2015). Importance of latent heat release in ascending air streams for atmospheric blocking. *Nat. Geosci.*, 8(8):610. https://doi.org/10.1038/ngeo2487.

Raveh-Rubin, S. (2017). Dry intrusions: Lagrangian climatology and dynamical impact on the planetary boundary layer. *J. Climate*, 30(17):6661–6682. https://doi.org/10.1175/JCLI-D-16-0782.1.

Renfrew, I. A., Moore, G. W. K., Kristjánsson, J. E., Olafsson, H., Gray, S. L., Petersen, G. N., Bovis, K., Brown, P. R. A., Føre, I., Haine, T., et al. (2008). The Greenland flow distortion experiment. *Bull. Am. Meteorol. Soc.*, 89(9):1307–1324. https://doi.org/10.1175/2008BAMS2508.1.

Serreze, M. C. and Barry, R. G. (2011). Processes and impacts of Arctic amplification: A research synthesis. *Glob. Planet. Change*, 77(1-2):85–96. https://doi.org/10.1016/j.gloplacha.2011.03.004.

Škerlak, B. (2014). *Climatology and process studies of tropopause folds, cross-tropopause exchange, and transport into the boundary layer*. PhD thesis, ETH Zurich. https://doi.org/10.3929/ethz-a-010256937.

Sousa, P. M., Trigo, R. M., Barriopedro, D., Soares, P. M. M., and Santos, J. A. (2018). European temperature responses to blocking and ridge regional patterns. *Clim. Dyn.*, 50(1-2):457–477. https://doi.org/10.1007/s00382-017-3620-2.

Sprenger, M., Fragkoulidis, G., Binder, H., Croci-Maspoli, M., Graf, P., Grams, C. M., Knippertz, P., Madonna, E., Schemm, S., Škerlak, B., et al. (2017). Global climatologies of Eulerian and Lagrangian flow features based on ERA-Interim. *Bull. Amer. Meteor. Soc.*, 98(8):1739–1748. https://doi.org/10.1175/BAMS-D-15-00299.1.

Sprenger, M. and Wernli, H. (2015). The LAGRANTO Lagrangian analysis tool–version 2.0. *Geosci. Model Dev.*, 8(8):2569–2586. https://doi.org/10.5194/gmd-8-2569-2015.

Tedesco, M., Box, J., Cappelen, J., Fettweis, X., Hansen, K., Mote, T., Smeets, P., van As, D., van de Wal, R., Velicogna, I., et al. (2016a). Greenland Ice Sheet [in "state of the climate in 2015"]. *Bull. Amer. Meteor. Soc.*, 97(8). https://doi.org/10.1175/2016BAMSStateoftheClimate.1.

Tedesco, M., Fettweis, X., Mote, T., Wahr, J., Alexander, P., Box, J., and Wouters, B. (2013). Evidence and analysis of 2012 Greenland records from spaceborne observations, a regional climate model and reanalysis data. *Cryosphere*, 7:615–630. https://doi.org/10.7916/D8J38SGV.

Tedesco, M., Mote, T., Fettweis, X., Hanna, E., Jeyaratnam, J., Booth, J. F., Datta, R., and Briggs, K. (2016b). Arctic cut-off high drives the poleward shift of a new Greenland melting record. *Nat. Commun.*, 7:11723. https://doi.org/10.1038/ncomms11723.

Tedesco, M., Serreze, M., and Fettweis, X. (2008). Diagnosing the extreme surface melt event over southwestern Greenland in 2007. *Cryosphere Discussions*, 2(3):383–397. https://hal.archives-ouvertes.fr/hal-00298544.

Våge, K., Spengler, T., Davies, H. C., and Pickart, R. S. (2009). Multi-event analysis of the westerly Greenland tip jet based upon 45 winters in ERA-40. *Quart. J. Roy. Meteor. Soc.*, 135(645):1999–2011. https://doi.org/10.1002/qj.488.

Van den Broeke, M., Box, J., Fettweis, X., Hanna, E., Noël, B., Tedesco, M., van As, D., van de Berg, W. J., and van Kampenhout, L. (2017). Greenland Ice Sheet surface mass loss: Recent developments in observation and modeling. *Curr. Clim. Change Rep.*, 3(4):345–356. https://doi.org/10.1007/s40641-017-0084-8.

References

Van den Broeke, M., Bus, C., Ettema, J., and Smeets, P. (2010). Temperature thresholds for degree-day modelling of Greenland Ice Sheet melt rates. *Geophys. Res. Lett.*, 37(18). http://dx.doi.org/10.1029/2010GL044123.

Van den Broeke, M., Smeets, P., Ettema, J., and Munneke, P. K. (2008). Surface radiation balance in the ablation zone of the west Greenland Ice Sheet. *J. Geophys. Res. Atmos.*, 113(D13). https://doi.org/10.1029/2007JD009283.

Van den Broeke, M. R., Enderlin, E. M., Howat, I. M., Kuipers Munneke, P., Noël, B. P., Jan Van De Berg, W., Van Meijgaard, E., and Wouters, B. (2016). On the recent contribution of the Greenland Ice Sheet to sea level change. *Cryosphere*, 10(5):1933–1946. https://doi.org/10.5194/tc-10-1933-2016, 2016.

Van Tricht, K., Lhermitte, S., Lenaerts, J. T. M., Gorodetskaya, I. V., L'Ecuyer, T. S., Noël, B., Van den Broeke, M. R., Turner, D. D., and van Lipzig, N. P. M. (2016). Clouds enhance Greenland Ice Sheet meltwater runoff. *Nat. Commun.*, 7:10266. https://doi.org/10.1038/ncomms10266.

Wang, W., Zender, C. S., van As, D., and Miller, N. B. (2019). Spatial distribution of melt season cloud radiative effects over Greenland: Evaluating satellite observations, reanalyses, and model simulations against in situ measurements. *J. Geophys. Res. Atmos.*, 124(1):57–71. https://doi.org/10.1029/2018JD028919.

Wernli, B. H. and Davies, H. C. (1997). A Lagrangian-based analysis of extratropical cyclones. I: The method and some applications. *Quart. J. Roy. Meteor. Soc.*, 123(538):467–489. https://doi.org/10.1002/qj.49712353811.

Wernli, H. and Papritz, L. (2018). Role of polar anticyclones and mid-latitude cyclones for Arctic summertime sea-ice melting. *Nat. Geosci.*, 11(2):108. https://doi.org/10.1038/s41561-017-0041-0.

Zhang, Y., Seidel, D. J., Golaz, J.-C., Deser, C., and Tomas, R. A. (2011). Climatological characteristics of Arctic and Antarctic surface-based inversions. *J. Climate*, 24(19):5167–5186. https://doi.org/10.1175/2011JCLI4004.1.

Zwally, H. J., Giovinetto, M. B., Beckley, M. A., and Saba, J. L. (2012). Antarctic and Greenland drainage systems, GSFC cryospheric sciences laboratory. *Available at icesat4.gsfc.nasa.gov/cryo_data/ant_grn_drainage_systems.php. Accessed March*, 1:2015. http://icesat4.gsfc.nasa.gov/cryo_data/ant_grn_drainage_systems.php.

Appendix

Table 1: Warm events EV1–25 listed with their start and end date ("YYYY-MM-DD HH"), duration (dur.), maximum elevation (ME), $T2M$ at maximum elevation (T2M$_{avg}^{ME}$), minimum melt extent (Min. A.) and maximum melt extent (Max. A.) – sorted by date.

ID	Start	End	Dur. [d]	ME [m]	T2M$_{avg}^{ME}$ [°C]	Min. A. [frac]	Max. A. [frac]
1	1979-07-24 18	1979-07-26 18	2.25	2606	−1.17	0.32	0.70
2	1981-06-25 18	1981-06-27 18	2.25	2549	−1.29	0.30	0.62
3	1981-07-21 12	1981-07-24 18	3.5	2729	2.44	0.25	0.59
4	1983-06-30 18	1983-07-01 18	1.25	2606	−0.27	0.25	0.67
5	1984-07-03 18	1984-07-08 18	5.25	2549	−1.72	0.19	0.68
6	1984-07-22 18	1984-07-24 18	2.25	2537	−0.57	0.22	0.66
7	1984-07-26 18	1984-07-27 18	1.25	2333	−0.06	0.34	0.61
8	1985-08-12 18	1985-08-14 18	2.25	2810	−0.51	0.23	0.54
9	1986-07-02 18	1986-07-03 18	1.25	2394	0.67	0.16	0.54
10	1986-07-20 18	1986-07-22 18	2.25	2729	2.43	0.29	0.53
11	1987-06-12 18	1987-06-13 18	1.25	2717	−1.17	0.26	0.56
12	1987-06-18 18	1987-06-22 18	4.25	2826	−1.87	0.13	0.63
13	1987-08-07 18	1987-08-10 18	3.25	2734	−1.07	0.15	0.72
14	1988-07-04 12	1988-07-12 18	8.5	2658	−0.10	0.20	0.69
15	1988-07-21 18	1988-07-22 18	1.25	2413	0.27	0.22	0.63
16	1989-07-13 18	1989-07-20 18	7.25	2810	−1.27	0.24	0.69
17	1990-07-28 18	1990-07-30 18	2.25	2748	−0.43	0.18	0.70
18	1990-08-05 18	1990-08-06 18	1.25	2628	−1.27	0.24	0.63
19	1991-06-18 18	1991-06-19 18	1.25	2810	−1.62	0.19	0.57
20	1991-06-26 18	1991-06-27 18	1.25	2394	−1.53	0.25	0.52
21	1991-06-29 12	1991-07-02 18	3.5	2606	−0.47	0.17	0.53
22	1991-07-04 18	1991-07-13 18	9.25	3000	−1.46	0.14	0.68
23	1994-07-07 18	1994-07-08 18	1.25	2443	0.55	0.27	0.68
24	1995-06-30 18	1995-07-03 18	3.25	2810	−0.25	0.17	0.65
25	1995-07-12 18	1995-07-16 18	4.25	2969	−0.36	0.24	0.77

Table 2: The same as Appendix Tab. 1 for EV26–59.

ID	Start	End	Dur. [d]	ME [m]	T2M$_{avg}^{ME}$ [°C]	Min. A. [frac]	Max. A. [frac]
26	1997-08-11 18	1997-08-13 18	2.25	2970	0.99	0.23	0.66
27	1998-08-01 18	1998-08-03 18	2.25	2637	−0.83	0.22	0.61
28	1999-06-28 18	1999-07-03 18	5.25	2721	−0.62	0.17	0.70
29	1999-07-25 18	1999-07-31 18	6.25	2628	−0.89	0.20	0.64
30	1999-08-02 18	1999-08-06 18	4.25	2826	−2.56	0.14	0.61
31	2000-07-28 18	2000-07-29 18	1.25	2637	0.49	0.39	0.70
32	2000-08-01 00	2000-08-02 18	2	2729	0.61	0.34	0.59
33	2000-08-19 18	2000-08-21 18	2.25	2634	0.43	0.19	0.53
34	2002-06-11 18	2002-06-14 18	3.25	2810	−0.67	0.13	0.71
35	2002-06-27 18	2002-07-03 18	6.25	3156	−0.44	0.25	1.08
36	2002-07-06 18	2002-07-07 18	1.25	2444	1.23	0.18	0.64
37	2002-07-20 18	2002-07-21 18	1.25	2719	−0.67	0.28	0.70
38	2003-08-26 18	2003-08-30 18	4.25	2729	−0.30	0.15	0.63
39	2004-06-18 12	2004-06-23 18	5.5	2826	−1.05	0.15	0.62
40	2004-07-05 18	2004-07-12 18	7.25	3175	−0.15	0.23	0.86
41	2004-08-11 18	2004-08-12 18	1.25	2810	−0.06	0.36	0.69
42	2005-06-13 18	2005-06-16 18	3.25	2628	0.67	0.17	0.70
43	2005-07-02 18	2005-07-03 18	1.25	2486	−0.17	0.23	0.68
44	2005-07-13 18	2005-07-15 18	2.25	2729	2.98	0.35	0.66
45	2005-07-21 18	2005-07-30 18	9.25	2916	−0.58	0.28	0.91
46	2006-07-19 18	2006-07-28 18	9.25	3100	−0.51	0.22	0.85
47	2006-08-03 18	2006-08-05 18	2.25	2606	−0.98	0.26	0.65
48	2006-08-15 00	2006-08-18 18	4	2758	−0.91	0.29	0.78
49	2007-06-10 18	2007-06-13 18	3.25	2637	1.88	0.20	0.63
50	2007-06-22 18	2007-06-29 18	7.25	2637	5.04	0.18	0.73
51	2007-07-06 18	2007-07-22 18	16.25	2658	0.70	0.20	0.74
52	2007-07-24 18	2007-07-25 18	1.25	2381	−2.37	0.27	0.65
53	2008-06-13 18	2008-06-14 18	1.25	2637	1.14	0.39	0.67
54	2008-06-17 18	2008-06-18 18	1.25	2482	2.37	0.18	0.55
55	2008-07-05 18	2008-07-06 18	1.25	2786	−0.91	0.40	0.76
56	2008-07-28 18	2008-07-31 18	3.25	2537	0.59	0.19	0.73
57	2009-07-06 18	2009-07-16 18	10.25	2943	−0.10	0.25	0.82
58	2009-07-20 18	2009-07-23 18	3.25	2486	0.09	0.22	0.71
59	2010-07-18 18	2010-07-19 18	1.25	2486	0.11	0.13	0.60

Table 3: The same as Appendix Tab. 1 for EV60–77.

ID	Start	End	Dur. [d]	ME [m]	T2M$_{\mathbf{avg}}^{\mathbf{ME}}$ [°C]	Min. A. [frac]	Max. A. [frac]
60	2010-07-23 18	2010-07-27 18	4.25	2486	-0.88	0.20	0.63
61	2010-07-29 18	2010-08-02 18	4.25	2537	-1.22	0.20	0.64
62	2010-08-09 18	2010-08-10 18	1.25	2455	-0.28	0.14	0.49
63	2010-08-15 18	2010-08-16 18	1.25	2628	-0.26	0.16	0.50
64	2011-06-13 18	2011-06-15 18	2.25	2856	0.93	0.10	0.68
65	2011-07-06 18	2011-07-10 18	4.25	2916	-0.78	0.24	0.73
66	2011-07-13 18	2011-07-15 18	2.25	2455	0.20	0.25	0.76
67	2011-07-18 18	2011-07-23 18	5.25	2526	0.03	0.21	0.69
68	2012-06-15 18	2012-06-29 18	14.25	2916	-1.81	0.18	0.81
69	2012-07-02 18	2012-07-17 18	15.25	3175	-0.13	0.23	1.21
70	2012-07-27 18	2012-08-08 18	12.25	3100	-1.08	0.22	0.96
71	2013-07-24 18	2013-07-28 18	4.25	2826	-2.44	0.17	0.71
72	2013-07-30 18	2013-08-02 18	3.25	2608	-1.07	0.16	0.62
73	2015-07-02 18	2015-07-09 18	7.25	2605	0.43	0.27	0.79
74	2016-06-10 18	2016-06-14 18	4.25	2652	-1.47	0.18	0.66
75	2016-06-22 18	2016-06-25 18	3.25	2581	2.50	0.23	0.55
76	2016-07-18 18	2016-07-24 18	6.25	2607	0.25	0.25	0.76
77	2017-07-25 12	2017-07-27 18	2.5	2628	1.98	0.28	0.76

Table 4: The 25th and 75th percentile of $\Theta_{anom}(t=0)$, $\Theta_{anom}(t=-10)$, transport-induced warm anomaly and diabatic cooling, respectively, whose medians are shown in Tab. 3.4.

	$\Theta_{\mathbf{anom}}(\mathbf{0})$	$\Theta_{\mathbf{anom}}(\mathbf{-10})$	Transport	Diabatics
Box SW	$[+3.3,+6.1]$ K	$[-1.8,+2.1]$ K	$[+1.7,+12.1]$ K	$[-7.5,+2.7]$ K
Box CW	$[+3.5,+6.4]$ K	$[-2.0,+2.4]$ K	$[+3.5,+13.8]$ K	$[-8.8,+0.8]$ K
Box NW	$[+2.9,+5.8]$ K	$[-2.0,+2.1]$ K	$[+3.5,+12.0]$ K	$[-7.3,+0.4]$ K
Box NE	$[+5.0,+8.0]$ K	$[-1.7,+1.5]$ K	$[+5.2,+15.2]$ K	$[-9.1,+0.6]$ K
Box CE	$[+5.2,+8.6]$ K	$[-1.9,+2.2]$ K	$[+5.8,+15.4]$ K	$[-8.7,+0.2]$ K
Box SE	$[+2.4,+6.2]$ K	$[-1.8,+2.6]$ K	$[+2.4,+12.7]$ K	$[-8.6,+1.0]$ K
EV69$_{\mathbf{warm}}$	$[+1.6,+7.0]$ K	$[-0.7,+3.3]$ K	$[+3.7,+13.0]$ K	$[-9.9,-1.1]$ K
EV69$_{\mathbf{all}}$	$[+0.3,+6.3]$ K	$[-0.6,+3.7]$ K	$[+1.7,+11.4]$ K	$[-9.3,-0.5]$ K
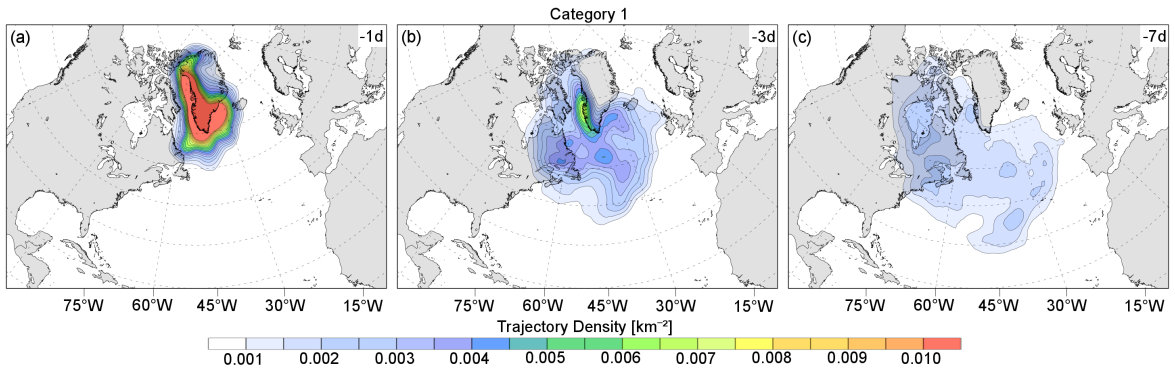
Figure 1: Trajectory density of all warm event trajectories in category 1 (Sec. 2.3.3) (a) 1 d, (b) 3 d and (c) 7 d prior to arrival, based on the gridding tool v2.4.2 (Škerlak, 2014).
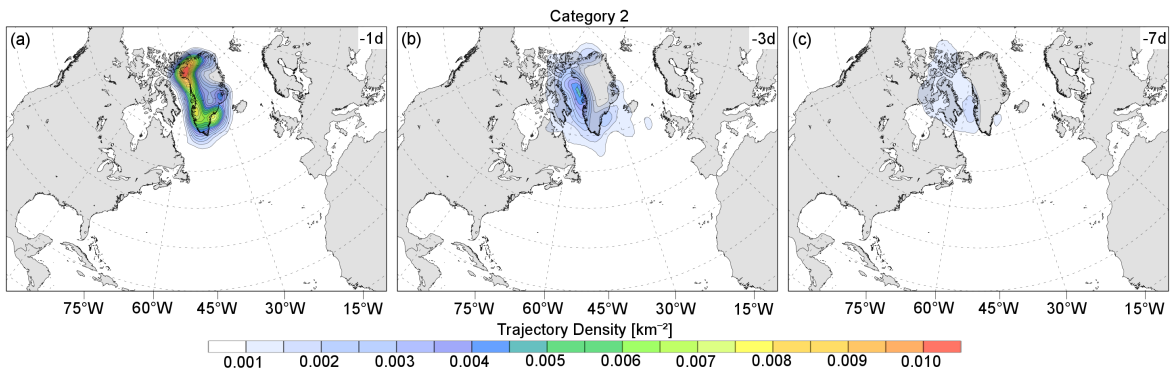
Figure 2: The trajectory density of category 2 trajectories, as described in Appendix Fig. 1.
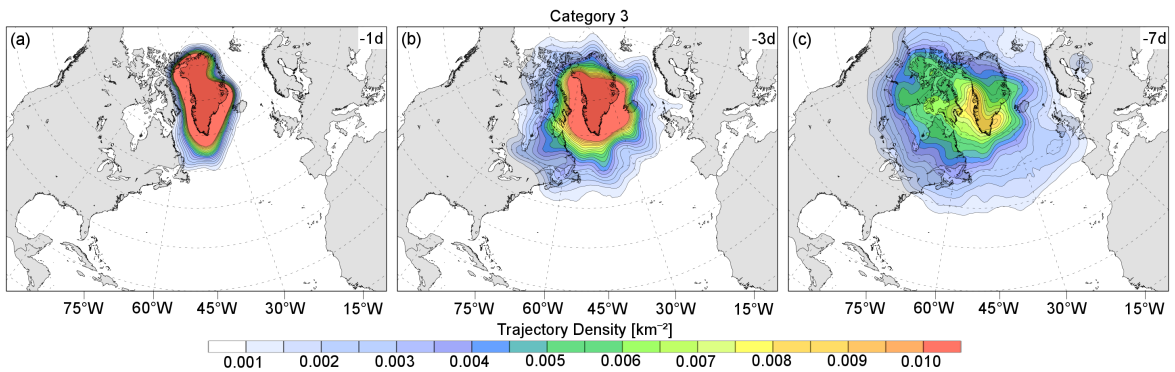
Figure 3: The trajectory density of category 3 trajectories, as described in Appendix Fig. 1.
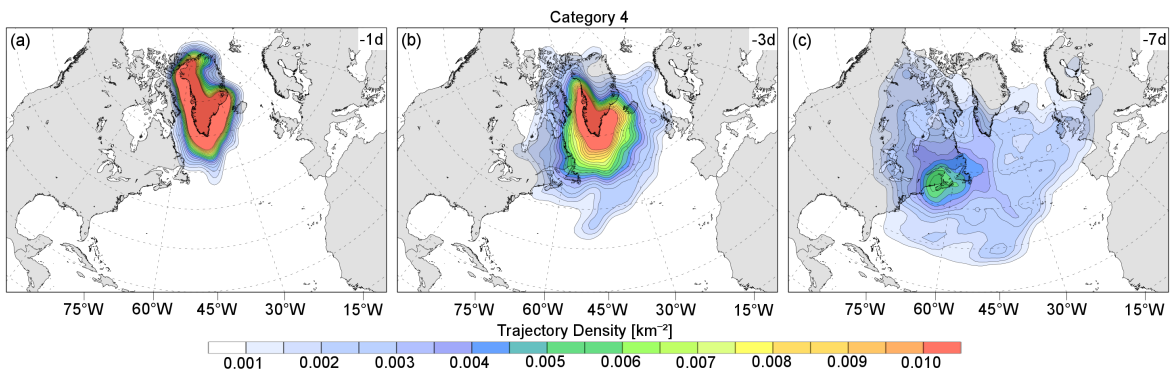
Figure 4: The trajectory density of category 4 trajectories, as described in Appendix Fig. 1.
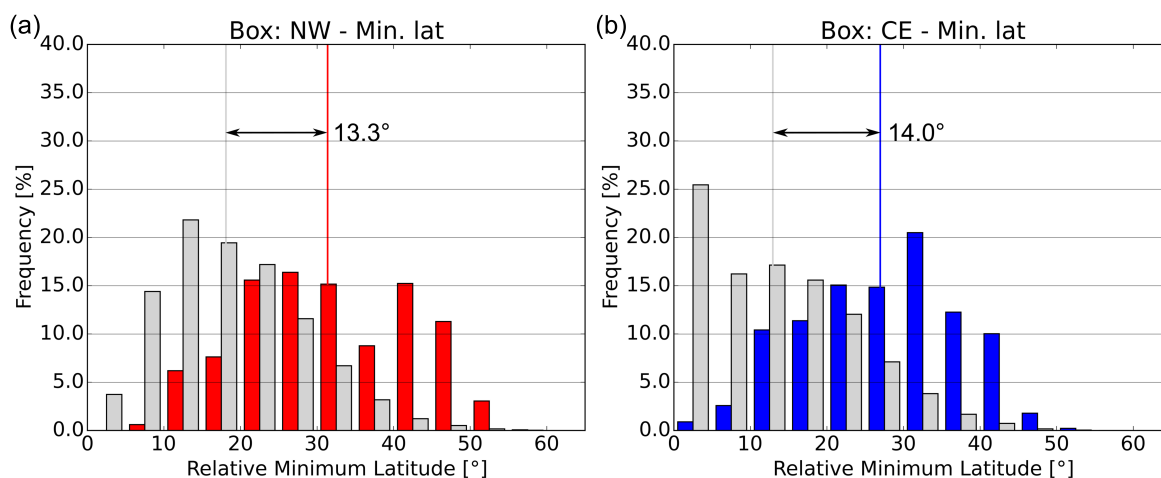
Figure 5: Normalized histograms of minimum latitude relative to latitude of arrival. The histograms are analogue to those in Fig. 3.26, but for regions (a) NW (red bars) and (b) CE (blue bars). For comparison, grey bars denote the occurrence frequencies of all JJA 1979–2017 trajectories reaching the respective region.
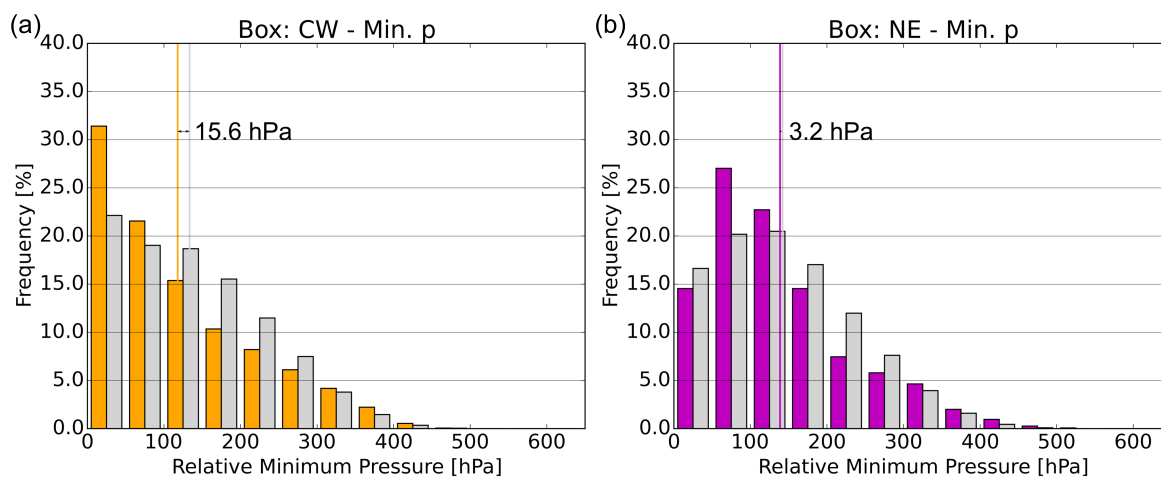
Figure 6: Normalized histograms of minimum pressure relative to pressure of arrival for regions (a) CW (orange bars) and (b) NE (purple bars), analogue to Appendix Fig. 5.

Appendix

ETH

Eidgenössische Technische Hochschule Zürich
Swiss Federal Institute of Technology Zurich

Declaration of originality

The signed declaration of originality is a component of every semester paper, Bachelor's thesis, Master's thesis and any other degree paper undertaken during the course of studies, including the respective electronic versions.

Lecturers may also require a declaration of originality for other written papers compiled for their courses.

_____

I hereby confirm that I am the sole author of the written work here enclosed and that I have compiled it in my own words. Parts excepted are corrections of form and content by the supervisor.

Title of work (in block letters):

```
```

Authored by (in block letters):
For papers written by groups the names of all authors are required.

Name(s):   **First name(s):**

....

....

....

....

With my signature I confirm that
− I have committed none of the forms of plagiarism described in the 'Citation etiquette' information sheet.
− I have documented all methods, data and processes truthfully.
− I have not manipulated any data.
− I have mentioned all persons who were significant facilitators of the work.

I am aware that the work may be screened electronically for plagiarism.

Place, date   **Signature(s)**

....

                                                ....

                                                ....

                                                ....

                                                ....

                                                For papers written by groups the names of all authors are required. Their signatures collectively guarantee the entire content of the written paper.